

國立臺灣大學理學院物理學系

博士論文

Department of Physics

College of Science

National Taiwan University

Doctoral Dissertation

以宇宙微波背景 B 模偏振探索迴圈量子宇宙學中的  
「前世宇宙」

Probing “Parent Universe” in Loop Quantum Cosmology  
with B-mode Polarization in Cosmic Microwave Background

張文軒

Wen-Hsuan Lucky Chang

指導教授：吳俊輝博士

Advisor: Jiun-Huei Protty Wu, Ph.D.

中華民國 108 年 7 月

July, 2019

國立臺灣大學  
物理學系

博士論文

以宇宙微波背景**□**模偏振探索迴圈量子宇宙學  
中的「前世宇宙」

張文軒  
撰

國立臺灣大學博士學位論文  
口試委員會審定書

以宇宙微波背景 B 模偏振探索迴圈量子宇宙學中的  
「前世宇宙」

Probing ‘Parent Universe’ in Loop Quantum Cosmology  
with B-mode Polarization in Cosmic Microwave Background

本論文係張文軒君（F00222018）在國立臺灣大學物理學系、所完成之博士學位論文，於民國 108 年 7 月 13 日承下列考試委員審查通過及口試及格，特此證明

口試委員：

吳俊輝

(簽名)

(指導教授)

董家雲

胡德邦

劉國凱

林建宏





# 致謝

能夠完成博士學位，首先我必須感謝吳俊輝老師的指導，這些年吳老師不僅在學術研究上不厭其煩地提點我，也不吝在言行間傳遞生活及處世的態度。特別感謝吳老師提供自由開放且獨立自主的研究環境，讓我張羅每個月的團隊健行活動，同時支持我時常踏上旅途尋找靈感，這些經驗都讓我收穫良多。

我要感謝這些年來一起探索宇宙的葉佳隆，我們不但是一起念書和做研究的戰友，也是生活和旅行的好夥伴。我們一起去夏威夷駐站觀測，一起到神戶參加研討會，神戶港後來甚至還成了佳隆向妻子以瑄求婚的地點，這些都是非常美好而特別的回憶。

感謝團隊成員林祐群、白尚平、林昀承、王富正、黃智威、詹明易（原名詹舜翔）、張業祥、何沛鑫、鄭邵安、傅思源、姚慧敏和姚于文這幾年來的相處與幫助，特別是感謝祐群協助修改我在這篇論文中所使用的一個CAMB子程式，並且提供他碩士論文中對宇宙重力波背景的模擬結果，讓我得以進行後續的計算。

感謝邱大維老師、黃冠維和何軍凱於研究早期的討論與協助。

感謝白色小車乘客蔡侑庭、吳昱萱、龔玟寧和詹竣翔在我博士生涯的最後階段，不斷接收我的負面心情，也讓我也能透過你們的眼，觀看這個世界的豐富與多彩。

感謝研究生涯中最重要的兄弟詹勳奇和楊智偉，我們一起準備資格考，一起分享彼此的專業，一起喝深夜咖啡，一起爬山，一起出遊。

感謝登山社暨太空社好友石恩、林子路、程永華和李芝瑩；感謝經常幫我釐清思緒、解憂釋疑的小秘書莊洧婷；感謝所有曾經來到我生命中的山友、球友、酒友和牌友們；感謝所有即便未能於此提及、卻都是我生命中不可或缺的貴人。

感謝各自陪我走過一段不朽歲月的黃筱涵和林昱廷。

感謝願意陪伴我經營未來漫漫人生的伴侶許珮筠。

最後，也是最重要的感謝，是父親張貴和母親張燕芬把我教育得如此堅強，並且全力支持我的一切理想與行動，縱然這些年總有前途茫茫的感覺，但在一切塵埃落定的今天，能夠留下來的都是永恆的愛。





## 中文摘要

我們希望透過觀測宇宙微波背景輻射的 B 模偏振，來探索迴圈量子宇宙學中所預測的「前世宇宙」，特別是驗證由前世宇宙中雙星系統所產生、並且經歷大反彈時期而存活下來的重力波，至今仍可被觀測的可能性。這個研究奠基於使用 ADM 形式描述的動力學，其中考慮了由量子理論所簡化的第零階繞異性修正。本論文提出了一個新的研究架構：利用轉移函數來演化前世宇宙的重力波，藉此得知它們在現今宇宙應有的樣貌。這是個透明且直覺的過程，讓人們能夠精準地討論在不同的迴圈量子宇宙學參數之下，這些來自前世宇宙的重力波將會為宇宙微波背景輻射 B 模偏振帶來什麼影響。我們期待能夠在不久的未來，科學家能夠透過觀測 B 模偏振的頻譜，藉此驗證這些來自前世宇宙的線索。值得一提的是，擁有時間對稱大反彈的宇宙所存在的可能性，已經被卜朗克計劃及 BICEP2 實驗的最新結果所排除。

**關鍵字：**迴圈量子宇宙學、暴縮、量子反彈、暴脹、重力波、轉移函數、宇宙微波背景輻射、B 模偏振、黑洞、類正態模





# Abstract

We aim to use the observations of B-mode polarization in the cosmic microwave background (CMB) to probe the “parent universe” under the context of loop quantum cosmology (LQC). In particular, we investigate the possibility for the gravitational waves (GWs) such as those from the stellar binary systems in the parent universe to survive the big bounce and thus to be still observable today. Our study is based on the background dynamics with the zeroth-order holonomy correction using the Arnowitt-Deser-Misner (ADM) formalism. We propose a new framework in which transfer functions are invoked to bring the GWs in the parent universe through the big bounce, inflation, and big bang to reach today. This transparent and intuitive formalism allows us to accurately discuss the influence of the GWs from the parent universe on the B-mode polarization in the CMB today under backgrounds of different LQC parameters. These features can soon be tested by the forthcoming CMB observations and we note that the LQC backgrounds with symmetric bouncing scenarios are ruled out by the latest observational results from Planck and BICEP2/Keck experiments.

Most parts of this dissertation are included in papers already published [1], submitted [2, 3], or in preparation [4].

**Keywords:** LQC, deflation, quantum bounce, inflation, GW, transfer function, CMB, B-mode polarization, black hole, QNM





# List of Publications

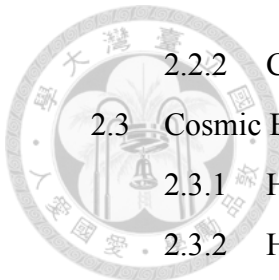
- [1] Wen-Hsuan Lucky Chang and Jiun-Huei Proty Wu. Time asymmetry of cosmic background evolution in loop quantum cosmology. *Physical Review D*, 99(12):123528, 2019.
- [2] Wen-Hsuan Lucky Chang and Jiun-Huei Proty Wu. New approach to evolving gravitational waves in loop quantum cosmology. (summmitted to *Physical Review D*). arXiv:1806.10508.
- [3] Wen-Hsuan Lucky Chang and Jiun-Huei Proty Wu. Signatures of the gravitational waves from parent universe in the CMB B-mode angular power spectrum. (summmitted to *Physical Review Letters*).
- [4] Wen-Hsuan Lucky Chang and Jiun-Huei Proty Wu. A solution to the UV divergence of scalar perturbation in loop quantum cosmology. (in preparation).





# Contents

<b>致謝</b>	i
<b>中文摘要</b>	iii
<b>Abstract</b>	v
<b>List of Publications</b>	vii
<b>Contents</b>	ix
<b>List of Figures</b>	xiii
<b>List of Tables</b>	xvii
<b>Units and Physical Constants</b>	xix
<b>Frequently Used Symbols</b>	xxi
<b>Abbreviations</b>	xxiii
<b>1 Introduction</b>	1
1.1 Historical Background . . . . .	1
1.2 Motivation and Objective . . . . .	4
1.3 Structure of Dissertation . . . . .	5
<b>2 Loop Quantum Cosmology</b>	7
2.1 Overview . . . . .	7
2.2 The Standard Cosmology . . . . .	8
2.2.1 $\Lambda$ CDM model . . . . .	8



2.2.2	Cosmological inflation . . . . .	10
2.3	Cosmic Background Dynamics . . . . .	13
2.3.1	Hamiltonian formalism . . . . .	13
2.3.2	Holonomy corrections . . . . .	14
2.3.3	The quantum bounce . . . . .	16
2.3.4	Realistic models of scalar field . . . . .	18
2.3.5	Cosmological deflation . . . . .	21
2.4	Summary . . . . .	26
<b>3</b>	<b>Evolution of Gravitational Waves</b>	<b>27</b>
3.1	Overview . . . . .	27
3.2	Gravitational Waves in LQC . . . . .	28
3.2.1	Gravitaional-wave equation . . . . .	28
3.2.2	Transfer functions . . . . .	30
3.2.3	Numerical approach to transfer functions . . . . .	34
3.3	Inflationary and Deflationary Epochs . . . . .	35
3.3.1	The slow-roll inflation . . . . .	35
3.3.2	Transfer functions for inflation . . . . .	35
3.3.3	Transfer functions for deflation . . . . .	38
3.3.4	Transfer functions and their symmetry in de Sitter space . . . . .	39
3.4	Quantum Bounce Epoch . . . . .	42
3.4.1	Definition of quantum bounce epoch . . . . .	42
3.4.2	Field-free approximation for effective mass . . . . .	43
3.4.3	Analytical solutions with field-free approximation . . . . .	44
3.5	Critical Breakthroughs . . . . .	48
3.5.1	Consistency with Bogoliubov transformation . . . . .	48
3.5.2	Solving the IR suppression problem . . . . .	51
3.5.3	Improvement from field-free approximation . . . . .	53
3.6	Models with a Parent Universe . . . . .	54
3.6.1	Bouncing scenarios . . . . .	54
3.6.2	Signals from the parent universe . . . . .	56
3.7	Summary . . . . .	58



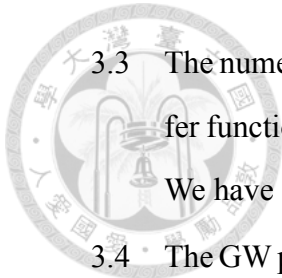
<b>4 Signatures of Pre-existing Gravitational Waves</b>	<b>61</b>
4.1 Overview . . . . .	61
4.2 Pre-existing Gravitational Waves . . . . .	62
4.2.1 Gravitational-wave background as initial conditions . . . . .	62
4.2.2 Astronomical sources of gravitational waves . . . . .	65
4.3 Observational Features . . . . .	67
4.3.1 Power spectrum of gravitational waves . . . . .	67
4.3.2 CMB B-mode angular power spectrum . . . . .	71
4.3.3 Restriction of chaotic background parameters . . . . .	73
4.3.4 Restriction of $R^2$ background parameters . . . . .	77
4.4 Observational Constraints . . . . .	79
4.4.1 CMB TT, EE, and TE angular power spectra . . . . .	79
4.4.2 CMB B-mode angular power spectrum . . . . .	85
4.5 Summary . . . . .	86
<b>5 The UV Divergence on Scalar Perturbations</b>	<b>87</b>
5.1 Overview . . . . .	87
5.2 Scalar Perturbations in LQC . . . . .	88
5.2.1 Evolutionary equation . . . . .	88
5.2.2 The UV divergence problem . . . . .	91
5.3 The Parent Black Hole . . . . .	93
5.3.1 Spacetime geometry . . . . .	93
5.3.2 Inflaton production . . . . .	97
5.3.3 Black hole perturbations . . . . .	99
5.4 Summary . . . . .	101
<b>6 Conclusion</b>	<b>103</b>
6.1 Innovation and Achievement . . . . .	103
6.2 Outlook in the Future . . . . .	104
<b>A The Fourier Transform</b>	<b>107</b>
<b>Bibliography</b>	<b>109</b>



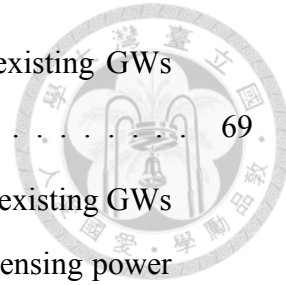


# List of Figures

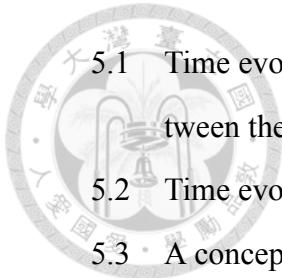
2.1	Time evolutions of the scale factor (top panel), the Hubble parameter (middle panel), and the comoving Hubble radius (bottom panel). We consider $V(\phi) = 0$ in this figure for simply demonstrating the quantum bounce.	17
2.2	The scale factor (upper panel) and the scalar field (lower panel) as functions of time at different values of $\phi_B$ , for the chaotic potential. . . . .	19
2.3	The same as Figure 2.2 for the $R^2$ potential. . . . .	20
2.4	Time evolution of the normalized chaotic potential before the quantum bounce. . . . .	22
2.5	The number of $e$ -foldings $N_e^D$ for chaotic deflation as functions of $\phi_B$ for different inflaton mass $m_\phi$ . . . . .	23
2.6	Time evolutions of the comoving Hubble radius (upper panel) and the scalar field (lower panel) with $\phi_B = 2.75$ ( $< \phi_{\text{crit}}$ ; brown dashed), 2.95 ( $\approx \phi_{\text{crit}}$ ; orange solid), and 2.98 ( $> \phi_{\text{crit}}$ ; red dashed) for chaotic potential. The vertical lines denote the beginning (right) and the end (left) of deflation, as the time goes leftwards in the plot. . . . .	24
2.7	The number of $e$ -foldings $N_e^D$ for $R^2$ deflation as functions of $\phi_B$ for different inflaton mass $m_H$ . . . . .	25
3.1	The effective mass as a function of the conformal time, evolving from the quantum bounce ( $\eta = 0$ ) to the beginning of inflation ( $\eta = \eta_b$ ). . . . .	30
3.2	The numerical (blue dashed) and analytical (red solid) results for the transfer functions of GWs in de Sitter inflation with chaotic potential. The consistency between the two is obvious. . . . .	37



3.3	The numerical (blue dashed) and analytical (red solid) results for the transfer functions of GWs in the quantum bounce epoch with chaotic potential. We have applied the field-free approximation for $m_{\text{eff}}$ . . . . .	46
3.4	The GW power spectra generated by the quantum fluctuations in the Minkowski vacuum before the quantum bounce epoch. The results based on the Bogoliubov transformation (dashed) and on our approach of transfer functions (solid) are totally consistent. . . . .	50
3.5	The primordial GW power spectra in the standard inflationary cosmology (solid) as compared with the result based on sub-horizon approximation (dashed). . . . .	51
3.6	The GW power spectrum normalized to its primordial power spectrum in a realistic cosmological model. The brown dashed curve is normalized to $P_T^{\text{std}}(k) \propto k^{-3}$ (sub-horizon approximation) while the red solid curve is normalized to the correct $P_T^{\text{dS}}(k)$ . . . . .	52
3.7	The predicted GW power spectra based on the “old” (dash-dotted) and “new” (solid) approaches as compared with the numerical result (dashed), all normalized to the same primordial $P_T^{\text{dS}}(k)$ . . . . .	53
3.8	The HABS (purple), IABS (blue), and NSBS (blank) regions in the parameter space $(\phi_B, m_\phi)$ . The two dashed lines are drawn for $N_e = 60$ and 70, respectively. . . . .	55
3.9	The scale-invariant power spectrum of pre-existing GWs generated by a constant $\tilde{u}_k^{(\text{i})}$ in the parent universe. . . . .	57
4.1	The energy density spectra of GWs (upper panel) [5] and the initial $\tilde{u}_k$ (lower panel) generated by stellar binary systems with respect to the physical frequency. The solid curves and the shaded bands present the most likely values and the uncertainties, respectively. The scale factor today $a_0$ has been chosen to be unity. . . . .	66
4.2	The power spectrum as evolved from the pre-existing GWs (solid) with the uncertainties from modelling the pre-existing GWs (shaded). . . . .	68



4.3	Comparisons of the power spectra resulted from the pre-existing GWs with different background parameters. . . . .	69
4.4	The B-mode angular power spectrum resulted from the pre-existing GWs (solid), as compared with the primordial (dashed) and the lensing power (dash-dotted). . . . .	71
4.5	Comparisons of the B-mode angular power spectra resulted from the pre-existing GWs with different background parameters. . . . .	72
4.6	The maximum of $C_l^{\text{BB}}/C_l^{\text{BB, std}}$ within $20 < l < 330$ with respect to $\alpha_\phi$ in the chaotic background with $W = 10^{13}$ . . . . .	75
4.7	The maximum of $C_l^{\text{BB}}/C_l^{\text{BB, std}}$ within $20 < l < 330$ with respect to $m_\phi$ in the chaotic background with $W = 10^{13}$ . . . . .	75
4.8	The regions of observational acceptance (shaded) in the $(\alpha_\phi, m_\phi)$ -space with selected $W$ 's. . . . .	76
4.9	The maximum value of $C_l^{\text{BB}}/C_l^{\text{BB, std}}$ within $20 < l < 330$ with respect to $\alpha_\phi$ in the $R^2$ background with $W = 10^{12}$ . . . . .	78
4.10	The maximum value of $C_l^{\text{BB}}/C_l^{\text{BB, std}}$ within $20 < l < 330$ with respect to $m_\phi$ in the $R^2$ background with $W = 10^{12}$ . . . . .	78
4.11	The regions of observational acceptance (shaded) in the $(\alpha_\phi, m_H)$ -space with selected $W$ 's. . . . .	79
4.12	The CMB TT, EE, TE, and BB angular power spectra in the chaotic background with $\alpha_\phi = 1.0$ and $W = 10^{13}$ as compared to the current concordance model (dashed). . . . .	81
4.13	The CMB TT, EE, TE, and BB angular power spectra in the chaotic background with $m_\phi = 10^{-7}$ and $W = 10^{13}$ . . . . .	82
4.14	The CMB TT, EE, TE, and BB angular power spectra in the $R^2$ background with $\alpha_\phi = 1.0$ and $W = 10^{12}$ . . . . .	83
4.15	The CMB TT, EE, TE, and BB angular power spectra in the $R^2$ background with $m_H = 10^{-4}$ and $W = 10^{12}$ . . . . .	84



5.1	Time evolution of the deformation factor and effective damping ratio between the quantum bounce and the beginning of inflation. . . . .	89
5.2	Time evolution of $\tilde{\mathcal{R}}_{ck}$ with different $k$ across the quantum bounce. . . . .	90
5.3	A conceptual time division of the quantum bounce epoch for approximating the scalar perturbations. . . . .	91
5.4	A conceptual Penrose-Carter diagram of the scenario that our present universe was born inside a Schwarzschild black hole. . . . .	96



# List of Tables

2.1	The number of $e$ -foldings for inflation with chaotic potential. . . . .	21
2.2	The number of $e$ -foldings for deflation with chaotic potential. . . . .	21
2.3	The value of $\phi_{\text{crit}}$ for different $m_\phi$ in chaotic deflation. They correspond to the minima in Figure 2.5. . . . .	23
2.4	The value of $\phi_{\text{crit}}$ for different $m_H$ in $R^2$ deflation. They correspond to the minima in Figure 2.7. . . . .	25





# Units and Physical Constants

The values of the related universal constants of fundamental physics in this dissertation in the international system of units (SI) are

Speed of light:  $c \approx 2.9979 \times 10^8$  m/s,

Gravitational constant:  $G \approx 6.6741 \times 10^{-11}$  N · m<sup>2</sup>/kg<sup>2</sup>,

Reduced Planck constant:  $\hbar \approx 1.0546 \times 10^{-34}$  J · s.

They are all normalized to be unity when expressed in terms of the Planckian units by definition:  $c = G = \hbar \equiv 1$ . The Planckian units that appear in this dissertation are

Planck length:  $l_{\text{Pl}} \approx 1.6162 \times 10^{-35}$  m,

Planck time:  $t_{\text{Pl}} \approx 5.3911 \times 10^{-44}$  s,

Planck mass:  $m_{\text{Pl}} \approx 2.1765 \times 10^{-8}$  kg.

We especially note that the two useful astrophysical units are therefore

$1 \text{ Mpc} \approx 3.2615 \times 10^6$  lyr  $\approx 1.9092 \times 10^{50}$ ,

$1 M_{\odot} \approx 9.1390 \times 10^{37}$ ,

where Mpc denotes  $10^6$  pc and  $M_{\odot}$  denotes the solar mass.





# Frequently Used Symbols

Symbol	Definition	Page
$\phi, \pi_\phi$	Scalar field and its conjugate momentum	10,14
$c, p$	Connection variables in the ADM formalism	13
$c_h^{(n)}$	The $n$ th-order holonomized connection variable	14
$H_{\text{grav}, \bar{\mu}}^{(n)}$	The $n$ th-order holonomized Hamiltonian of spacetime	15
$H_{\bar{\mu}}^{(n)}$	The $n$ th-order holonomized total Hamiltonian	15
$\rho_c^{(n)}$	The $n$ th-order holonomized critical energy density	15
$\rho_j, p_j$	Energy density and pressure of content “j”	9
$\Omega_j$	Energy parameter of content “j”	9
$N_e, N_e^D$	Number of $e$ -foldings for inflation and deflation	11,22
$\phi_B$	Scalar field at the quantum bounce	18
$\phi_{\text{crit}}$	Scalar field at the quantum bounce that minimizes deflation	23
$\alpha_\phi$	Scalar field at the quantum bounce normalized to $\phi_{\text{crit}}$	67
$m_\phi, m_H$	Masses of chaotic and $R^2$ inflaton	19,20
$W$	Rescaling factor of GW background	66
$\tilde{u}_k$	Fourier mode of comoving GW function	29
$m_{\text{eff}}$	Effective mass of $\tilde{u}$	29
$T_k$	Transfer functions of $\tilde{u}$ as a $2 \times 2$ matrix	31
$\tilde{\mathcal{R}}_{ck}$	Mode function of comoving intrinsic curvature perturbation	88
$\Omega, \zeta_{\text{eff}}$	Deformation factor and effective damping ratio of $\tilde{\mathcal{R}}_{ck}$	88,89
$Z_{\omega, s, \ell}$	Quasi normal mode of black hole perturbation	99





# Abbreviations

Abbreviation	Full Form
ADM	Arnowitt-Deser-Misner
GR	General theory of relativity
QFT	Quantum field theory
SM	Standard model of particle physics
FRW	Friedmann-Roberson-Walker
CMB	Cosmic microwave background
BBN	Big bang nucleosynthesis
CDM	Cold dark matter
HSRA / PSRA	Hubble / potential slow-roll approximation
LQG / LQC	Loop quantum gravity / cosmology
PKR	Potential to kinetic energy ratio
HABS / IABS	Highly / intermediately asymmetric bouncing scenario
NSBS	Nearly symmetric bouncing scenario
GW	Gravitational wave
QNM	Quasi normal mode (black hole perturbation)
LIGO	Laser Interferometer Gravitational-wave Observatory





# Chapter 1

## Introduction

*“I believe in Spinoza’s God, Who reveals Himself in the lawful harmony of the world.”*

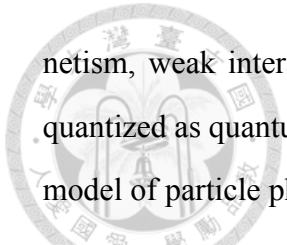
— Albert Einstein

### 1.1 Historical Background

“Once upon a time, ...” A story always begins like this. However, how long can we trace back to tell the whole story about our universe? From east to west and culture to culture, human beings attempt to comprehend our universe for thousands of years. The word “cosmology” first appeared in 1656 in Thomas Blount’s *Glossographia* [6], which is a study of the story about our universe.

Cosmology used to be parts of philosophy, mythology, and religion, and had just turned to modern science after Einstein proposed his theory of gravity in 1916. The universe was lonely until Einstein was born, my advisor Jiun-Huei Protty Wu said. That is true. Starting from the past century, people can accurately measure signals from the outer space, make correct predictions, and explain lots of phenomena according to Einstein’s theory.

We are now talking cosmology as a discipline studying the evolution, dynamics, and ingredients of the universe. It is definitely an application of all fundamental physics. In our current understanding, there are four fundamental interactions in nature: electromag-



netism, weak interaction, strong interaction, and gravity. The former three have been quantized as quantum field theories (QFTs), which are combined together as the standard model of particle physics (SM) [7–9].

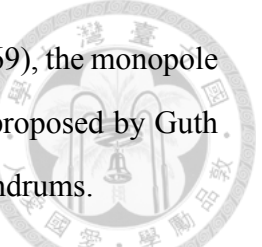
The SM is a non-abelian gauge theory with the symmetric group  $SU(3)_C \times SU(2)_L \times U(1)_Y$ . In this theory, there are elementary particles including twelve gauge bosons (photon, three weak bosons, and eight gluons), twelve fermions (six quarks and neutrinos each), and the Higgs particle. The Higgs particle provides masses to the other SM elementary particles through the so-called “Higgs mechanism”, the fermions construct all the known matters (such as baryons, atoms, and molecules) in the universe, and the gauge bosons propagate the interactions between all of them.

However, gravity has not yet been quantized in a satisfactory manner up to now. It is still a classical field theory, the general theory of relativity (GR) [10–12], built up by Einstein in 1916. In the GR, gravity is treated as geometry of spacetime. Energy and momentum change the geometry, and the geometry determines the evolution of energy and momentum as well.

Although gravity has not yet been quantized as expected, it still works perfectly for describing our universe most of the time. The mainstream models of cosmology are based on the GR with the cosmological principle saying that the universe is homogeneous and isotropic on large scale. Moreover, the SM particles are considered to survive in this so-called Friedmann-Roberson-Walker (FRW) spacetime. Because our universe is expanding at present, it is supposed to evolve from a status with extremely tiny size and high temperature (i.e. the hot big bang theory). The hot big bang theory reaches several successes on predicting the cosmic microwave background (CMB) first discovered in 1965 by Penzias and Wilson [13] and explaining the big-bang nucleosynthesis (BBN) well [14]. Nowadays, the standard model of hot big bang cosmology has been proposed with the cosmological constant ( $\Lambda$ ) and the cold dark matter (CDM), which is known as the  $\Lambda$ CDM model [15–17].

Unfortunately, there are still conundrums associated with the  $\Lambda$ CDM model. These “cosmological conundrums” are the horizon problem (pointed out by Charles Misner in

the late 1960s), the flatness problem (first noticed by Robert Dicke in 1969), the monopole problem [18, 19], and so on. A new idea, the inflationary cosmology, proposed by Guth in 1981 [20] is now commonly adopted to solve the cosmological conundrums.



Inflation is simply defined as an epoch of accelerated expansion of the universe. The size of the universe grows up rapidly during inflation, and hence most of the contents are causally separated with each other. The curvature of spacetime becomes extremely flat, and the density of magnetic monopoles is smeared out after inflation. This cosmological inflation is triggered by a scalar field before the hot big bang age. It not only settles the cosmological conundrums, but also gives initial conditions to the hot big bang universe. The scalar field is considered as a quantum field with the corresponding particle named “inflaton”. The inflatons can be pair-produced from the vacuum and pair-annihilated with each other, and thus generate “primordial perturbations” during the inflationary epoch. The primordial perturbations are decomposed to three types: scalar, vector, and tensor. They are believed to be the origin of gravitational structures which have been accurately measured by the observations in the past.

The context of combining the  $\Lambda$ CDM model and the inflationary cosmology is currently recognized as the standard model of cosmology (standard cosmology) [21, 22].

However, there must exist a singularity in the finite past if our universe is described by the standard cosmology [23]. The so-called “singularity problem” is supposed to be solved by those theories that combine the rules of QFTs with the GR. Loop quantum gravity (LQG) is one of the attempts to do so although it is still an incomplete theory. With applying the cosmological principle, LQG can be simplified as a symmetry-reduced theory called loop quantum cosmology (LQC) [24].

LQC is a theory employing the FRW model with quantum corrections. In this dissertation, we particularly use a semiclassical approach. The extra terms involve a scalar field to resolve the singularity with a quantum bounce [25] and in turn allow for the existence of a “parent universe” [26–28]. The cosmological inflation can be driven naturally after the bounce [29]. Moreover, there must be freedoms on time symmetry of cosmic background, which depends on the potential and kinetic energies of the scalar field at the bounce.

## 1.2 Motivation and Objective

It is a great motivation for us to study the testability of the fundamental physics, especially through cosmological aspects. Recently people considered the tensor perturbations, which are known as the linearized gravitational waves (GWs), generated during the quantum bounce in LQC [30], and further obtained their imprints on the angular power spectrum of the CMB B-mode polarization [31]. Besides, we are more interested in and will thus pay our attention on the GWs propagating from the parent universe.

To reach our primary target, it acquires a more detailed research on cosmic background dynamics including the time asymmetry of the quantum bounce. We thus define a new parameter to quantitatively calculate the numbers of  $e$ -foldings of inflation and the possible “deflation”. The reason is that, in the case of time-symmetric bouncing scenarios, inflation and deflation may counteract each other, likely leaving the cosmological conundrums unresolved.

Due to the complexity of the Bogoliubov transformations used in the literature [30], we propose a new framework which employs the “transfer functions” to bring arbitrary GWs from any given initial time to a designated final time. This method is mathematically so simple and intuitive that enables us to not only use the transfer functions to study our present universe, but also probe the parent universe by figuring out the GW signals emitted far before the quantum bounce.

We naively suppose that the parent universe appeared similarly to our present universe and thus contained astronomically bounded systems that generated “pre-existing GWs”. As the first attempt, we only consider the stellar binary systems in this work. This is now fascinating owing that the Laser Interferometer Gravitational-Wave Observatory (LIGO) had discovered the GWs generated by an event of binary black hole merger in early 2016 [32] and confirmed several GW events later on [33–36]. Furthermore, the first electromagnetic counterpart of GWs has already been observed by the Fermi Gamma-ray Burst Monitor in 2017 [37].

To find out the imprints of the pre-existing GWs on the CMB signals, first of all, we calculate the power spectra of the pre-existing GWs at the end of inflation. Then

we employ CAMB, a cosmological code developed by Antony Lewis [38], to obtain the corresponding CMB angular power spectra and compare them to that predicted by the current concordance model of the standard cosmology. Finally we use the observational results of the CMB angular power spectra from the Planck [39, 40] and the BICEP2/Keck [41, 42] experiments to confine the LQC parameters.

### 1.3 Structure of Dissertation

In Chapter 2, we review the current standard cosmology and introduce the cosmic background dynamics of LQC. We study the time symmetry of the quantum bounce, propose and quantitatively analyze deflation before the quantum bounce. In Chapter 3, we calculate the transfer functions for each evolutionary epoch to evolve the pre-existing GWs from the parent universe through the quantum bounce to our present universe. Chapter 4 presents the results of the CMB angular power spectra and the constraints on the model parameters. In addition to the major target, we discuss the pre-existing scalar perturbation and its divergent behavior on small scale in Chapter 5. We further discuss the possibility that our universe was born inside a parent black hole. We concludes this dissertation in Chapter 6.

We note that the units of all physical quantities appearing in this dissertation are normalized with the Planckian units except for specially stated or labeled. For details about the Planckian units, please refer to Page xix. We list the frequently used symbols on Page xxi and the abbreviations in Page xxiii. Last of all please consult Appendix A for the Fourier transform used in this dissertation.





# Chapter 2

## Loop Quantum Cosmology

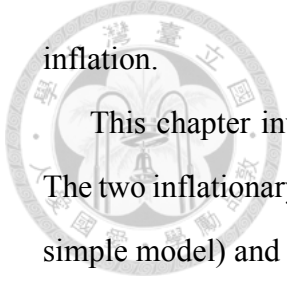
*“No great discovery was ever made without a bold guess.”*

— Isaac Newton

### 2.1 Overview

In LQC, the quantum corrected Friedmann equation and fluid equation [43, 44] evolve the scale factor and the Hubble parameter. These two equations were derived with the Hamiltonian formulation in a semiclassical approach [45] involving the connection variables (known as the Ashtekar variables) with two major types of quantum corrections: the holonomy [46–48] and the inverse volume [49]. The equations of motions of the connection variables can be obtained by calculating their Poisson brackets with the Hamiltonian, and are equivalent to the quantum corrected Friedmann equation and fluid equation.

Within the LQC framework, inflation occurs naturally after the quantum bounce due to the existence of a scalar field [29] so that the cosmological conundrums can be resolved in the conventional way. Before the quantum bounce this scalar field may also generate a period of damped contraction called deflation. The amount of deflation and that of inflation may differ and one key is the “potential to kinetic energy ratio” (PKR) of the scalar field at the quantum bounce. Here we shall directly employ a more intuitive quantity  $\phi_B$ , the  $\phi$  value at the quantum bounce, to study the asymmetry between deflation and



inflation.

This chapter investigate in detail the dependence of cosmic time asymmetry on  $\phi_B$ . The two inflationary models considered here are the chaotic potential (a commonly chosen simple model) and the  $R^2$  potential (a realistic model to data [50]).

We provide a brief review on the standard model of cosmology including the  $\Lambda$ CDM model and the cosmological inflation in Section 2.2. Then in Section 2.3 we lay out the convention of LQC, where Subsection 2.3.1 defines the Hamiltonian formalism, with its quantum corrections presented in Subsection 2.3.2. Subsections 2.3.3 and 2.3.4 investigate the time asymmetry in cosmic evolution, in particular employing the  $\phi_B$ . Subsection 2.3.4 further discusses the possible deflation and its impact. We conclude this chapter in Section 2.4.

## 2.2 The Standard Cosmology

### 2.2.1 $\Lambda$ CDM model

The standard cosmology is built with the GR and the cosmology principle. It is known as the hot big bang theory which describes the SM particles in the FRW spacetime by two nontrivial Einstein equations. The first one is the Friedmann equation

$$H^2 + \frac{K}{a^2} = \frac{8\pi}{3}\rho_{\text{tot}} + \frac{\Lambda}{3} \quad (2.1)$$

and the second one is the Raychaudhuri equation

$$\frac{\ddot{a}}{a} = -\frac{4\pi}{3}(\rho_{\text{tot}} + 3p_{\text{tot}}) + \frac{\Lambda}{3}, \quad (2.2)$$

where  $\rho_{\text{tot}}$  and  $p_{\text{tot}}$  stand for the total energy density and pressure of all cosmic contents. The scale factor and the Hubble parameter are symbolized by  $a$  and  $H$ , respectively. The overdot indicates the derivative of the cosmic (proper) time  $t$ .

The curvature constant  $K$  in Equation (2.1) measures the spatial topology and geometry of the universe while the universe is possible to be closed (when  $K > 0$ , known as

three-sphere  $S^3$ ), flat (when  $K = 0$ , known as Euclidean three-space  $R^3$ ), and open (when  $K < 0$ , known as three-hyperboloid  $H^3$ ). By convention,  $K$  is usually normalized to be  $\pm 1$  and 0. The cosmological constant  $\Lambda$  is firstly proposed by Einstein as a universally repulsive force to construct a static universe. It is now considered to be nonzero as a dark energy candidate to explain the result of Type Ia supernova observation in 1998 [51].

According to the conservation of energy and momentum, the cosmic contents with energy density  $\rho_j$  and pressure  $p_j = p_j(\rho_j)$  behave like perfect fluids which can be described by the fluid equation

$$\dot{\rho}_j + 3\frac{\dot{a}}{a}(\rho_j + p_j) = 0. \quad (2.3)$$

The subscript “j” can be “m” for matter and “r” for radiation. There are only two kinds of particles in the  $\Lambda$ CDM model: radiation ( $p_r = \rho_r/3$ ) and matter ( $p_m \ll \rho_m$ , including cold dark matters). According to the Friedmann equation, it is straight forward to define the energy parameters by

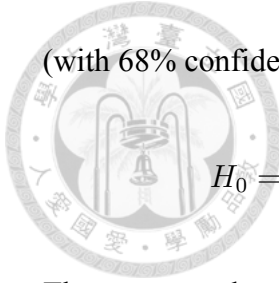
$$\Omega_j \equiv \frac{8\pi}{3H^2}\rho_j, \quad (2.4)$$

which are functions of scale factor. We study flat models in this dissertation because we have known that our universe is almost flat. Moreover, we consider the cosmological constant  $\Lambda$  as a physical content in such a flat universe. We calculate the total energy density parameter at a certain time by

$$\Omega_{\text{tot}} = \left(\frac{a}{a_0}\right)^3 \Omega_{m0} + \left(\frac{a}{a_0}\right)^4 \Omega_{r0} + \Omega_{\Lambda0} \quad (2.5)$$

with all known present values  $\Omega_{m0}$ ,  $\Omega_{r0}$ , and  $\Omega_{\Lambda0}$ . We note that the subscript “0” stands for “today” by convention.

The  $\Lambda$ CDM model reaches several successes. It is able to explain the observational phenomena such as the Hubble expansion, the CMB, and the BBN. With the observational results provided by the Planck experiment in 2018 [52], the  $\Lambda$ CDM parameters are well-fit



(with 68% confidence limits) as following. The Hubble parameter today  $H_0$  is

$$H_0 = 67.36 \pm 0.46 \text{ km/s/Mpc} = (1.1761 \pm 0.0094) \times 10^{-61}. \quad (2.6)$$

The present value of the energy density parameters are

$$\Omega_{\Lambda 0} = 0.6874 \pm 0.0073 \quad \text{and} \quad \Omega_{m0} = 0.3153 \pm 0.0073. \quad (2.7)$$

The red-shift of matter-radiation equality is

$$z_{\text{eq}} = 3402 \pm 26. \quad (2.8)$$

Nevertheless, there are still some challenges (the cosmological conundrums and the singularity problem [23]) that cannot be solved by the  $\Lambda$ CDM model and have been studied in the past few decades.

### 2.2.2 Cosmological inflation

It is believed that some of the cosmological conundrums (i.e. the flatness problem, the horizon problem, and the monopole problem) can be resolved by introducing a cosmological inflation before the hot big bang era. Inflation is defined as an epoch of the universe with accelerating expansion

$$\dot{a} > 0 \quad \text{and} \quad \ddot{a} > 0. \quad (2.9)$$

A time-dependent scalar field  $\phi$  is proposed to generate inflation so that one can model inflation by the Lagrangian formalism with a potential  $V(\phi)$  as

$$\rho_\phi = \frac{1}{2}\dot{\phi}^2 + V(\phi) \quad \text{and} \quad p_\phi = \frac{1}{2}\dot{\phi}^2 - V(\phi). \quad (2.10)$$

There are hundreds of inflationary models proposed during the past 30 years. The most intuitive consideration is called “de Sitter expansion”, which is simply originated from the

cosmological constant in GR. According to the fluid equation, the equation of  $\phi$ -motion can be obtained as

$$\ddot{\phi} + 3H\dot{\phi} = -\frac{d}{d\phi}V(\phi). \quad (2.11)$$

The amount of expansion during inflation is quantitatively defined by the number of  $e$ -foldings

$$N_e \equiv \ln \left[ \frac{a_e}{a_b} \right], \quad (2.12)$$

where  $a_b \equiv a(t_b)$  and  $a_e \equiv a(t_e)$  are the scale factors at the beginning ( $t = t_b$ ) and the end ( $t = t_e$ ) of inflation, respectively. The number of  $e$ -foldings  $N_e$  is required to be at least about 50 according to the current observations for solving the cosmological conundrums which are mentioned before.

To simplify the analytical calculations, one can employ the potential slow-roll approximation (PSRA) [53–55] and the Hubble slow-roll approximation (HSRA) [56].

QFTs quantize the inflationary field as a particle called inflaton. Indeed, physicists aim to find an unified theory that contains a scalar field playing the role of inflaton such as the SM Higgs and the supersymmetric particles. The inflatons are pair-produced from the vacuum and pair-annihilated with their antiparticles during inflation, and thus generate primordial perturbations. They form gravitational structures later when they are frozen out and then re-enter the causal horizon. According to the GR, one can decompose the primordial perturbations into three types: scalar, vector, and tensor modes, in the Fourier domain, which can be observed by measuring the intensity and the polarizations of the CMB photons. The primordial scalar perturbations have already been observed. The data released by Planck in 2018 [52] gave the best-fit amplitude of the power spectrum of the primordial scalar perturbations as

$$A_S \equiv A_S(k^{(*)}) = 2.100 \times 10^{-9}, \quad (2.13)$$

where the superscript “( $*$ )” denotes the reference (pivot) scale,  $k = k^{(*)} = 0.05 \text{ Mpc}^{-1}$ , of the horizon entry. However, the primordial GWs of which amplitude of power spectrum is labeled as  $A_T$  have not yet been detected. The BICEP2/Keck experiments set the latest upper bound of the tensor-to-scalar ratio in 2016 [42]:

$$r \equiv \frac{A_S}{A_T} < 0.07. \quad (2.14)$$

People introduced the spectral indices ( $n$  for scalar and  $n_T$  for tensor) to conveniently parametrize the power spectra  $P_S$  and  $P_T$  of the primordial perturbations as power laws. The de Sitter expansion predicts

$$n^{\text{dS}} = 1 \quad \text{and} \quad n_T^{\text{dS}} = 0, \quad (2.15)$$

while different models give different values which can thus be directly examined by observing the tilt of the power spectra. Planck 2018 data [52] prefers the spectral index of primordial scalar perturbations being

$$n = 0.9649 \pm 0.0042. \quad (2.16)$$

This rules out numbers of inflationary models including the de Sitter expansion. Furthermore, there are tens of models which have been tested by the literature [50, 57–59].

However, the initial conditions of inflation are still undetermined and the singularity in the  $\Lambda\text{CDM}$  model is still unresolved. It means that we need further beyond the standard cosmology, say quantum cosmology, which employs QFTs to the pre-inflationary epoch and thus well handles the physics of the early universe.

## 2.3 Cosmic Background Dynamics



### 2.3.1 Hamiltonian formalism

To have a good handle on the quantum mechanical properties of the early universe, we employ the Arnowitt-Deser-Misner (ADM) approach. The Hamiltonian of spacetime is

$$H_{\text{grav}} = -\frac{3}{8\pi\gamma^2}c^2\sqrt{p}, \quad (2.17)$$

where  $p$  and  $c$  are the connection variables, which are related to the cosmological variables  $a$  and  $H$  as [43, 60]

$$|p| = \frac{1}{4}L^2a^2 = \frac{1}{4}a^2 \quad \text{and} \quad c = \frac{1}{2}L(K + \gamma aH) = \frac{1}{2}\gamma aH, \quad (2.18)$$

and satisfy the canonical relation [43]

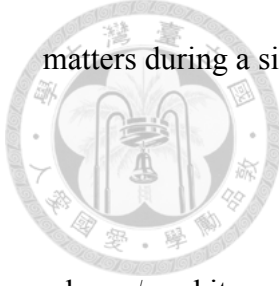
$$[c, p]_{\text{PB}} = \frac{8\pi\gamma}{3}. \quad (2.19)$$

The subscript “PB” denotes that the calculation rule follows Possion bracket rather than the commutation. The Barbero-Immirzi parameter [61, 62]  $\gamma = \log(3)/\sqrt{2\pi}$  can be obtained from the computation of black hole entropy [63]. In Equation (2.18), we have dropped the normalized curvature parameter of the FRW model  $K$  because we consider a flat universe in this dissertation and chosen the coordinate length of the finite-sized cubic cell  $L$  in LQG to be unity. It is obvious that the energy density of spacetime

$$\rho_{\text{grav}} = p^{-3/2}H_{\text{grav}} \quad (2.20)$$

is unbounded while the size of the universe goes to zero ( $a \rightarrow 0$ ).

On the other hand, the Hamiltonian of the scalar field  $\phi$ , which is the only content that



matters during a single-field inflation, is

$$H_\phi = \frac{\pi_\phi^2}{2p^{3/2}} + p^{3/2}V(\phi), \quad (2.21)$$

where  $\phi$  and its conjugate momentum  $\pi_\phi$  satisfy the canonical relation [47]:

$$[\phi, \pi_\phi]_{\text{PB}} = 1. \quad (2.22)$$

The GR then requires that the total Hamiltonian must stay constant (simply chosen to be zero) at all times:

$$H_{\text{tot}} = H_{\text{grav}} + H_\phi = 0. \quad (2.23)$$

This is the Hamiltonian constraint, which is commonly used in solving the Einstein equations numerically. Consequently, the equations of motion that describe the dynamics of the universe are

$$\frac{dq}{dt} = [q, H_{\text{tot}}]_{\text{PB}}, \quad (2.24)$$

where  $q$  represents  $p, c, \phi$ , and  $\pi_\phi$  [31]. This set of equations is equivalent to the Friedmann equation and the fluid equation.

### 2.3.2 Holonomy corrections

For the quantum corrections in the above formalism, we adopt a semiclassical approach in LQC [45]. In this dissertation, we consider the models satisfying the cosmological principle [24] and we employ only the holonomy corrections [46–48]. The  $n$ th-order holonomized connection variable  $c_h^{(n)}$  is defined as [47]

$$c_h^{(n)} \equiv \frac{1}{\bar{\mu}} \sum_{k=0}^n \frac{(2k)!}{2^{2k}(k!)^2(2k+1)} (\sin \bar{\mu}c)^{2k+1}, \quad (2.25)$$

where  $\bar{\mu} = \sqrt{\Delta/p}$  is the discreteness variable with  $\Delta = 2\sqrt{3}\pi\gamma$  the standard choice of the area gap in the full theory of LQG [26]. One key feature in LQC is that the connection variable in the standard cosmology has to be replaced by holonomies. Thus the Hamiltonian of spacetime with holonomy correction up to the  $n$ th order is [64]

$$H_{\text{grav},\bar{\mu}}^{(n)} = -\frac{3}{8\pi\gamma^2}(c_h^{(n)})^2\sqrt{p}. \quad (2.26)$$

Finally the new Hamiltonian constraint is [30, 64]

$$H_{\bar{\mu}}^{(n)} = H_{\text{grav},\bar{\mu}}^{(n)} + H_\phi = 0. \quad (2.27)$$

We can hold the second equal sign as what was done in GR [65], consequently, we can use a lapse function  $N$  to change the time variable from the proper time  $t$  to a new parametric time  $t'$  via  $dt' = N^{-1}dt$ . The corresponding Hamiltonian with the new time variable is  $H_{\bar{\mu}}^{(n)'} = NH_{\bar{\mu}}^{(n)}$ . The new time variable  $t'$  in the case of  $N = \sqrt{p}$  indicates to the conformal time  $\eta$  defined by  $d\eta = a^{-1}dt$ .

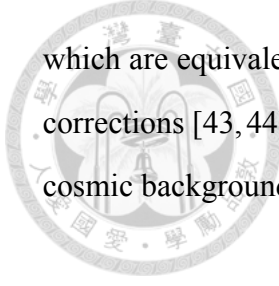
With such quantum corrections, it is obvious that the energy density of the spacetime  $\rho_{\text{grav}}$  is always finite. The extreme values appear when  $\bar{\mu}c$  equals to 0,  $\pi/2$ , or its multiples. When  $\bar{\mu}c = \pi/2$ , the Hamiltonian  $H_{\text{grav},\bar{\mu}}^{(n)}$  reaches its minimum and thus  $H_\phi$  reaches its maximum. The maximal energy density of the inflaton  $\rho_\phi = p^{-3/2}H_\phi$  is called the “critical energy density” and is related to the holonomies as [47]

$$\rho_c^{(n)} = \frac{\sqrt{3}}{16\pi^2\gamma^3} \left[ \sum_{k=0}^n \frac{(2k)!}{2^{2k}(k!)^2(2k+1)} \right]^2, \quad (2.28)$$

which is confined between  $\rho_c^{(0)} \simeq 0.82$  and  $\rho_c^{(\infty)} \simeq 2.02$ . We note that the standard cosmology is recovered ( $c_h^{(n)} \rightarrow c$ ) when  $\bar{\mu}c \rightarrow 0$  (that is, when  $p \gg 1$ ). This indicates that the quantum effects are important only when the universe is tiny ( $p \sim \Delta$ ).

Consequently the equations of motion can be obtained as

$$\frac{dq}{dt} = [q, H_{\bar{\mu}}^{(n)}]_{\text{PB}}, \quad (2.29)$$



which are equivalent to the Friedmann equation and the fluid equation with the quantum corrections [43, 44]. According to the literature [47, 48], the higher-ordered effects on the cosmic background are distinguishable but secondary.

### 2.3.3 The quantum bounce

As we have seen in the previous section,  $\rho_\phi$  now has a maximum  $\rho_c^{(n)}$  when  $\bar{\mu}c = \pi/2$  and thus avoids the singularity. To see how this is manifested in the behavior of cosmic expansion, we can use the equations of motion to first obtain the Hubble parameter as

$$H = \frac{\dot{a}}{a} = \frac{2}{p}[p, H_{\bar{\mu}}^{(n)}]_{\text{PB}} = \frac{4}{\gamma\sqrt{p}} \cos(\bar{\mu}c) \mathcal{O}_n(\bar{\mu}c) c_h^{(n)}, \quad (2.30)$$

where

$$\mathcal{O}_n(\bar{\mu}c) \equiv \sum_{k=0}^n \frac{(2k)!}{2^{2k}(k!)^2} (\sin \bar{\mu}c)^{2k}. \quad (2.31)$$

The solid curves in Figure 2.1 are the numerical solutions of the scale factor  $a$ , the Hubble parameter  $H$ , and the comoving Hubble radius  $|H^{-1}/a|$ , as functions of time  $t$ . The scale factor  $a(t)$  is normalized to unity at  $t = 0$ . It shows that the universe contracts before the quantum bounce and expands after the bounce, with a turning point of  $a(0) = 1$  corresponding to  $\bar{\mu}c = \pi/2$ . We refer to the epoch before the bounce as the parent universe.

For the Hubble parameter, it changes its sign at the bounce. The fact that  $H(0) = 0$  indicates that the comoving Hubble radius  $|H^{-1}/a|$  diverges to infinity at  $t = 0$ . It means that the quantum effects are extremely strong such that the whole universe is in causal contact at the quantum bounce.

The dashed curves in Figure 2.1 are the results in the standard cosmology, without the quantum corrections. In this case the universe starts from singularity at  $t = 0$ , without causal connections at all because the comoving Hubble radius is zero at this time.

While the solid curves show symmetry in time with respect to the quantum bounce at  $t = 0$ , such symmetry may be broken in general cases. According to Equations (2.21),

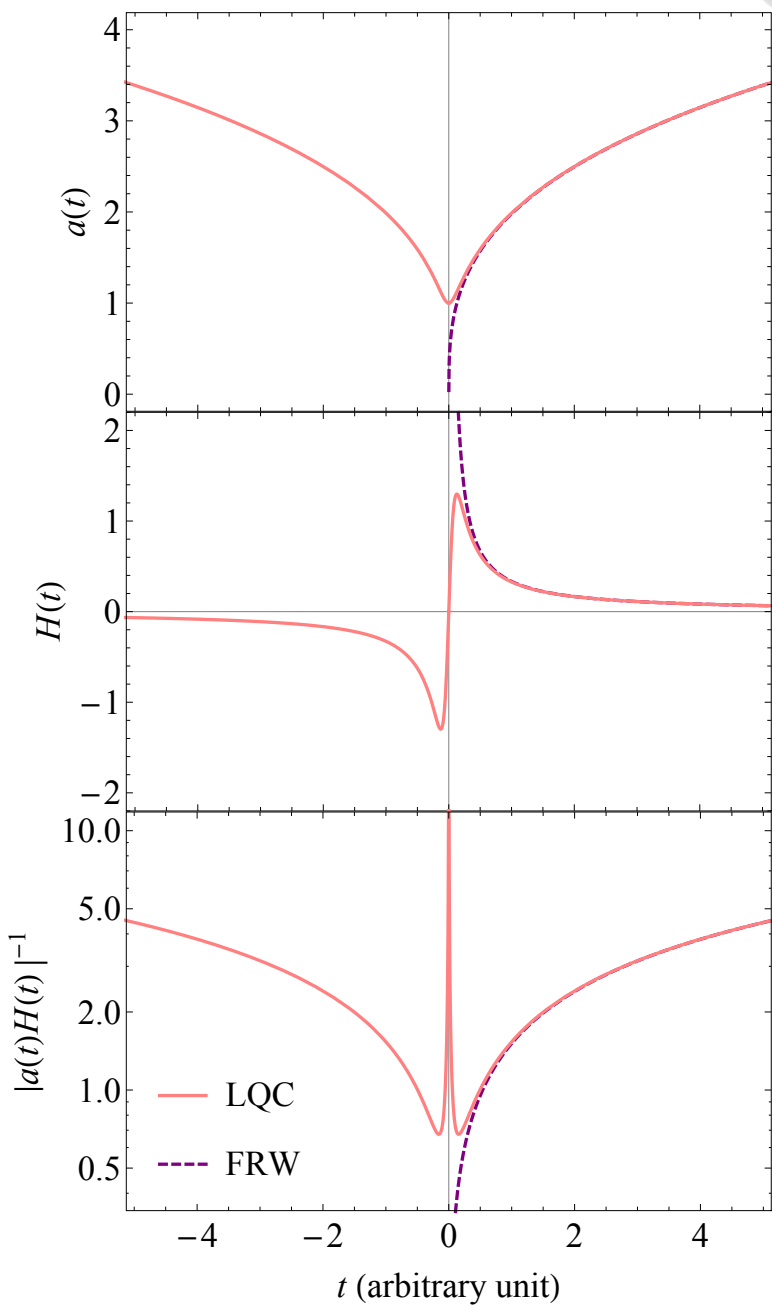
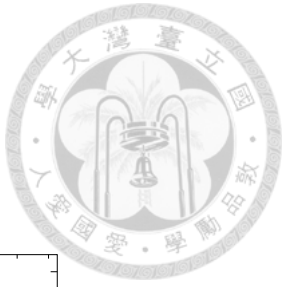
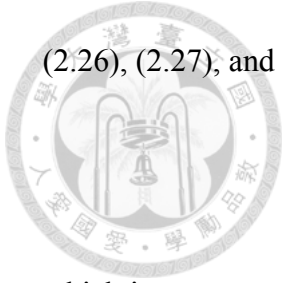


Figure 2.1: Time evolutions of the scale factor (top panel), the Hubble parameter (middle panel), and the comoving Hubble radius (bottom panel). We consider  $V(\phi) = 0$  in this figure for simply demonstrating the quantum bounce.



(2.26), (2.27), and (2.29), with  $\phi_B$  the  $\phi$  value at  $t = 0$ , we have

$$\frac{1}{2}\dot{\phi}_B^2 + V(\phi_B) = \rho_c^{(n)}, \quad (2.32)$$

which is a constant for given  $n$ . Thus the PKR of the scalar field at the bounce is a free parameter so we may define a “bouncing phase” as

$$\theta_B = \tan^{-1} \frac{\sqrt{2V(\phi_B)}}{\dot{\phi}_B}, \quad (2.33)$$

where  $\dot{\phi}_B$  is the  $\dot{\phi}$  value at  $t = 0$ . For the cases where  $V(\phi)$  is an even or odd functions in  $\phi$ ,  $\theta_B$  determines the level of time asymmetry in the cosmic background dynamics. The case  $\theta_B = 0$  corresponds to a time symmetry with respect to  $t = 0$ ; other cases lead to time asymmetry. For the case where  $V(\phi)$  is not symmetric in  $\phi$ , the cosmic background dynamics is always asymmetric with respect to the quantum bounce.

Reference [30] studied a special kind of asymmetric cases called the “shark-fin type”, which provides a relatively large number of  $e$ -foldings in inflation after the quantum bounce.

### 2.3.4 Realistic models of scalar field

Equation (2.33), however, has a limit that  $V(\phi)$  must stay non-negative, and thus cannot be applied to a general potential. Also, the PKR does not have one-to-one correspondence to the time symmetry. Due to these reason, we consider directly the  $\phi$  value at the quantum bounce, labeled as  $\phi_B$  in Equation (2.32), as a free parameter that quantifies the symmetry. Because the number of  $e$ -foldings in inflation depends on the value of  $\phi$ , the value of  $\phi_B$  is more apparently related to the intrinsic properties of an inflationary model than  $\theta_B$ .

For scalar potential symmetric in  $\phi$ , the case  $\phi_B = 0$  corresponds to a time-symmetric case; in a time-asymmetric case, the  $\phi$  value at the end of deflation would differ from the beginning of inflation leading to a nonzero  $\phi_B$ .

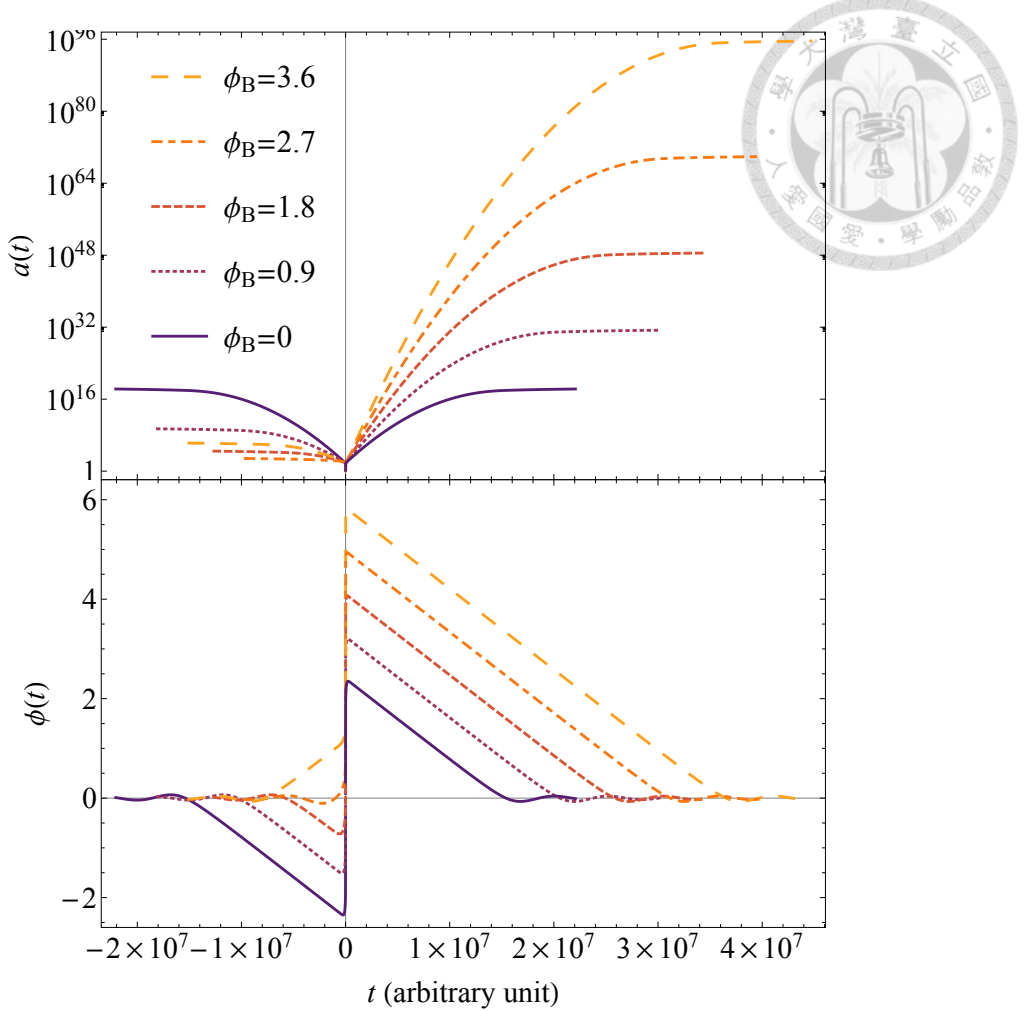


Figure 2.2: The scale factor (upper panel) and the scalar field (lower panel) as functions of time at different values of  $\phi_B$ , for the chaotic potential.

Given this new parameter  $\phi_B$ , we first consider the chaotic inflation

$$V(\phi) = \frac{1}{2}m_\phi^2\phi^2. \quad (2.34)$$

Figure 2.2 illustrates the scale factor and the scalar field as functions of time, at different values of  $\phi_B$ . We have considered the zeroth-ordered holonomy correction ( $n = 0$ ) and chosen the inflaton mass  $m_\phi = 10^{-6}$  in deriving the result in this figure. It is clear that  $\phi_B = 0$  corresponds to a time-symmetric case, while a larger  $\phi_B$  corresponds to a larger number of  $e$ -foldings. In addition, the amount of deflation is less when  $\phi_B$  is larger. The shark-fin type in Reference [30] corresponds to our case with  $\phi_B \approx 2.7$ , where the time asymmetry is about the largest.

Table 2.1 lists the number of  $e$ -foldings for chaotic inflation with various  $\phi_B$  and  $m_\phi$ .

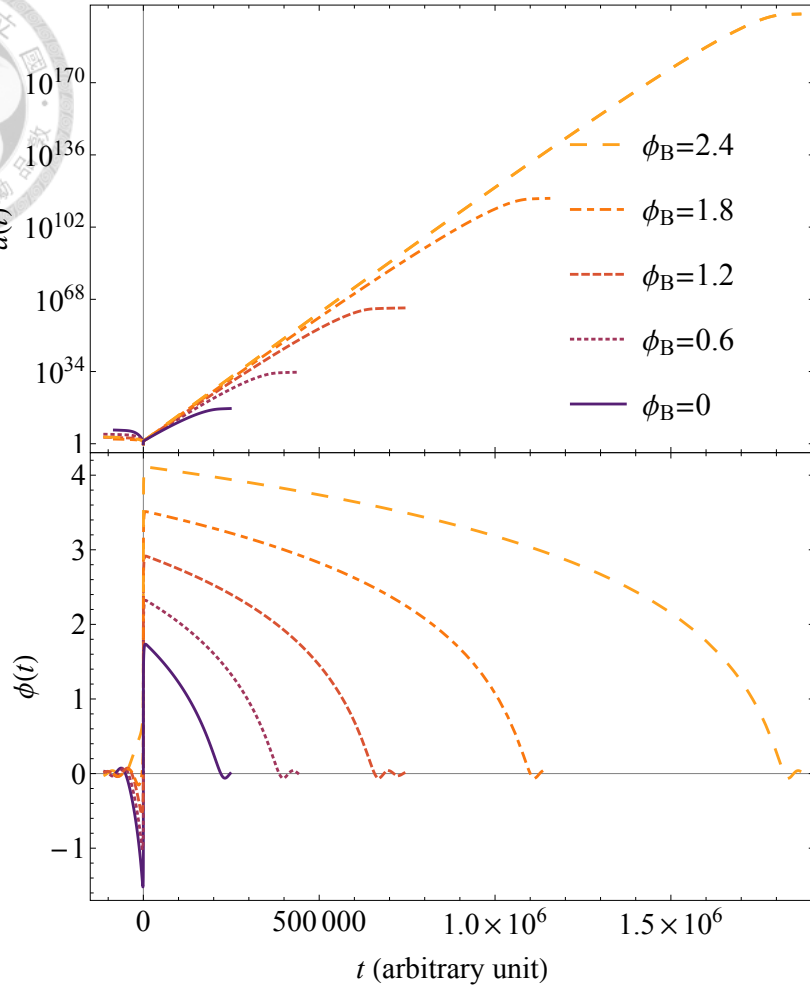


Figure 2.3: The same as Figure 2.2 for the  $R^2$  potential.

Next we consider the  $R^2$  inflation

$$V(\phi) = m_H^4 \left(1 - e^{-\sqrt{\frac{2}{3}}\phi}\right). \quad (2.35)$$

where  $m_H$  is the inflaton mass, which is normally denoted as  $\Lambda$  in literature. Here the subscript “H” stands for the Higgs-like particle. To clarify, this  $R^2$  potential is not a quantum field in Starobinsky gravity but a classical field in GR. The resulting time evolutions of the scale factor and the scalar field at different values of  $\phi_B$  are presented in Figure 2.3, where we have used  $n = 0$  and  $m_H = 10^{-2}$ . Unlike the chaotic inflation, here we see no case with time symmetry simply because  $R^2$  potential is not symmetric in  $\phi$ .

These results also indicate that the cosmological inflation occurs naturally after the quantum bounce, with its initial condition unambiguously and naturally determined rather

than manipulatively designed. This fact was previously studied for both by time-symmetric background [64] and time-asymmetric cosmic background [30].

To sum up, the four conditions required for solving the four coupled equations of motion are the Hamiltonian constraint  $H_{\bar{\mu}}^{(n)} = 0$ , the turning point condition  $\bar{\mu}c = \pi/2$ , the value of  $\phi_B$ , and the normalization of the scale factor  $a$ . The only free parameter in these four conditions is  $\phi_B$ . To uniquely solve the cosmic background, we might determine further free parameters coming with inflationary models such as  $m_\phi$  and  $m_H$ .

$\phi_B$ $m_\phi$	0	0.9	1.8	2.7	3.6
$10^{-4}$	18.5	33.0	52.2	76.0	105
$10^{-6}$	36.3	66.6	107	157	217
$10^{-8}$	60.6	113	183	270	374
$10^{-10}$	91.7	173	280	414	575

Table 2.1: The number of  $e$ -foldings for inflation with chaotic potential.

$\phi_B$ $m_\phi$	0	0.9	1.8	2.7	3.6
$10^{-4}$	18.5	8.45	2.56	0.33	3.66
$10^{-6}$	36.3	15.6	3.97	0.25	8.84
$10^{-8}$	60.6	25.1	5.64	0.19	16.5
$10^{-10}$	91.7	36.9	7.55	0.17	26.2

Table 2.2: The number of  $e$ -foldings for deflation with chaotic potential.

### 2.3.5 Cosmological deflation

When we look into the epoch right before the quantum bounce, the scalar field may induce a damped contraction of the space, which we call the cosmological deflation. During deflation, we have

$$\dot{a} < 0 \quad \text{and} \quad \ddot{a} > 0. \quad (2.36)$$

In contrast to inflation, the comoving Hubble radius grows with time during deflation. In other words, the size of causally contacted region is increasing. In addition, the energy

densities and thus the perturbations are increasing. All these may counteract the inflationary effects that we need for resolving the cosmological conundrums, so a scenario with comparably less deflation is in general needed. This in turn requires asymmetry in time with respect to the quantum bounce.

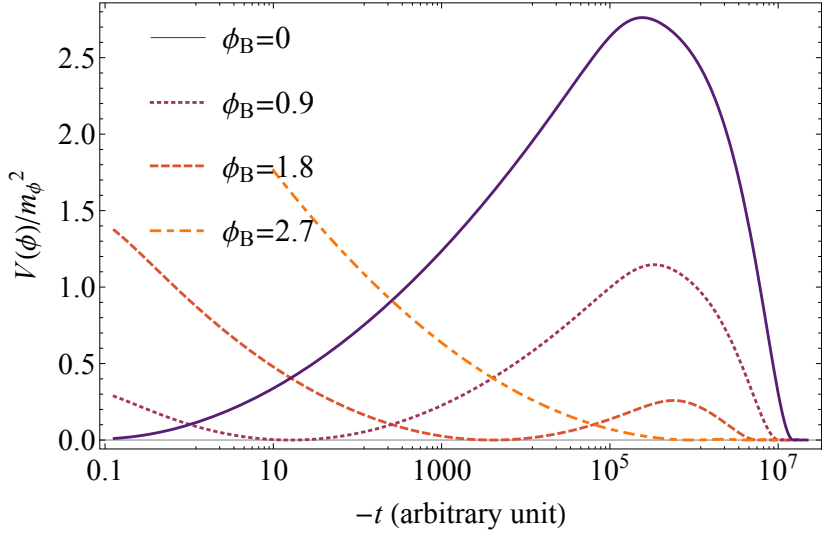


Figure 2.4: Time evolution of the normalized chaotic potential before the quantum bounce.

Most of the formalism used for study of inflation are equally useful for the study of deflation, for example, the slow-roll approximation. Figure 2.4 shows how the chaotic potential evolves with time before the quantum bounce. Deflation takes place when the slope is small and thus near the peaks of the curves in the figure. For deflation we define the number of  $e$ -foldings similar to that of the inflation as

$$N_e^D \equiv \ln \left( \frac{a_b^D}{a_e^D} \right), \quad (2.37)$$

where  $a_b^D \equiv a(t_b^D)$  and  $a_e^D \equiv a(t_e^D)$  are the scale factor at the beginning ( $t = t_b^D$ ) and the end of deflation ( $t = t_e^D$ ), respectively. For a chaotic potential under the slow-roll approximations, with  $\phi_e^D \equiv \phi(t_b^D)$  the  $\phi$  value at the end of deflation, this reduced to [66]

$$N_e^D \simeq 2\pi \left( \phi_e^D \right)^2 - \frac{1}{2} = 4\pi \frac{V(\phi_e^D)}{m_\phi^2} - \frac{1}{2}. \quad (2.38)$$

Combining this with Figure 2.4, we see the dependence of  $N_e^D$  on  $\phi_B$ . The dependence of

$N_e^D$  on  $m_\phi$  is implicit as  $a_b^D$  and  $a_e^D$  are dependent on  $m_\phi$ . Table 2.2 lists the dependence of  $N_e^D$  on some discrete values of  $m_\phi$  and  $\phi_B$ . We see that for a fixed value of  $m_\phi$  the case  $\phi_B = 2.7$  always gives the least amount of deflation, as we can also see in Figure 2.4 when combined with Equation (2.38). A comparison between Tables 2.1 and 2.2 also shows that the case  $\phi_B = 0$  has the same amount of inflation and deflation so their effects are expected to be reciprocally canceled out. This is the time-symmetric case. Such scenarios are less of our interest because the cosmological conundrums revive here. In the following we shall discuss the circumstances where such cancellation can be minimized.

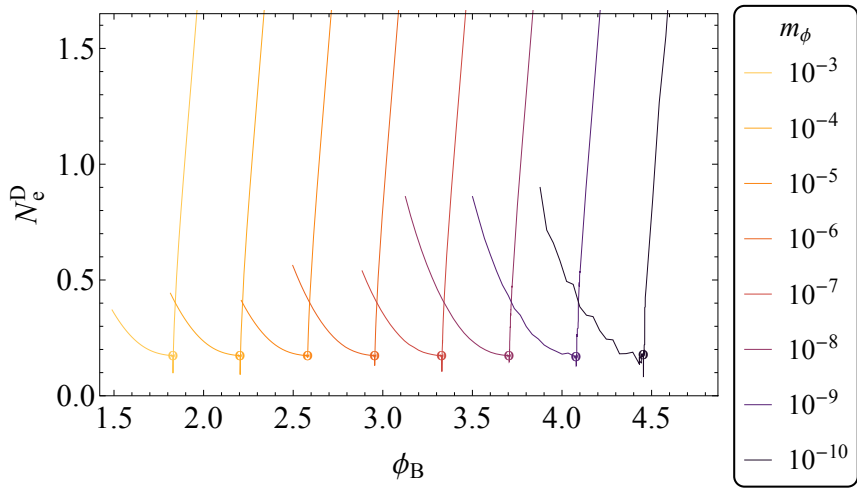


Figure 2.5: The number of  $e$ -foldings  $N_e^D$  for chaotic deflation as functions of  $\phi_B$  for different inflaton mass  $m_\phi$ .

$m_\phi$	$10^{-3}$	$10^{-4}$	$10^{-5}$	$10^{-6}$	$10^{-7}$	$10^{-8}$	$10^{-9}$	$10^{-10}$
$\phi_{\text{crit}}$	1.83	2.20	2.58	2.95	3.33	3.70	4.08	4.45

Table 2.3: The value of  $\phi_{\text{crit}}$  for different  $m_\phi$  in chaotic deflation. They correspond to the minima in Figure 2.5.

We first numerically determine how  $N_e^D$  depends on  $\phi_B$ . For the chaotic potential, Figure 2.5 shows the  $N_e^D$  as a function of  $\phi_B$  at different but fixed values of  $m_\phi$ . We use  $\phi_{\text{crit}}$  to denote the value of  $\phi_B$  at which the minimum  $N_e^D$  occurs in a curve. It is interesting to note that the minimum values of  $N_e^D$  in all cases are about the same, 0.17. We also find that  $\phi_{\text{crit}}$  increases with  $m_\phi$ .

Table 2.3 summarizes the  $\phi_{\text{crit}}$  for different  $m_\phi$ . Here we surprisingly find that  $\phi_{\text{crit}}$

has a linear relationship with the order of magnitude of  $m_\phi$  as

$$\phi_{\text{crit}} = 0.70 - 0.37 \log_{10}(m_\phi). \quad (2.39)$$

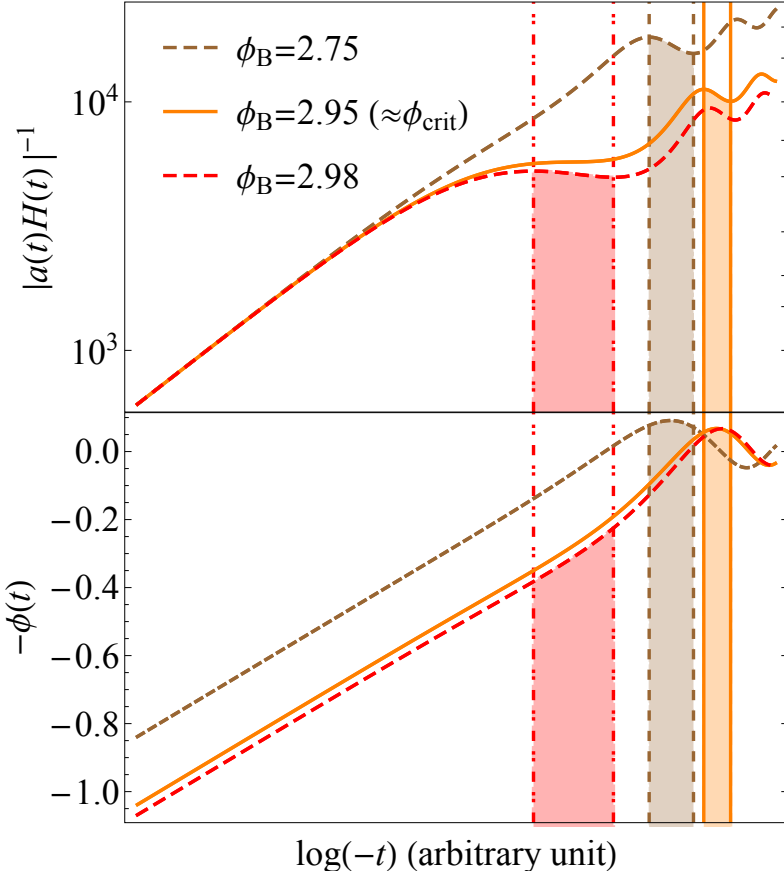


Figure 2.6: Time evolutions of the comoving Hubble radius (upper panel) and the scalar field (lower panel) with  $\phi_B = 2.75$  ( $< \phi_{\text{crit}}$ ; brown dashed),  $2.95$  ( $\approx \phi_{\text{crit}}$ ; orange solid), and  $2.98$  ( $> \phi_{\text{crit}}$ ; red dashed) for chaotic potential. The vertical lines denote the beginning (right) and the end (left) of deflation, as the time goes leftwards in the plot.

On the other hand, for each curve in Figure 2.5, we note that the value of  $N_e^D$  increases more dramatically when  $\phi_B$  departs from  $\phi_{\text{crit}}$  to a larger value than to a smaller value. This can be explained in Figure 2.6 where we plot the comoving Hubble radius (upper panel) and the scalar field (lower panel) both as functions of time, for the case  $m_\phi = 10^{-6}$ . We consider three cases:  $\phi_B < \phi_{\text{crit}}$  (brown dashed),  $\phi_B \approx \phi_{\text{crit}}$  (orange solid), and  $\phi_B > \phi_{\text{crit}}$  (red dashed). In the upper panel, the parts of curves with negative slopes (increasing Hubble radius) indicate the periods when deflation takes place. These periods are shaded down to the lower panel and we see that the change in  $\phi$  during deflation is obviously larger in the

case when  $\phi_B > \phi_{\text{crit}}$ , resulting in the larger amount of deflation as seen in Figure 2.5. We also note that in the lower panel of Figure 2.6 the parts in the curves that cross  $\phi = 0$  can be thought of as the “inverse reheating”, at which inflatons are produced by other particles. This is a period when all existing particles are converted to inflatons. This epoch always take place before deflation, so the scenario is like a mirror process of inflation.

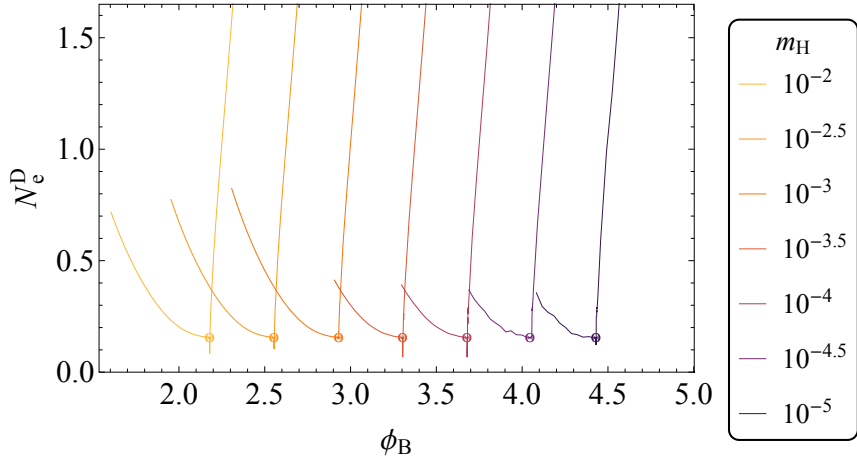


Figure 2.7: The number of  $e$ -foldings  $N_e^D$  for  $R^2$  deflation as functions of  $\phi_B$  for different inflaton mass  $m_H$ .

$m_H$	$10^{-2}$	$10^{-2.5}$	$10^{-3}$	$10^{-3.5}$	$10^{-4}$	$10^{-4.5}$	$10^{-5}$
$\phi_{\text{crit}}$	2.18	2.55	2.93	3.30	3.68	4.05	4.43

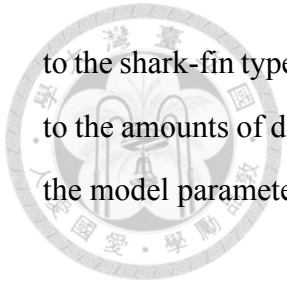
Table 2.4: The value of  $\phi_{\text{crit}}$  for different  $m_H$  in  $R^2$  deflation. They correspond to the minima in Figure 2.7.

For the  $R^2$  potential, the counter results are shown in Figure 2.7 and Tables 2.4. There is a linear relationship between  $\phi_{\text{crit}}$  and the order of magnitude of  $m_H$  as well:

$$\phi_{\text{crit}} = 0.68 - 0.75 \log_{10}(m_H) \quad (2.40)$$

Again the minimum values of  $N_e^D$  in all cases are about the same, 0.15, and for a fixed  $m_H$  the amount of deflation  $N_e^D$  increases more quickly when  $\phi_B$  depart from  $\phi_{\text{crit}}$  to a larger value than to a smaller value. We verified that the reason of this is the same as discussed in Figure 2.6.

In summary, for the selected inflationary models in this dissertation, the amount of deflation is minimized when  $\phi_B$  reaches  $\phi_{\text{crit}}$ . For the chaotic potential this corresponds



to the shark-fin type (see Figure 2.2). Since this  $\phi_B$  is model dependent and closely related to the amounts of deflation and inflation, we may use observations to confine  $\phi_B$  and thus the model parameters.

## 2.4 Summary

In this chapter, we reviewed the standard cosmology including the  $\Lambda$ CDM model and the cosmological inflation. According to the cosmological principle, our universe is assumed to be spatially homogeneous and isotropic on large scale and therefore described by the Friedmann and Raychaudhuri equations. However, there is a singularity in the finite past. We therefore considered the quantum bounce to replace the initial singularity under the context of LQC.

To solve the cosmological conundrums, in this chapter, we studied two inflationary models, the chaotic potential and the  $R^2$  potential. We employed the parameter  $\phi_B$  to discuss the asymmetry in the cosmic background evolution with respect to the quantum bounce. It is particularly noted that the time-symmetric scenarios should be avoided because in such cases inflation and the deflationary counterpart may counteract each other, likely leaving the cosmological conundrums unresolved.

In the consideration of number of  $e$ -foldings, there is a critical value of  $\phi_B$  at which the amount of deflation is minimized. This critical value  $\phi_{\text{crit}}$  depends on the model parameters, namely the inflaton masses  $m_\phi$  and  $m_H$  in the chaotic potential and the  $R^2$  potential, respectively, in our demonstration. Thus when we study any model in LQC, we should be cautious about the level of time asymmetry in order to have sufficient inflation that is not preanceled out by deflation before the quantum bounce.

Within this context, other issues such as the cosmological perturbations also require proper treatment. In this regard we proposed a new approach to evolving the GWs in the next chapter.



# Chapter 3

## Evolution of Gravitational Waves

*“The soul that sees beauty may sometimes walk alone.”*

— Johann Wolfgang Goethe

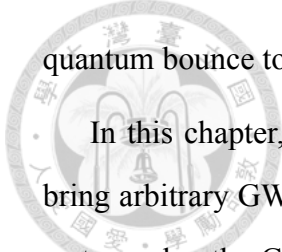
### 3.1 Overview

In the standard cosmological model the large-scale cosmic structures are originated from the primordial perturbations created through the quantum fluctuations during inflation. The inflationary process froze out the pair-created gravitons and thus generated the GWs as the by-product of inflation. The standard power spectrum of these primordial GWs on sub-horizon scales in a de Sitter expansion is

$$P_T^{\text{std}} = \frac{8\pi H^2}{k^3}, \quad (3.1)$$

where  $k$  is the wavenumber and  $H$  is supposed to be constant during inflation.

Recent studies considered the primordial GWs generated during the quantum bounce in LQC [30, 31]. They even parametrized the quantum effects in the power spectrum. However, there could be GWs even in the parent universe surviving the quantum bounce and manifesting themselves today with different features as compare with those studied before. Thus one of the major contributions of this chapter is to provide a new framework that enables us to evolve the pre-existing GWs from the parent universe through the



quantum bounce to the end of inflation and even to the present.

- In this chapter, we propose a new formalism that employs the transfer functions to bring arbitrary GWs from any given initial time to a designated final time. This enables us to evolve the GWs from the parent universe through deflation, the quantum bounce, inflation, and any epoch of our interest. In particular, we discuss GWs with the holonomy corrections [30, 31, 67]. Our formalism is so transparent that we are able to resolve, for example, the IR suppression problem [30]. We also show that our new approach using the transfer functions is equivalent to and produces same results as the Bogoliubov transformations [30].

In addition to the transfer-function formalism, in this chapter we shall propose the “field-free approximation” for the effective mass in the quantum bounce epoch, which in turn dramatically improves the accuracy in the predicted GW power spectrum.

We introduce the new formalism that employs transfer functions in Section 3.2. Then in Section 3.3 and Section 3.4 we calculate the transfer functions for all related epochs of cosmic evolution. In particular, the field-free approximation is proposed to improve on the handling of the effective mass in quantum bounce. In Section 3.5, we verify the consistency with the Bogoliubov transformations and consider additional but importantly related issues, including resolving the IR suppression problem and improving the accuracy of the predicted GW power spectrum using the field-free approximation. Finally, we summarize this chapter and give some conclusions in Section 3.7.

## 3.2 Gravitational Waves in LQC

### 3.2.1 Gravitaional-wave equation

The evolution of GWs in LQC can be described by the wave equation [68]

$$\frac{d^2}{d\eta^2} h_i^j + 2H \frac{d}{d\eta} h_i^j + (-\nabla^2 + m_Q^2) h_i^j = 0. \quad (3.2)$$

The GW functions are given by  $h_i^j = h_i^j(\eta, \mathbf{x})$  with  $h_1^1 = -h_2^2 = h_{\oplus}$  and  $h_2^1 = h_1^2 = h_{\otimes}$  in the transverse-traceless gauge. They are decomposed from the metric perturbations. The holonomy correction term  $m_Q$  is given by [68]

$$m_Q^2 = 16\pi a^2 \frac{\rho}{\rho_c} \left( \frac{2}{3}\rho - V \right), \quad (3.3)$$

which vanishes in a classical regime.

It is clear that there exists a damping term in the wave equation. It means that GWs will be diluted by the cosmic expansion. Therefore, it is more convenient to solve the wave equation and understand the physics by defining a new function  $u$  [30] in the comoving space:

$$u = u(\mathbf{x}, \eta) = \frac{ah_{\oplus}}{\sqrt{16\pi}} = \frac{ah_{\otimes}}{\sqrt{16\pi}}. \quad (3.4)$$

In the Fourier domain, the wave equation then becomes [30]:

$$\frac{d^2}{d\eta^2} \tilde{u}_{\mathbf{k}}(\eta) + (k^2 + m_{\text{eff}}^2) \tilde{u}_{\mathbf{k}}(\eta) = 0, \quad (3.5)$$

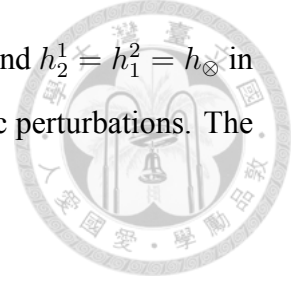
where

$$\tilde{u}_{\mathbf{k}} = \tilde{u}_{\mathbf{k}}(\eta) = \int \frac{d^3 k}{(2\pi)^3} u(\mathbf{x}, \eta) e^{-i\mathbf{k}\cdot\mathbf{x}}, \quad (3.6)$$

and the effective mass is defined as

$$m_{\text{eff}}^2 = m_Q^2 - \frac{1}{a} \frac{d^2 a}{d\eta^2}. \quad (3.7)$$

Figure 3.1 shows the effective mass as a function of the conformal time. The part for  $\eta < 0$  is not shown as it is expected to be almost time-symmetric with respect to  $\eta = 0$ . The blue dashed line is our numerical result, indicating the inaccuracy of other approximations which we shall discuss later. The effective mass is relatively large around the quantum bounce, meaning that the quantum effects acting on GWs become significant



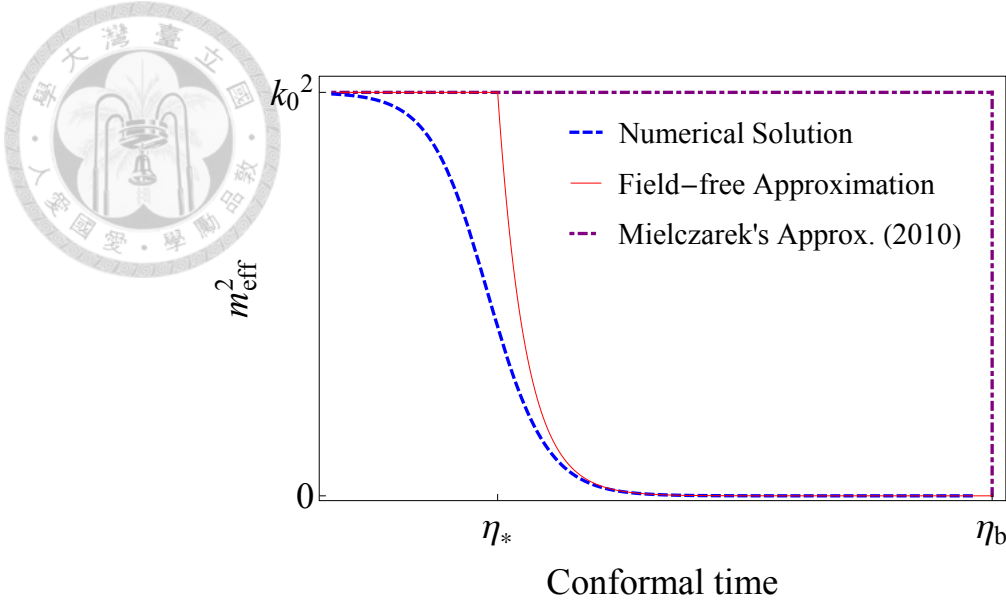


Figure 3.1: The effective mass as a function of the conformal time, evolving from the quantum bounce ( $\eta = 0$ ) to the beginning of inflation ( $\eta = \eta_b$ ).

near the quantum bounce. In addition, Equation (3.5) also tells us that the quantum effects behave much more obviously on larger scales (smaller  $k$ ). This feature provides critical insight into the observational tests for such quantum effects at the bounce.

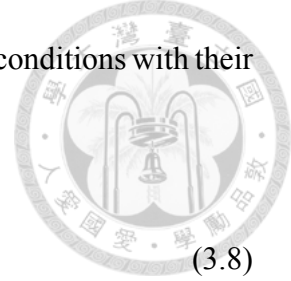
Such scale-dependent features can also be argued from a different perspective through the comoving coordinates. The wavenumber  $k$  is related to the comoving wavelength  $\lambda_k$  of the GW as  $\lambda_k \sim 2\pi/k$ . According to Equation (3.5), the GWs reduce to plane waves on small scales. On the other hand, the comoving Hubble radius goes to infinity at the quantum bounce, which is the turning point ( $H = 0$ ) of the cosmic contraction. It means that the whole universe is in causal connection due to strong quantum effects at the bounce. For a GW originally on super-horizon scales evolving through the quantum bounce, it will suddenly oscillate after the horizon entry near the quantum bounce. Therefore, we expect that the large-scale power spectrum in such scenarios to be potentially different from that in the standard model.

### 3.2.2 Transfer functions

Equation (3.6), which governs the evolution of the GWs, is a linear second-order ordinary differential equation of  $\tilde{u}_k(\eta)$ , so for any given set of initial and final times there must

exist certain transfer functions connecting any arbitrarily given initial conditions with their final solutions. In other words, if we define

$$\tilde{\mathbf{U}}_{\mathbf{k}}(\eta) \equiv \begin{bmatrix} \tilde{u}_{\mathbf{k}}(\eta') \\ \frac{d\tilde{u}_{\mathbf{k}}(\eta')}{d\eta'} \end{bmatrix}_{\eta'=\eta}, \quad (3.8)$$



then the above statement goes as

$$\tilde{\mathbf{U}}_{\mathbf{k}}(\eta_f) = \mathbf{T}_{\mathbf{k}}(\eta_i, \eta_f) \tilde{\mathbf{U}}_{\mathbf{k}}(\eta_i), \quad (3.9)$$

where  $\tilde{\mathbf{U}}_{\mathbf{k}}(\eta_i)$  is the initial condition at  $\eta_i$ ,  $\tilde{\mathbf{U}}_{\mathbf{k}}(\eta_f)$  is the final state at  $\eta_f$ , and  $\mathbf{T}_{\mathbf{k}}(\eta_i, \eta_f)$  is a  $2 \times 2$  transfer matrix that contains, in general, four independent transfer functions:

$$\mathbf{T}_{\mathbf{k}}(\eta_i, \eta_f) = \begin{bmatrix} T(\mathbf{k})_{11} & T(\mathbf{k})_{12} \\ T(\mathbf{k})_{21} & T(\mathbf{k})_{22} \end{bmatrix}. \quad (3.10)$$

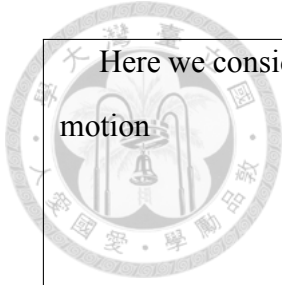
These four transfer functions are independent of the initial condition and are purely determined by the evolution equation, whose form changes in different epochs following different cosmological background dynamics.

If the evolutionary history of the universe can be divided into  $N$  epochs in sequence, namely  $[\eta_i^x, \eta_f^x]$  ( $x = 1 \dots N$ ), then the overall transfer matrix  $\mathbf{T}_{\mathbf{k}}(\eta_i, \eta_f)$  can be obtained by combining the transfer matrices  $\mathbf{T}_{\mathbf{k}}^x(\eta_i^x, \eta_f^x)$  of each individual epoch:

$$\mathbf{T}_{\mathbf{k}}(\eta_i, \eta_f) = \prod_{x=1}^N \mathbf{T}_{\mathbf{k}}^x(\eta_i^x, \eta_f^x). \quad (3.11)$$

For a GW equation that can be solved analytically, its corresponding transfer functions can be easily derived.

On the following page, we use a toy example to demonstrate how we derive the transfer functions from the analytical solutions of a linear equation of motion.



Here we consider a simple harmonic oscillator  $x = x(t)$  which follows the equation of motion

$$\ddot{x} + \omega^2 x = 0.$$

The solution is well-known as

$$x(t) = A \cos \omega t + B \sin \omega t,$$

where  $A$  and  $B$  are arbitrary coefficients, which may be determined by the initial conditions at  $t_i$  through

$$\begin{cases} x(t_i) = A \cos \omega t_i + B \sin \omega t_i, \\ \dot{x}(t_i) = -\omega A \sin \omega t_i + \omega B \cos \omega t_i, \end{cases}$$

which lead to

$$\begin{cases} A = \cos \omega t_i x(t_i) - \frac{\sin \omega t_i}{\omega} \dot{x}(t_i), \\ B = \sin \omega t_i x(t_i) + \frac{\cos \omega t_i}{\omega} \dot{x}(t_i). \end{cases}$$

At the final time  $t_f$  we then have

$$\begin{cases} x(t_f) = \cos(\omega \Delta t) x(t_i) + \frac{1}{\omega} \sin(\omega \Delta t) \dot{x}(t_i), \\ \dot{x}(t_f) = -\omega \sin(\omega \Delta t) x(t_i) + \cos(\omega \Delta t) \dot{x}(t_i). \end{cases}$$

Therefore the transfer function matrix for the equation of motion is

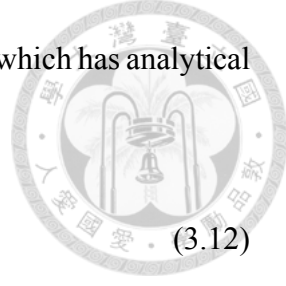
$$\mathbf{T}_\omega(t_i, t_f) = \begin{bmatrix} \cos(\omega \Delta t) & \frac{1}{\omega} \sin(\omega \Delta t) \\ -\omega \sin(\omega \Delta t) & \cos(\omega \Delta t) \end{bmatrix},$$

where  $\Delta t \equiv t_f - t_i$ . We note that this is obviously a rotation matrix of  $SO(2)$  group which rotates the coordinates in the Cartesian plane counter-clockwise by an angle  $\omega \Delta t$  about the origin in Euclidean space.

In general, for a linear second-order ordinary differential equation which has analytical

solutions

$$\tilde{u}_k(\eta) = AF_k(\eta) + BG_k(\eta), \quad (3.12)$$



the transfer functions are

$$T(k)_{11} = \frac{\frac{dG_k^i}{d\eta} F_k^f - \frac{dF_k^i}{d\eta} G_k^f}{F_k^i \frac{dG_k^i}{d\eta} - G_k^i \frac{dF_k^i}{d\eta}}, \quad (3.13a)$$

$$T(k)_{12} = \frac{F_k^i G_k^f - G_k^i F_k^f}{F_k^i \frac{dG_k^i}{d\eta} - G_k^i \frac{dF_k^i}{d\eta}}, \quad (3.13b)$$

$$T(k)_{21} = \frac{\frac{dG_k^i}{d\eta} \frac{dF_k^f}{d\eta} - \frac{dF_k^i}{d\eta} \frac{dG_k^f}{d\eta}}{F_k^i \frac{dG_k^i}{d\eta} - G_k^i \frac{dF_k^i}{d\eta}}, \quad (3.13c)$$

$$T(k)_{22} = \frac{F_k^i \frac{dG_k^f}{d\eta} - G_k^i \frac{dF_k^f}{d\eta}}{F_k^i \frac{dG_k^i}{d\eta} - G_k^i \frac{dF_k^i}{d\eta}}, \quad (3.13d)$$

where the superscripts “i” and “f” over  $F_k$  and  $G_k$  indicate arguments  $\eta_i$  and  $\eta_f$ . There are four degrees of freedom simply because  $F_k^i$ ,  $G_k^i$ ,  $F_k^f$ , and  $G_k^f$  are independent. In the system of simple harmonic oscillation that we introduced as the toy example in the previous page, we have  $F_\omega(t) = \cos \omega t$  and  $G_\omega(t) = \sin \omega t$ . There are three relations between these four:

$$F_\omega(t_i)^2 + G_\omega(t_i)^2 = 1,$$

$$F_\omega(t_f)^2 + G_\omega(t_f)^2 = 1,$$

$$F_\omega(\Delta t)^2 + G_\omega(\Delta t)^2 = 1,$$

where

$$F_\omega(\Delta t) = F_\omega(t_f - t_i) = F_\omega(t_f)F_\omega(t_i) + G_\omega(t_f)G_\omega(t_i),$$

$$G_\omega(\Delta t) = G_\omega(t_f - t_i) = G_\omega(t_f)F_\omega(t_i) - F_\omega(t_f)G_\omega(t_i),$$

and thus only one degree of freedom parametrized by the rotation angle (i.e.  $\omega\Delta t$ ).

### 3.2.3 Numerical approach to transfer functions

Now we demonstrate how to numerically obtain the transfer matrix of given  $\eta_i$  and  $\eta_f$ .

In principle we could numerically evolve any arbitrary initial condition  $\tilde{\mathbf{U}}_k(\eta_i)$  to obtain its final state  $\tilde{\mathbf{U}}_k(\eta_f)$ , and then derive the corresponding transfer functions, which should be valid for any initial condition. As shown in Equation (3.9),  $\mathbf{T}_k(\eta_i, \eta_f)$  is a  $2 \times 2$  matrix with four transfer functions, so we need four equations to derive them. Equation (3.8) actually provides two “independent” equations, so what we need to do is simply to evolve two different initial conditions  $\tilde{\mathbf{U}}_k^{i(a)} \equiv \tilde{\mathbf{U}}_k^{(a)}(\eta_i)$  ( $a = 1, 2$ ) into their final states  $\tilde{\mathbf{U}}_k^{f(a)} \equiv \tilde{\mathbf{U}}_k^{(a)}(\eta_f)$ , and then we are ready to solve for the four transfer functions using:

$$\tilde{u}_k^{f(a)} = T(\mathbf{k})_{11} \tilde{u}_k^{i(a)} + T(\mathbf{k})_{12} \frac{d\tilde{u}_k}{d\eta}^{i(a)}, \quad (3.14a)$$

$$\frac{d\tilde{u}_k}{d\eta}^{f(a)} = T(\mathbf{k})_{21} \tilde{u}_k^{i(a)} + T(\mathbf{k})_{22} \frac{d\tilde{u}_k}{d\eta}^{i(a)}, \quad (3.14b)$$

where  $a = 1, 2$ . The explicit forms of the solved transfer functions are:

$$T(\mathbf{k})_{11} = \frac{\tilde{u}_k^{f(1)} \frac{d\tilde{u}_k}{d\eta}^{i(2)} - \tilde{u}_k^{f(2)} \frac{d\tilde{u}_k}{d\eta}^{i(1)}}{\tilde{u}_k^{i(1)} \frac{d\tilde{u}_k}{d\eta}^{i(2)} - \tilde{u}_k^{i(2)} \frac{d\tilde{u}_k}{d\eta}^{i(1)}}, \quad (3.15a)$$

$$T(\mathbf{k})_{12} = \frac{\tilde{u}_k^{f(1)} \tilde{u}_k^{i(2)} - \tilde{u}_k^{f(2)} \tilde{u}_k^{i(1)}}{\frac{d\tilde{u}_k}{d\eta}^{i(1)} \tilde{u}_k^{i(2)} - \frac{d\tilde{u}_k}{d\eta}^{i(2)} \tilde{u}_k^{i(1)}}, \quad (3.15b)$$

$$T(\mathbf{k})_{21} = \frac{\frac{d\tilde{u}_k}{d\eta}^{f(1)} \frac{d\tilde{u}_k}{d\eta}^{i(2)} - \frac{d\tilde{u}_k}{d\eta}^{f(2)} \frac{d\tilde{u}_k}{d\eta}^{i(1)}}{\tilde{u}_k^{i(1)} \frac{d\tilde{u}_k}{d\eta}^{i(2)} - \tilde{u}_k^{i(2)} \frac{d\tilde{u}_k}{d\eta}^{i(1)}}, \quad (3.15c)$$

$$T(\mathbf{k})_{22} = \frac{\frac{d\tilde{u}_k}{d\eta}^{f(1)} \tilde{u}_k^{i(2)} - \frac{d\tilde{u}_k}{d\eta}^{f(2)} \tilde{u}_k^{i(1)}}{\frac{d\tilde{u}_k}{d\eta}^{i(1)} \tilde{u}_k^{i(2)} - \frac{d\tilde{u}_k}{d\eta}^{i(2)} \tilde{u}_k^{i(1)}}. \quad (3.15d)$$

This provides a complete recipe for obtaining accurate numerical results. We always cross check our numerical results with the analytical results, wherever the latter are available. The numerical results are also useful for verifying our approximations where exact analytical solutions are not available.

Because of the cosmological principle, we shall drop the directional dependence of  $\mathbf{k}$  to consider only  $k \equiv |\mathbf{k}|$  in the following discussions.



### 3.3 Inflationary and Deflationary Epochs

#### 3.3.1 The slow-roll inflation

The definition of inflation is simply that the universe undergoes an era of accelerated expansion (see Subsection 2.2.2 for a detailed review). After the quantum bounce there are two periods when inflation occurs: the cosmological inflation in the standard cosmology and the super-inflationary phase near the quantum bounce. In the following, we focus on the former, which is necessary for solving the cosmological conundrums.

To investigate the inflationary epoch, we adopt the PSRA [53, 55]. Under the PSRA, the chaotic inflation may be approximated as the de Sitter expansion, when the scale factor grows exponentially so that the Hubble parameter stays as a constant  $H_{\text{dS}}$ . The scale factors at the beginning ( $\eta = \eta_b$ ) and the end ( $\eta = \eta_e$ ) of inflation are denoted as  $a_b \equiv a(\eta_b)$  and  $a_e \equiv a(\eta_e)$  respectively. The definition of conformal time (see e.g. Reference [17]) thus gives

$$\eta' = \int_{a_e}^a \frac{da}{Ha^2} = \frac{1}{H_{\text{dS}}} \int_{a_e}^a \frac{da}{a^2} = \frac{-1}{aH_{\text{dS}}} + \frac{1}{a_e H_{\text{dS}}}. \quad (3.16)$$

We note that  $\eta'$  is originated at the end of inflation while  $\eta$  is originated at the quantum bounce, so  $\eta'$  is negative during inflation. These are related as:

$$\eta' = \eta - \eta_e. \quad (3.17)$$

For more review on inflationary cosmology please refer to References [66] and [21].

#### 3.3.2 Transfer functions for inflation

In this epoch the quantum correction term  $m_Q$  in Equation (3.3) vanishes, therefore Equation (3.5) becomes

$$\frac{d^2}{d\eta^2} \tilde{u}_k + \left( k^2 - \frac{1}{a} \frac{d^2 a}{d\eta^2} \right) \tilde{u}_k = 0. \quad (3.18)$$



In the regime of de Sitter expansion, Equation (3.18) can be rewritten as:

$$\frac{d^2}{d\eta_I^2} \tilde{u}_k + \left( k^2 - \frac{2}{\eta_I^2} \right) \tilde{u}_k = 0, \quad \eta_I \equiv \frac{1}{a_e H_{dS}} - \eta', \quad (3.19)$$

where  $\eta_I$  denotes the conformal time defined in the inflationary epoch. It is obvious that Equation (3.19) is in the form of a Bessel differential equation of order 3/2, so its solution should be simply the linear sum of Bessel functions:

$$\tilde{u}_k^I(\eta_I) = A^I \sqrt{\eta_I} J_{3/2}(k\eta_I) + B^I \sqrt{\eta_I} J_{-3/2}(k\eta_I), \quad (3.20)$$

where  $J$  is the Bessel function of the first kind. Here we use the superscript “I” to denote quantities specifically for the inflationary epoch. The coefficients  $A^I$  and  $B^I$  may be determined by the initial conditions. More details about the mathematics of Bessel differential equation of order 3/2 are provided in Subsection 3.3.4. The transfer functions corresponding to Equation (3.19) are presented as Equation (3.34) in Subsection 3.3.4 as well.

By taking the limit  $a_e \gg a_b$ , the transfer functions  $\mathbf{T}^I(k) \equiv \mathbf{T}_k(\eta_b, \eta_e)$  as defined in Equations (3.9) and (3.10) for the inflationary epoch can be obtained as:

$$T^I(k)_{11} = \frac{a_e H_{dS}}{k} [\sin(k\Delta\eta_I) - j_1(k\Delta\eta_I)], \quad (3.21a)$$

$$T^I(k)_{12} = \frac{a_e H_{dS}}{k^2} [\cos(k\Delta\eta_I) - j_0(k\Delta\eta_I)], \quad (3.21b)$$

$$T^I(k)_{21} = -\frac{a_e^2 H_{dS}^2}{k} [\sin(k\Delta\eta_I) - j_1(k\Delta\eta_I)], \quad (3.21c)$$

$$T^I(k)_{22} = -\frac{a_e^2 H_{dS}^2}{k^2} [\cos(k\Delta\eta_I) - j_0(k\Delta\eta_I)], \quad (3.21d)$$

where  $\Delta\eta_I \equiv \eta_e - \eta_b$  is the duration of inflation, and the  $j$ ’s are the spherical Bessel functions of the first kind. These four transfer functions are shown in Figure 3.2, where such analytical results are numerically verified using Equation (3.15) at high accuracy.

Although these transfer functions are obtained in a purely classical manner, they are consistently useful in a quantum mechanical problem. Considering the quantum fluctua-

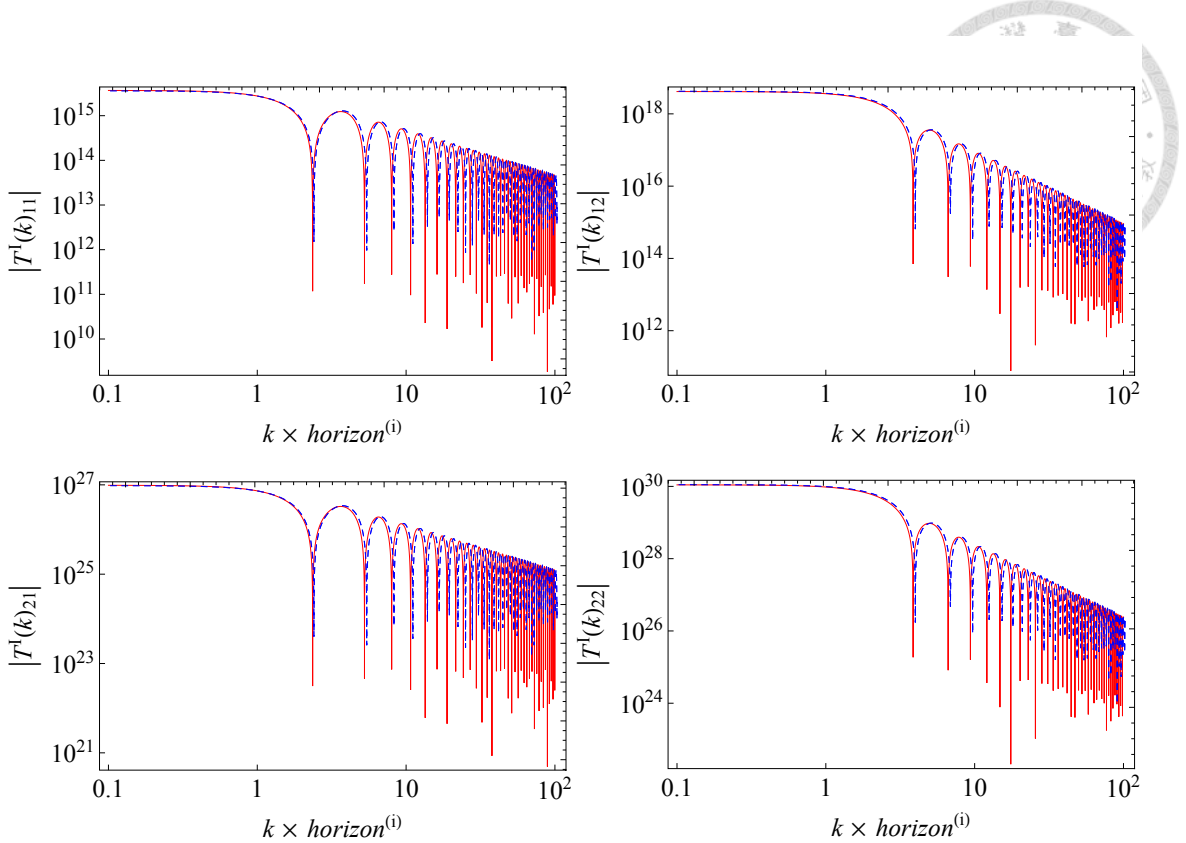


Figure 3.2: The numerical (blue dashed) and analytical (red solid) results for the transfer functions of GWs in de Sitter inflation with chaotic potential. The consistency between the two is obvious.

tions in the Minkowski spacetime (see e.g. Reference [17])

$$\tilde{u}_k(\eta_b) = \frac{1}{\sqrt{2k}} e^{-ik\eta_b} \quad \text{and} \quad \frac{d\tilde{u}_k}{d\eta}(\eta_b) = \frac{-ik}{\sqrt{2k}} e^{-ik\eta_b}, \quad (3.22)$$

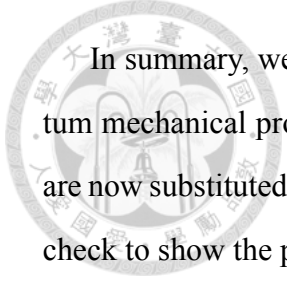
with the sub-horizon (large- $k$ ) limit

$$\lim_{k \rightarrow \infty} \mathbf{T}^I(k) = \begin{bmatrix} \frac{a_e H_{\text{dS}}}{k} \sin(k\Delta\eta_l) & \frac{a_e H_{\text{dS}}}{k^2} \cos(k\Delta\eta_l) \\ -\frac{a_e^2 H_{\text{dS}}^2}{k} \sin(k\Delta\eta_l) & -\frac{a_e^2 H_{\text{dS}}^2}{k^2} \cos(k\Delta\eta_l) \end{bmatrix}, \quad (3.23)$$

we can obtain the primordial tensor power spectrum at the end of inflation as

$$\lim_{k \rightarrow \infty} P_T^{\text{dS}}(k) = \frac{16\pi}{a_e^2} |\tilde{u}_k(\eta_e)|^2 = \frac{8\pi H_{\text{dS}}^2}{k^3} = P_T^{\text{std}}(k). \quad (3.24)$$

This shows the consistency with the result from quantizing the GWs considered before.



In summary, we conclude that the transfer functions successfully classicalize a quantum mechanical problem. The quantization process and the Bogoliubov transformations are now substituted by simple algebraic calculations. We shall provide further consistency check to show the power of the transfer functions later in this chapter.

### 3.3.3 Transfer functions for deflation

As studied in Subsection 2.3.5, there must be a contractive process before reaching the limit to trigger the quantum bounce if there exists a parent universe. We thus consider in this process a possible deflation defined by Equation (2.36). In addition to the primordial perturbations, which are originated from the quantum bounce and inflation, in this subsection we also derive the transfer functions for the deflationary epoch, extending the framework in literature well through the bounce backwards in time into the parent universe.

To handle deflation, we also employ the PSRA. Again the Hubble parameter is expected to vary so slowly and thus well approximated by the “de Sitter contraction”, where the scale factor decays exponentially so that the Hubble parameter stays as a negative constant  $H_{\text{dS}}^{\text{D}} < 0$ . We can then define the conformal time with an origin at the beginning of deflation as

$$\eta'_{\text{D}} = \int_{a_b^{\text{D}}}^a \frac{da}{Ha^2} = \frac{1}{H_{\text{dS}}^{\text{D}}} \int_{a_b^{\text{D}}}^a \frac{da}{a^2} = \frac{1}{H_{\text{dS}}^{\text{D}}} \left( \frac{-1}{a} + \frac{1}{a_b^{\text{D}}} \right), \quad (3.25)$$

which stays positive during deflation since  $a < a_b^{\text{D}}$ , and that

$$\eta'_{\text{D}} = \eta - \eta_b^{\text{D}}. \quad (3.26)$$

The superscript or subscript “D” denotes for deflation. The equation of  $\tilde{u}_k$  in the deflationary epoch can now be written as

$$\frac{d^2}{d\eta_{\text{D}}^2} \tilde{u}_k + \left( k^2 - \frac{2}{\eta_{\text{D}}^2} \right) \tilde{u}_k = 0, \quad \eta_{\text{D}} \equiv \eta'_{\text{D}} - \frac{1}{a_b^{\text{D}} H_{\text{dS}}^{\text{D}}}. \quad (3.27)$$

This is in the form of a Bessel differential equation of order 3/2 so its general solution is

$$\tilde{u}_k^D(\eta_D) = A^D \sqrt{\eta_D} J_{3/2}(k\eta_D) + B^D \sqrt{\eta_D} J_{-3/2}(k\eta_D), \quad (3.28)$$

where the coefficients  $A^D$  and  $B^D$  may be determined by the initial conditions. The transfer functions  $\mathbf{T}^D(k) \equiv \mathbf{T}_k^D(\eta_b^D, \eta_e^D)$  corresponding to Equation (3.27) are presented as Equation (3.40) in Subsection 3.3.4.

As we shall argue in the next subsection,  $\mathbf{T}^D(k)$  should be the inverse matrix of  $\mathbf{T}^I(k)$  if the cosmic background is time-symmetric with respect to the quantum bounce. More details about the transfer functions for Bessel differential equation of order 3/2 are provided below.

### 3.3.4 Transfer functions and their symmetry in de Sitter space

The Bessel equation is a linear second-order ordinary differential equation

$$x^2 \frac{d^2 u}{dx^2} + x \frac{du}{dx} + (x^2 - n^2)u = 0. \quad (3.29)$$

A modified expression of the Bessel differential equation of order  $n$  is [69]

$$\frac{d^2 u}{dx^2} - \frac{2\alpha - 1}{x} \frac{du}{dx} + \left( \beta^2 \gamma^2 x^{2\gamma-2} + \frac{\alpha^2 - n^2 \gamma^2}{x^2} \right) u = 0 \quad (3.30)$$

Here the parameters  $\alpha, \beta, \gamma$  and  $n$  are purely mathematical, not related to the cosmological context. The solutions are therefore:

$$u(x) = \begin{cases} x^\alpha [AJ_n(\beta x^\gamma) + BY_n(\beta x^\gamma)] & \text{for integer } n \\ x^\alpha [AJ_n(\beta x^\gamma) + BJ_{-n}(\beta x^\gamma)] & \text{for non-integer } n. \end{cases} \quad (3.31)$$

By comparing Equations (3.19) and (3.27) with Equation (3.30), we see that both Equations (3.19) and (3.27) are Bessel differential equation of order 3/2, and that

$$\{\alpha, \beta, \gamma, n\} = \left\{ \frac{1}{2}, k, 1, \frac{3}{2} \right\}. \quad (3.32)$$



Substituting these numbers into Equation (3.31) gives the general solutions as

$$u_k(x) = \sqrt{x} [AJ_{3/2}(kx) + BJ_{-3/2}(kx)]. \quad (3.33)$$

The resulting transfer functions  $\mathbf{T}(k) \equiv \mathbf{T}_k(x_1, x_2)$  that connect the initial state  $u_k(x_1)$  with the final state  $u_k(x_2)$  are

$$T(k)_{11} = F_4(kx_1)F_2(kx_2) - F_3(kx_1)F_1(kx_2); \quad (3.34a)$$

$$T(k)_{12} = \frac{1}{k} \{F_1(kx_1)F_2(kx_2) - F_2(kx_1)F_1(kx_2)\}; \quad (3.34b)$$

$$T(k)_{21} = k \{F_4(kx_1)F_3(kx_2) + F_3(kx_1)F_4(kx_2)\}; \quad (3.34c)$$

$$T(k)_{22} = F_1(kx_1)F_3(kx_2) + F_2(kx_1)F_4(kx_2). \quad (3.34d)$$

with

$$\begin{aligned} F_1(x) &\equiv \cos(x) - j_0(x); & F_2(x) &\equiv \sin(x) - y_0(x); \\ F_3(x) &\equiv \cos(x) + y_1(x); & F_4(x) &\equiv \sin(x) - j_1(x). \end{aligned} \quad (3.35)$$

where the  $y$ 's are the spherical Bessel function of the second kind. These results for the transfer functions are exact without using any approximation.

For the de Sitter expansion, where Equation (3.16) is satisfied, we have

$$x_2 = \frac{1}{a_e H_{\text{dS}}} \quad \text{and} \quad x_1 = x_2 + \Delta\eta_{\text{I}}. \quad (3.36)$$

The transfer functions for the inflationary epoch are therefore

$$T^{\text{I}}(k)_{11} = F_4(k\Delta\eta_{\text{I}})F_2\left(\frac{k}{a_e H_{\text{dS}}}\right) - F_3(k\Delta\eta_{\text{I}})F_1\left(\frac{k}{a_e H_{\text{dS}}}\right); \quad (3.37a)$$

$$T^{\text{I}}(k)_{12} = \frac{1}{k} \left[ F_1(k\Delta\eta_{\text{I}})F_2\left(\frac{k}{a_e H_{\text{dS}}}\right) - F_2(k\Delta\eta_{\text{I}})F_1\left(\frac{k}{a_e H_{\text{dS}}}\right) \right]; \quad (3.37b)$$

$$T^{\text{I}}(k)_{21} = k \left[ F_4(k\Delta\eta_{\text{I}})F_3\left(\frac{k}{a_e H_{\text{dS}}}\right) + F_3(k\Delta\eta_{\text{I}})F_4\left(\frac{k}{a_e H_{\text{dS}}}\right) \right]; \quad (3.37c)$$

$$T^{\text{I}}(k)_{22} = F_1(k\Delta\eta_{\text{I}})F_3\left(\frac{k}{a_e H_{\text{dS}}}\right) + F_2(k\Delta\eta_{\text{I}})F_4\left(\frac{k}{a_e H_{\text{dS}}}\right). \quad (3.37d)$$

When taking the limit  $a_e \gg a_b$ , which is equivalent to  $x_1 \gg x_2$ , Equations (3.37) reduce exactly to Equations (3.21).

An obvious fact is that the determinants of  $T(k)$  and  $T^I(k)$  are both unity

$$\det(T(k)) = \det(T^I(k)) = 1. \quad (3.38)$$

However, the determinant of the  $T^I(k)$  in Equations (3.21) is zero, not unity. This indicates that the linear independence among the transfer functions is broken when taking the limit  $a_e \gg a_b$ . Therefore, we should be very careful whenever we employ Equations (3.21), which are not generally valid.

For the de Sitter contraction, where Equation (3.25) is satisfied, we have

$$x_1 = \frac{-1}{a_b^D H_{dS}^D} \quad \text{and} \quad x_2 = x_1 + \Delta\eta_D. \quad (3.39)$$

The transfer functions for the deflationary epoch are therefore

$$T^D(k)_{11} = F_4\left(\frac{-k}{a_e^D H_{dS}^D}\right) F_2(k\Delta\eta_D) - F_3\left(\frac{-k}{a_e^D H_{dS}^D}\right) F_1(k\Delta\eta_D); \quad (3.40a)$$

$$T^D(k)_{12} = \frac{1}{k} \left[ F_1\left(\frac{-k}{a_e^D H_{dS}^D}\right) F_2(k\Delta\eta_D) - F_2\left(\frac{-k}{a_e^D H_{dS}^D}\right) F_1(k\Delta\eta_D) \right]; \quad (3.40b)$$

$$T^D(k)_{21} = k \left[ F_4\left(\frac{-k}{a_e^D H_{dS}^D}\right) F_3(k\Delta\eta_D) + F_3\left(\frac{-k}{a_e^D H_{dS}^D}\right) F_4(k\Delta\eta_D) \right]; \quad (3.40c)$$

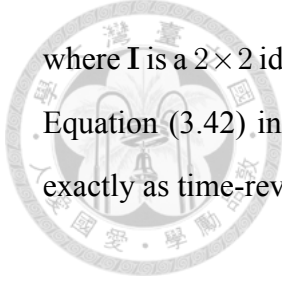
$$T^D(k)_{22} = F_1\left(\frac{-k}{a_e^D H_{dS}^D}\right) F_3(k\Delta\eta_D) + F_2\left(\frac{-k}{a_e^D H_{dS}^D}\right) F_4(k\Delta\eta_D). \quad (3.40d)$$

In a cosmic background that is time-symmetric to the quantum bounce, it is natural to expect that deflation and inflation are also time-symmetric to each other:

$$\Delta\eta_I = \Delta\eta_D \quad \text{and} \quad a_e H_{dS} = -a_b^D H_{dS}^D. \quad (3.41)$$

In such cases, we expect the transfer matrices for inflation and deflation to satisfy

$$T^I(k) \times T^D(k) = T^D(k) \times T^I(k) = I, \quad (3.42)$$



where  $\mathbf{I}$  is a  $2 \times 2$  identity matrix. This is indeed verified by our results of transfer matrices. Equation (3.42) in turn implies that the evolution of GWs in these two stages behaves exactly as time-reversed with each other.

## 3.4 Quantum Bounce Epoch

### 3.4.1 Definition of quantum bounce epoch

The definition of quantum bounce epoch is the period between cosmological deflation and cosmological inflation. It undergoes both the classical and quantum regimes, including the super-deflationary phase, the quantum bounce and the super-inflationary phase.

To compare our results to the literature, in Sections 3.4 and 3.5, we first consider the Minkowski vacuum, which comes before the quantum bounce epoch, as the first stage for the primordial perturbations to travel through rather than deflation. We here define the quantum bounce epoch to begin when the quantum effect of the spacetime becomes considerable (the quantum gravity regime) and then to end at the beginning of inflation.

In Equation (2.25), the discreteness variable  $\bar{\mu}$  is directly related to the holonomy corrections, so we could use  $\bar{\mu}c_h$  to quantify the quantum gravity effect. Thus the quantum gravity regime can be defined as the period when

$$0.01 < \bar{\mu}c_h < \pi - 0.01. \quad (3.43)$$

The conformal time at the beginning of the quantum gravity regime  $\eta_i$  can then be defined through

$$\bar{\mu}(\eta_i)c_h(\eta_i) = \pi - 0.01. \quad (3.44)$$

We note that  $\bar{\mu}c_h$  goes to zero when  $t \gg 0$  with the Ashtekar variables reduced to the cosmological parameters in the standard cosmology.

Although this definition for the quantum gravity regime is lack of strict physical justification, it is well motivated enough and convenient for us to discuss the transfer functions

and the concomitant breakthroughs in these two sections.



### 3.4.2 Field-free approximation for effective mass

In our framework, a decisive factor for the evolution of GWs is the behavior of the effective mass in Equation (3.5). During the quantum bounce epoch, the quantum correction term  $m_Q^2$  is critical and the effective mass depends on both the background dynamics and the scalar potential, as indicated in Equations (3.3) and (3.7). In a previous study by Mielczarek *et al.* [30], the effective mass is conveniently assumed to be a constant ( $k_0$ ) during the entire quantum bounce epoch, as shown by the purple dash-dotted line in Figure 3.1. However, it is largely discrepant from the numerical result, as presented by the blue dashed curve. Thus we propose a new approximation for the effective mass in this subsection, and will compare its results with literature in Subsection 3.5.1.

We approximate the effective mass in the following way. The simplest case is to consider a scalar-field free cosmic background during the quantum bounce epoch. An exact form of such an effective mass was derived as a function of proper time in Reference [67]. Its corresponding ‘‘approximated’’ function of the conformal time was then provided but only in the classical limit where  $|t| \rightarrow \infty$  [67]. Based on this result, we build a new analytical form to approximate the numerical solution of the effective mass:

$$m_{\text{eff}}^2 = \begin{cases} k_0^2 & \text{for } -\eta_* < \eta < \eta_*, \\ \frac{1}{4\eta_*^2} & \text{for } \eta_e^D \leq \eta \leq -\eta_* \text{ and } \eta_* \leq \eta \leq \eta_b, \end{cases} \quad (3.45)$$

where [67]

$$k_0^2 \equiv m_{\text{eff}}^2(0) = \frac{16\pi^2\gamma^2\Delta\pi_\phi^4}{9(\frac{4}{3}\pi\gamma^2\Delta\pi_\phi^2)^{5/3}}, \quad (3.46)$$

and

$$\frac{1}{4\eta_*^2} = k_0^2, \quad (3.47)$$

with  $\eta_* > 0$ . We call Equation (3.45) as the field-free approximation, which is shown as the red solid curve in Figure 3.1.

As mathematically argued before, the quantum effect for GWs is negligible on small scales (large  $k$ ) but critical on large scales (small  $k$ ). Its physical reason is that when a large-scale GW propagates through the quantum bounce, it experiences a longer  $m_{\text{eff}}^2$ -dominated period than a small-scale GW. Therefore, the inaccuracy of any approximation for the  $m_{\text{eff}}^2$  is expected to be larger on large scales (small  $k$ ).

### 3.4.3 Analytical solutions with field-free approximation

With the approximation of Equation (3.45), the quantum bounce epoch can be further divided into three stages: left, middle, and right, along the axis of conformal time. We shall use the superscripts “L”, “M”, and “R” respectively to label them.

Under the field-free approximation, the effective mass in the middle stage is a constant. The GWs thus propagate like plane waves:

$$\frac{d^2}{d\eta^2} \tilde{u}_k + k_*^2 \tilde{u}_k = 0, \quad (3.48)$$

where  $k_* \equiv \sqrt{k^2 + k_0^2}$  is the effective wavenumber of the plane waves (simple harmonic oscillation). The general solutions can be obtained as:

$$\tilde{u}_k^M(\eta) = A^M \cos(k_* \eta) + B^M \sin(k_* \eta), \quad (3.49)$$

where the coefficients  $A^M$  and  $B^M$  may be determined by the initial conditions. Thus the corresponding transfer functions are

$$\mathbf{T}^M(k) \equiv \mathbf{T}_k^M(-\eta_*, \eta_*) = \begin{bmatrix} \cos(2k_* \eta_*) & \frac{1}{k_*} \sin(2k_* \eta_*) \\ -k_* \sin(2k_* \eta_*) & \cos(2k_* \eta_*) \end{bmatrix}. \quad (3.50)$$

In the left and right stages, the equation of  $\tilde{u}_k$  is the same because the effective mass is exactly time-symmetric with respect to the quantum bounce. According to Equation (3.45),



we have

$$\frac{d^2}{d\eta^2}\tilde{u}_k + \left(k^2 + \frac{1}{4\eta^2}\right)\tilde{u}_k = 0. \quad (3.51)$$

This is obviously a Bessel equation of order zero.

First in the right stage ( $\eta > 0$ ), the general solutions are

$$\tilde{u}_k^R(\eta) = A^R \sqrt{\eta} J_0(k\eta) + B^R \sqrt{\eta} Y_0(k\eta), \quad (3.52)$$

where  $J$  and  $Y$  are the Bessel functions of the first kind and the second kind respectively, and coefficients  $A^R$  and  $B^R$  may be determined by the initial conditions. The corresponding transfer functions  $\mathbf{T}^R(k) \equiv \mathbf{T}_k^R(\eta_*, \eta_b)$  are

$$T^R(k)_{11} = \frac{1}{D(\eta_*)} \sqrt{\frac{\eta_b}{\eta_*}} [C_Y(\eta_*) J_0(k\eta_b) - C_J(\eta_*) Y_0(k\eta_b)], \quad (3.53a)$$

$$T^R(k)_{12} = \frac{\sqrt{\eta_* \eta_b}}{D(\eta_*)} [J_0(k\eta_*) Y_0(k\eta_b) - Y_0(k\eta_*) J_0(k\eta_b)], \quad (3.53b)$$

$$T^R(k)_{21} = \frac{1}{D(\eta_*)} \frac{1}{\sqrt{\eta_* \eta_b}} [C_Y(\eta_*) C_J(\eta_b) - C_J(\eta_*) C_Y(\eta_b)], \quad (3.53c)$$

$$T^R(k)_{22} = \frac{1}{D(\eta_*)} \sqrt{\frac{\eta_*}{\eta_b}} [J_0(k\eta_*) C_Y(\eta_b) - Y_0(k\eta_*) C_J(\eta_b)], \quad (3.53d)$$

where

$$C_Y(\eta) = \frac{1}{2} Y_0(k\eta) + \eta \frac{d}{d\eta} Y_0(k\eta), \quad (3.54)$$

$$C_J(\eta) = \frac{1}{2} J_0(k\eta) + \eta \frac{d}{d\eta} J_0(k\eta), \quad (3.55)$$

$$D(\eta) = C_Y(\eta) J_0(k\eta) - C_J(\eta) Y_0(k\eta). \quad (3.56)$$

Similarly in the left stage ( $\eta < 0$ ), the general solutions are

$$\tilde{u}_k^L(\eta) = A^L \sqrt{-\eta} J_0(-k\eta) + B^L \sqrt{-\eta} Y_0(-k\eta), \quad (3.57)$$

where the coefficients  $A^L$  and  $B^L$  may be determined by the initial conditions. The cor-

responding transfer functions  $\mathbf{T}^L(k) \equiv \mathbf{T}_k^L(\eta_i, -\eta_*)$  are

$$T^L(k)_{11} = \frac{1}{D(-\eta_i)} \sqrt{\frac{\eta_*}{-\eta_i}} [C_Y(-\eta_i) J_0(k\eta_*) - C_J(-\eta_i) Y_0(k\eta_*)], \quad (3.58a)$$

$$T^L(k)_{12} = \frac{1}{D(-\eta_i)} \sqrt{-\eta_i \eta_*} [J_0(-k\eta_i) Y_0(k\eta_*) - Y_0(-k\eta_i) J_0(k\eta_*)], \quad (3.58b)$$

$$T^L(k)_{21} = \frac{1}{D(-\eta_i)} \frac{1}{\sqrt{-\eta_i \eta_*}} [C_Y(-\eta_i) C_J(\eta_*) - C_J(-\eta_i) C_Y(\eta_*)], \quad (3.58c)$$

$$T^L(k)_{22} = \frac{1}{D(-\eta_i)} \sqrt{\frac{-\eta_i}{\eta_*}} [J_0(-k\eta_i) C_Y(\eta_*) - Y_0(-k\eta_i) C_J(\eta_*)]. \quad (3.58d)$$

Finally according to Equation (3.11), the overall transfer functions of the quantum bounce epoch can be obtained by combining Equations (3.50), (3.53), and (3.58):

$$\mathbf{T}^B(k) \equiv \mathbf{T}_k^B(\eta_i, \eta_e) = \mathbf{T}^R(k) \mathbf{T}^M(k) \mathbf{T}^L(k). \quad (3.59)$$

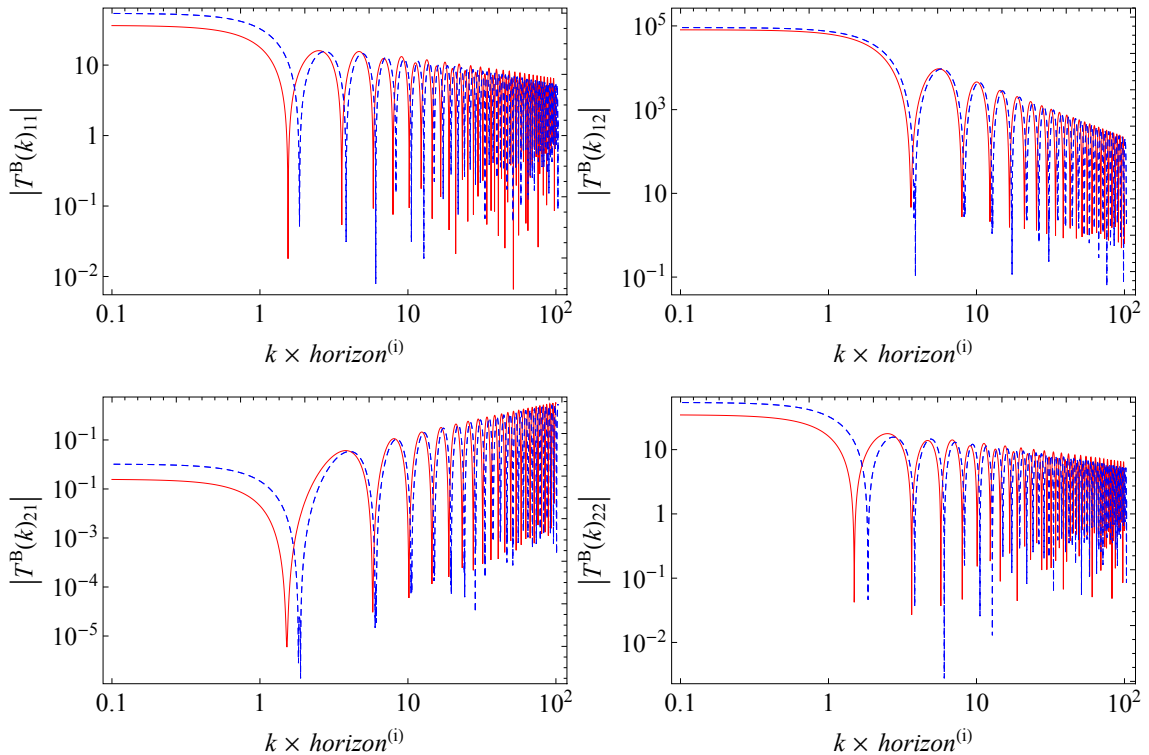


Figure 3.3: The numerical (blue dashed) and analytical (red solid) results for the transfer functions of GWs in the quantum bounce epoch with chaotic potential. We have applied the field-free approximation for  $m_{\text{eff}}$ .

Figure 3.3 presents the results of  $\mathbf{T}^B(k)$ . The “*horizon*<sup>(i)</sup>” in the horizontal axis is the horizon size of causal contact at the beginning of inflation. As expected, the field-free approximation works well at large  $k$  (small scales). To take the advantage of this fact, we can consider only the cosmological models where the *horizon*<sup>(i)</sup> is larger than the horizon today so that all the observable GWs today will have wavelengths much smaller than the horizon size at early times and thus eligible for taking the large- $k$  limit. In such cases, we not only avoid the inaccuracy shown in Figure 3.3 but also get better physical insight for the evolution of GWs.

The Bessel functions of order zero and their derivatives under the large- $k$  limit are [70]

$$\lim_{k \rightarrow \infty} J_0(k\eta) = \lim_{k \rightarrow \infty} \frac{d}{kd\eta} Y_0(k\eta) = \sqrt{\frac{2}{\pi k\eta}} \cos\left(k\eta - \frac{\pi}{4}\right), \quad (3.60)$$

$$\lim_{k \rightarrow \infty} Y_0(k\eta) = \lim_{k \rightarrow \infty} \frac{-d}{kd\eta} J_0(k\eta) = \sqrt{\frac{2}{\pi k\eta}} \sin\left(k\eta - \frac{\pi}{4}\right). \quad (3.61)$$

Therefore the transfer functions in the right and left stages under the large- $k$  limit are

$$\lim_{k \rightarrow \infty} T^R(k) = \begin{bmatrix} \cos(k\Delta\eta_R) & \frac{1}{k} \sin(k\Delta\eta_R) \\ -k \sin(k\Delta\eta_R) & \cos(k\Delta\eta_R) \end{bmatrix}, \quad (3.62)$$

$$\lim_{k \rightarrow \infty} T^L(k) = \begin{bmatrix} \cos(k\Delta\eta_L) & -\frac{1}{k} \sin(k\Delta\eta_L) \\ k \sin(k\Delta\eta_L) & \cos(k\Delta\eta_L) \end{bmatrix}, \quad (3.63)$$

where  $\Delta\eta_R = \eta_b - \eta_*$  and  $\Delta\eta_L = -\eta_* - \eta_i$ .

One interesting feature in this result is that the forms of the transfer functions in the left and right stages have a time reversal symmetry. It means that the field-free approximation leads to a time-symmetric quantum bounce effect. This is actually not surprising because according to Section 2.3 the cosmic background should be time-symmetric with respect to the quantum bounce if there is no scalar field.

Under the large- $k$  limit, GWs behave just like plane waves during the entire quantum bounce epoch because the effective mass is negligible. In such case the transfer functions



should possess the simple form for plane waves:

$$\lim_{k \rightarrow \infty} T^B(k) = \begin{bmatrix} \cos(k\Delta\eta_B) & \frac{1}{k} \sin(k\Delta\eta_B) \\ -k \sin(k\Delta\eta_B) & \cos(k\Delta\eta_B) \end{bmatrix}, \quad (3.64)$$

where  $\Delta\eta_B = \eta_b - \eta_i = \Delta\eta_L + \Delta\eta_M + \Delta\eta_R$ . Indeed this is exactly the same as the result that we obtain from our Equation (3.50) with Equations (3.50), (3.62) and (3.63) under the large- $k$  limit ( $k \rightarrow \infty$ ).

## 3.5 Critical Breakthroughs

### 3.5.1 Consistency with Bogoliubov transformation

We first lay out the framework of the Bogoliubov transformation in literature [30] and then link it to our new approach of transfer functions for cross checking. In their approximation for the effective mass, there are three evolutionary stages and hence we need three transition matrices for transforming the creation and annihilation operators. In our notations, they are

$$\mathbf{M}_k^V(\eta) = \begin{bmatrix} \frac{1}{\sqrt{2k}} e^{-ik\eta} & \frac{1}{\sqrt{2k}} e^{ik\eta} \\ \frac{-ik}{\sqrt{2k}} e^{-ik\eta} & \frac{ik}{\sqrt{2k}} e^{ik\eta} \end{bmatrix}, \quad (3.65)$$

$$\mathbf{M}_k^B(\eta) = \begin{bmatrix} \frac{1}{\sqrt{2k_*}} e^{-ik_*\eta} & \frac{1}{\sqrt{2k_*}} e^{ik_*\eta} \\ \frac{-ik_*}{\sqrt{2k_*}} e^{-ik_*\eta} & \frac{ik_*}{\sqrt{2k_*}} e^{ik_*\eta} \end{bmatrix}, \quad (3.66)$$

$$\mathbf{M}_k^I(\eta) = \begin{bmatrix} g_k(\eta) & g_k^*(\eta) \\ \frac{d}{d\eta}g_k(\eta) & \frac{d}{d\eta}g_k^*(\eta) \end{bmatrix}, \quad (3.67)$$

where the mode function  $g_k(\eta)$  is

$$g_k(\eta) = -\sqrt{\frac{-\pi\eta_{-e}}{4}} H_{3/2}^{(1)}(k\eta_{-e}), \quad (3.68)$$

which satisfies Equation (3.19) with

$$\hat{u}_k^I(\eta) = g_k(\eta)\hat{b}_k + g_k^*(\eta)\hat{b}_{-k}^\dagger. \quad (3.69)$$



Here  $H^{(1)}$  is the Hankel function of the first kind,  $\eta_{-e} = \eta - \eta_e$ , the superscripts “V” and “B” stand for the Minkowski vacuum and the quantum bounce respectively. The corresponding mode function  $f_k$  satisfying the plane wave equation is given by [30]

$$\hat{u}_k^V(\eta) = f_k(\eta)\hat{a}_k + f_k^*(\eta)\hat{a}_{-k}^\dagger. \quad (3.70)$$

Conventionally  $\hat{a}_{-k}^\dagger$  and  $\hat{a}_k$  are the creation and annihilation operators for the Minkowski vacuum. Similarly  $\hat{b}_{-k}^\dagger$  and  $\hat{b}_k$  are the creation and annihilation operators for inflation. The mode functions  $f_k$  and  $g_k$  must satisfy the Wronskian condition [30]

$$W(f_k, f_k^*) = W(g_k, g_k^*) = i. \quad (3.71)$$

The Bogoliubov transformation is therefore

$$\begin{bmatrix} \hat{b}_k \\ \hat{b}_{-k}^\dagger \end{bmatrix} = \begin{bmatrix} \alpha_k & \beta_k^* \\ \beta_k & \alpha_k^* \end{bmatrix} \begin{bmatrix} \hat{a}_k \\ \hat{a}_{-k}^\dagger \end{bmatrix}. \quad (3.72)$$

The coefficients  $\alpha_k$  and  $\beta_k$  can then be determined as

$$\begin{bmatrix} \alpha_k \\ \beta_k \end{bmatrix} = \mathbf{M}_k^I(\eta_b)^{-1} \mathbf{M}_k^B(\eta_b) \mathbf{M}_k^B(\eta_i)^{-1} \mathbf{M}_k^V(\eta_i) \begin{bmatrix} 1 \\ 0 \end{bmatrix}. \quad (3.73)$$

Finally, the GW power spectrum can be obtained by

$$P_T(k) = |\alpha_k - \beta_k|^2 P_T^{\text{std}}(k). \quad (3.74)$$

Two interesting features can be revealed here. First, the initial GWs generated by the



quantum fluctuations in the Minkowski vacuum can now be derived as

$$\mathbf{M}_k^V(\eta_i) \begin{bmatrix} 1 \\ 0 \end{bmatrix} = \begin{bmatrix} \frac{1}{\sqrt{2k}} \\ \frac{-ik}{\sqrt{2k}} \end{bmatrix} e^{-ik\eta_i} = \tilde{U}_k^V(\eta_i). \quad (3.75)$$

Secondly, the transfer functions of the quantum bounce epoch with the approximation  $m_{\text{eff}}^2 = k_0^2$  (for  $\eta_i < \eta < \eta_b$ ) [30] are now given as

$$\mathbf{M}_k^B(\eta_b)\mathbf{M}_k^B(\eta_i)^{-1} = \begin{bmatrix} \cos(k_*\Delta\eta_B) & \frac{1}{k_*} \sin(k_*\Delta\eta_B) \\ -k_* \sin(k_*\Delta\eta_B) & \cos(k_*\Delta\eta_B) \end{bmatrix} \equiv T^{B,\text{old}}(k). \quad (3.76)$$

The superscript “old” stands for the results based on the approximation in literature [30]. We shall discuss this in more details in the next subsection.

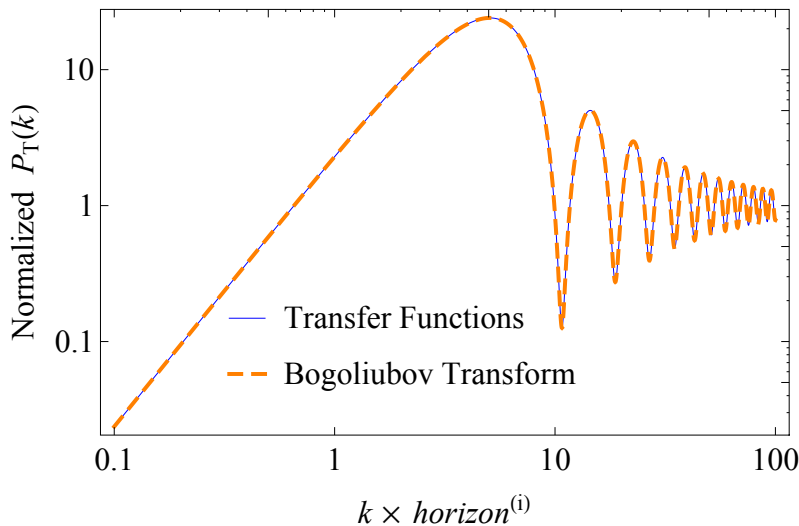


Figure 3.4: The GW power spectra generated by the quantum fluctuations in the Minkowski vacuum before the quantum bounce epoch. The results based on the Bogoliubov transformation (dashed) and on our approach of transfer functions (solid) are totally consistent.

Figure 3.4 compares the GW power spectra based on the Bogoliubov transformation (dashed) and on our approach of transfer functions (solid). It is obvious that they are totally consistent with each other.



### 3.5.2 Solving the IR suppression problem

In Figure 3.4, there is a clear suppression in the normalized GW power spectrum towards long wavelengths (small  $k$ ). This is called the IR suppression first pointed out by Reference [30]. In this subsection, we shall employ our transfer functions to show that the IR suppression is not of a physical origin but a consequence of improper normalization.

The problem comes from the fact that the GW power spectrum in Figure 3.4 is normalized to Equation (3.1), which is valid only for the sub-horizon modes (large  $k$ ). To reveal the super-horizon behavior of the primordial perturbations, we take the small- $k$  limit for Equation (3.21):

$$\lim_{k \rightarrow 0} T^I(k) = \begin{bmatrix} \frac{2}{3}a_e H_{\text{dS}} \Delta\eta_I & -\frac{1}{3}a_e H_{\text{dS}} \Delta\eta_I^2 \\ -\frac{2}{3}a_e^2 H_{\text{dS}}^2 \Delta\eta_I & \frac{1}{3}a_e^2 H_{\text{dS}}^2 \Delta\eta_I^2 \end{bmatrix}. \quad (3.77)$$

Then the GW power spectrum generated by the quantum fluctuations in de Sitter space is

$$\lim_{k \rightarrow 0} P_T^{\text{dS}}(k) = \frac{32\pi H_{\text{dS}}^2 \Delta\eta_I^2}{9k} \propto k^{-1}. \quad (3.78)$$

Equations (3.24) and (3.78) together conclude that  $P_T^{\text{dS}} \propto k^{-3}$  on sub-horizon scales

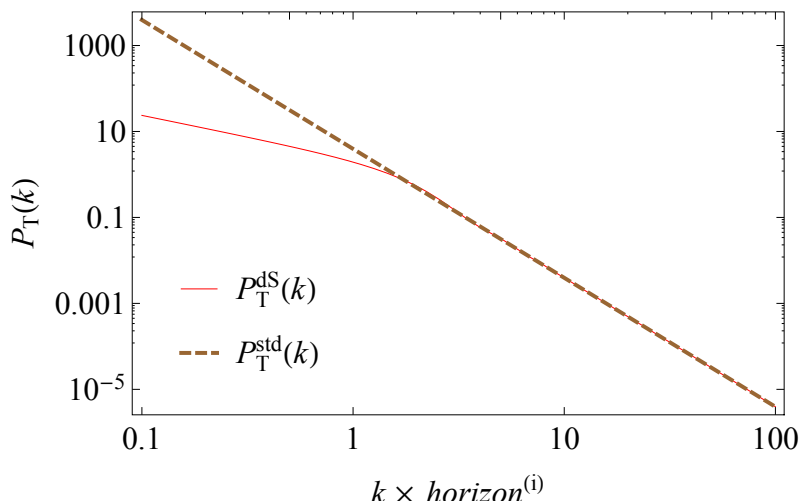


Figure 3.5: The primordial GW power spectra in the standard inflationary cosmology (solid) as compared with the result based on sub-horizon approximation (dashed).

(large  $k$ ) and  $P_T^{\text{dS}} \propto k^{-1}$  on super-horizon scales (small  $k$ ). These behaviors can be seen in the red solid curve in Figure 3.5. The transition of the two behaviors occurs at  $k \times \text{horizon}^{(i)} \sim 1$ . On super-horizon scales, this exact solution deviates significantly from the pure sub-horizon approximation (dashed curve). In other words, taking the  $k^{-3}$  dependence throughout as the primordial form to normalize the entire power spectrum would cause the deficit in the power at small  $k$ , and thus the IR suppression problem.

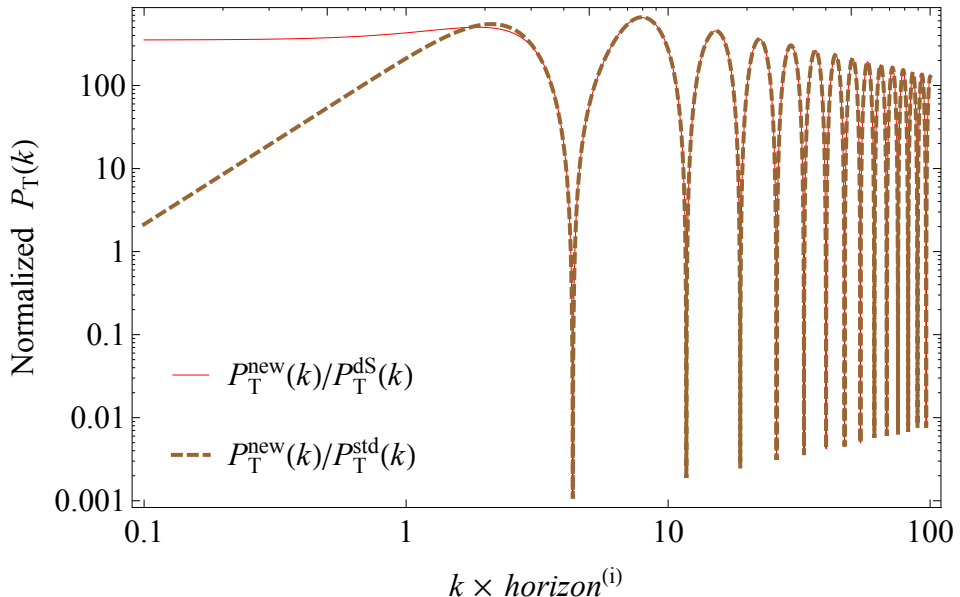
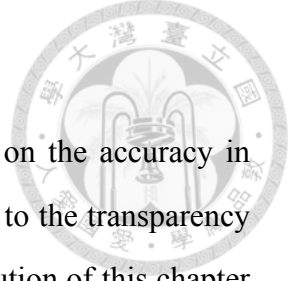


Figure 3.6: The GW power spectrum normalized to its primordial power spectrum in a realistic cosmological model. The brown dashed curve is normalized to  $P_T^{\text{std}}(k) \propto k^{-3}$  (sub-horizon approximation) while the red solid curve is normalized to the correct  $P_T^{\text{dS}}(k)$ .

Figure 3.6 shows the GW power spectrum normalized to its primordial power spectrum in a realistic cosmic background. The brown dashed curve is normalized to  $P_T^{\text{std}}(k) \propto k^{-3}$  (sub-horizon approximation) so the expected IR suppression problem at small  $k$  is clear. On the other hand, the red solid curve is normalized to the correct  $P_T^{\text{dS}}(k)$  based on our formalism of transfer functions, so the IR suppression problem disappears. The correctly normalized GW power spectrum remains constant on the super-horizon scales while oscillating on sub-horizon scales. It means that the GWs originally frozen outside the horizon will start oscillating after the horizon entry.



### 3.5.3 Improvement from field-free approximation

We now demonstrate how much our formalism could improve on the accuracy in evolving the GWs, as compared with the literature [30]. In addition to the transparency of the transfer functions in evolving the GWs, another major contribution of this chapter is the field-free approximation, which provides a better estimate of the effective mass so as to improve the accuracy in evolving the GWs during the quantum bounce epoch.

Reference [30] assumes the effective mass to be a constant  $k_0$  throughout the quantum bounce epoch. This leads to Equation (3.75) in our formalism using transfer functions. In turn we could obtain the GW power spectrum, which is shown in Figure 3.7 as the dash-dotted curve, labeled with “old”. On the other hand, our field-free approximation, which divide and estimate the evolutionary behavior of the effective mass into three stages (see Equation (3.45) and Figure 3.1), leads to the solid curve in Figure 3.7, labeled with “new”. These two results are compared to the numerical solution (dashed curve). It is evident that our field-free approximation leads to a dramatical improvement, while the approximation in Reference [30] results in an overestimation by an order of about two. Although our result may be further improved on super-horizon scales and on the phase accuracy, these

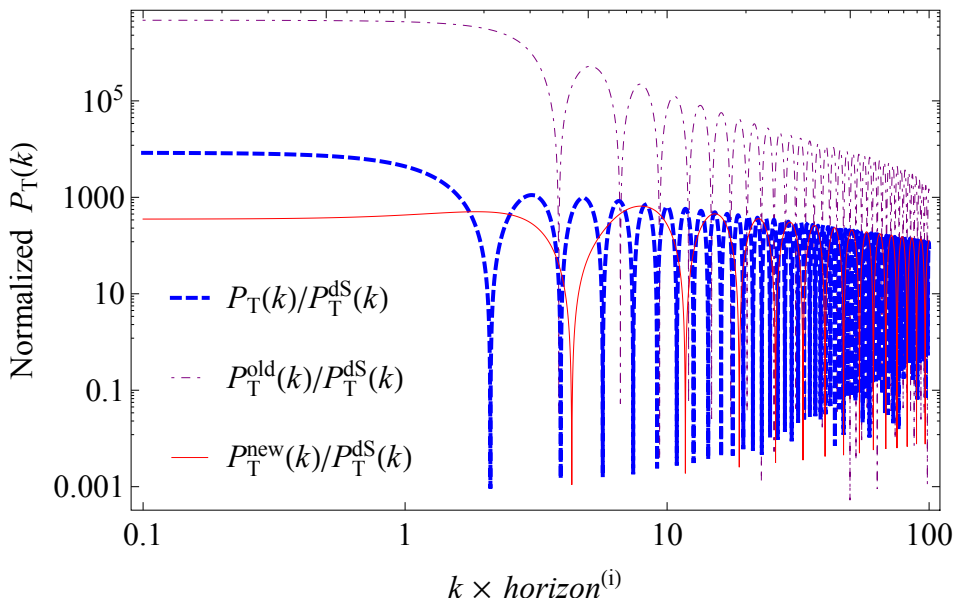
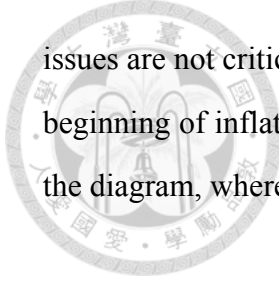


Figure 3.7: The predicted GW power spectra based on the “old” (dash-dotted) and “new” (solid) approaches as compared with the numerical result (dashed), all normalized to the same primordial  $P_T^{\text{ds}}(k)$ .



issues are not critical as the causal horizon today is required to be smaller than that at the beginning of inflation so that the observable scales today should be at the large- $k$  end of the diagram, where our approximation delivers a good result.

## 3.6 Models with a Parent Universe

### 3.6.1 Bouncing scenarios

Previously in Equation (2.33), we have introduced  $\theta_B$  to describe the time-symmetry of cosmic background. However  $\theta_B$  doesn't work well for a potential which is not always positive because the sine term goes to imaginary when the potential goes below zero at the quantum bounce. We therefore directly use, instead of  $\theta_B$ , the value of scalar field at the quantum bounce  $\phi_B$  to quantify the time-symmetry of cosmic background. We now have, for example for chaotic potential, two parameters  $m_\phi$  and  $\phi_B$  that determine the evolution of cosmic background and thus determine the transfer functions.

In this section we consider the models with a parent universe. In other words, there is deflation comes before the quantum bounce epoch instead of the Minkowski vacuum that we considered since Section 3.4. The quantum bounce epoch therefore starts at the end of deflation  $\eta = \eta_e^D$ . There are in terms seven resulted quantities that affect the behaviors of transfer functions:  $\{\chi_2^D, \chi_1^D, \eta_b^D, \eta_*, \eta_b, \chi_2^I, \chi_1^I\}$ , where  $\chi_1^D \equiv -(a_b^D H_{dS}^D)^{-1}$ ,  $\chi_2^I \equiv (a_e H_{dS})^{-1}$ . We can then classify the bouncing scenarios for  $\phi_B > 0$  into three types: highly asymmetric bouncing scenario (HABS), intermediately asymmetric bouncing scenario (IABS), and nearly symmetric bouncing scenario (NSBS), by the following conditions:

$$k_h \chi_2^D > 1 \text{ and } k_h \chi_1^D > 1 \text{ for HABS,}$$

$$k_h \chi_2^D > 1 \text{ and } k_h \chi_1^D < 1 \text{ for IABS,}$$

$$k_h \chi_2^D < 1 \text{ and } k_h \chi_1^D < 1 \text{ for NSBS,}$$

where  $k_h$  is the comoving wavenumber of the Hubble horizon today.

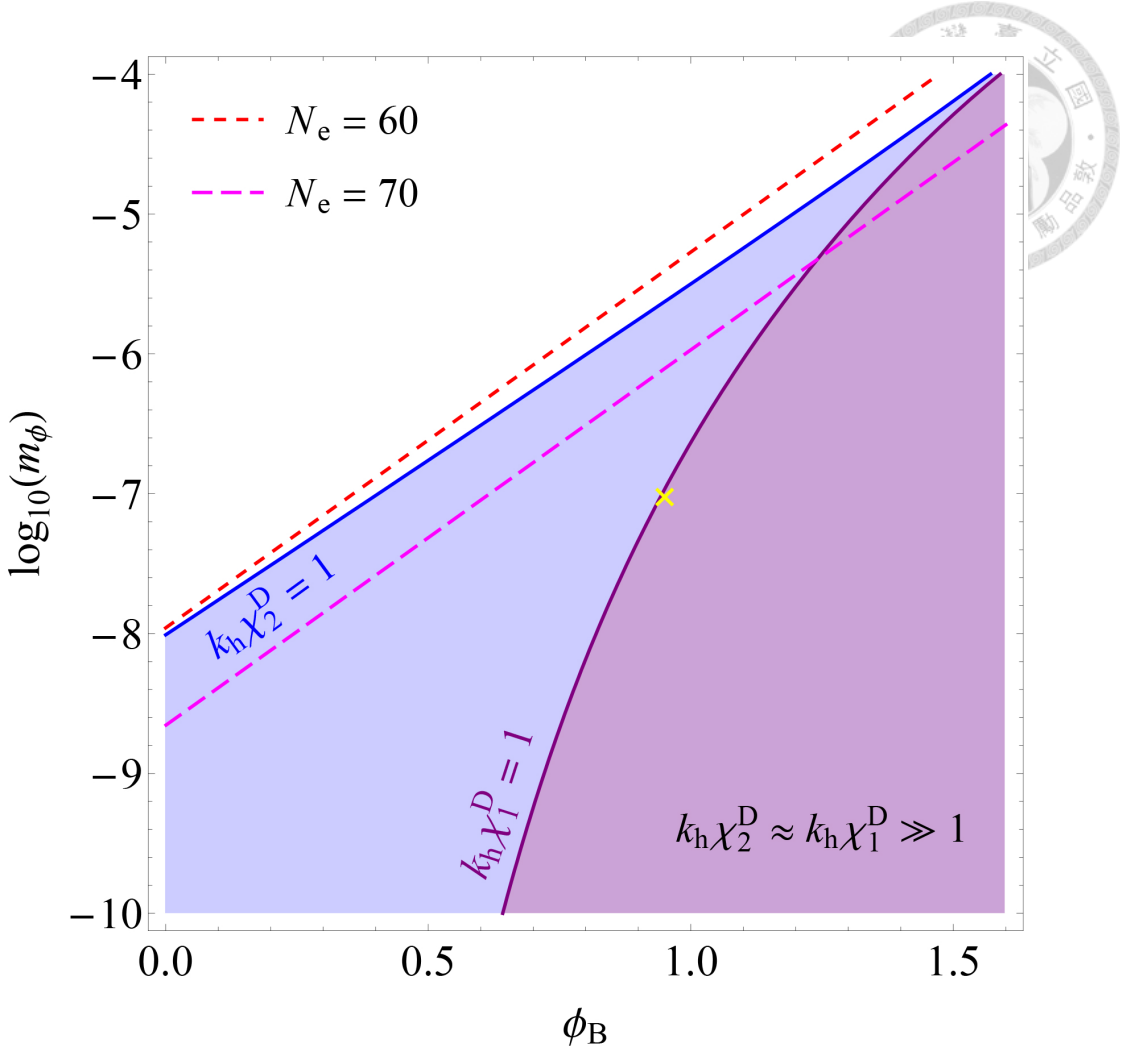


Figure 3.8: The HABS (purple), IABS (blue), and NSBS (blank) regions in the parameter space  $(\phi_B, m_\phi)$ . The two dashed lines are drawn for  $N_e = 60$  and  $70$ , respectively.

Figure 3.8 shows the regions of these three scenarios in the two-dimensional parameter space  $(\phi_B, m_\phi)$  where the solid curves underline the boundaries. It is clear that most of the scenarios with number of  $e$ -foldings for inflation  $N_e$  greater than 60 are HABS's and IABS's. In these two scenarios, inflation is strong enough that  $k_h \chi_1^I$  is much greater than one and  $k_h \chi_2^I$  is much smaller than one so that  $T^I(k)$  must follow Equation (3.23). On the other hand, the quantum bounce occurs at a relatively small scale so  $T^B(k)$  satisfies the large- $k$  limit and thus follows Equation (3.64). The evolutions of pre-existing GWs are therefore simply determined only by deflation. In the following section, we combine all of these conditions and take corresponding limits on  $T^D(k)$  for both HABS and IABS to study the behaviors of pre-existing GWs.

### 3.6.2 Signals from the parent universe

First of all we consider the HABS. In this kind of cosmic background, deflation is small that GWs propagate like plane waves in this era. The transfer functions for deflationary epoch are therefore reduced to

$$\mathbf{T}^D(k) = \begin{bmatrix} \cos(k\Delta\eta_D) & \frac{1}{k} \sin(k\Delta\eta_D) \\ -k \sin(k\Delta\eta_D) & \cos(k\Delta\eta_D) \end{bmatrix} \quad (3.79)$$

and the resulting matrix of overall transfer functions is

$$\mathbf{T}(k) = \begin{bmatrix} -\frac{a_e H_{dS}}{k} \sin(k\Delta\eta_{all}) & \frac{a_e H_{dS}}{k^2} \cos(k\Delta\eta_{all}) \\ \frac{a_e^2 H_{dS}^2}{k} \sin(k\Delta\eta_{all}) & -\frac{a_e^2 H_{dS}^2}{k^2} \cos(k\Delta\eta_{all}) \end{bmatrix}, \quad (3.80)$$

where  $\Delta\eta_{all} = \Delta\eta_D + \Delta\eta_B + \Delta\eta_I$ . We find that Equation (3.80) takes exactly the same forms as  $\mathbf{T}^I(k)$  but with a different phase. With initial conditions  $\tilde{u}_k^{(i)}$  and its derivative  $-ik\tilde{u}_k^{(i)}$ , the power spectrum is given by

$$P_T^{\text{HABS}}(k) = \frac{16\pi H_{dS}^2}{k^2} |\tilde{u}_k^{(i)}|^2 \propto k^{-2} |\tilde{u}_k^{(i)}|^2. \quad (3.81)$$

This result indicates that, in the HABS, deflation is too weak to generate distinguishable feachers on GWs.

We then head into the IABS where deflation become much stronger such that  $k_h \chi_1^D$  goes far below one. The corresponding transfer functions for deflationary epoch are

$$\mathbf{T}^D(k) = \begin{bmatrix} -\frac{(a_b^D H_{dS}^D)^2}{k^2} \cos(k\Delta\eta_D) & -\frac{a_b^D H_{dS}^D}{k^2} \cos(k\Delta\eta_D) \\ \frac{(a_b^D H_{dS}^D)^2}{k} \sin(k\Delta\eta_D) & \frac{a_b^D H_{dS}^D}{k} \sin(k\Delta\eta_D) \end{bmatrix} \quad (3.82)$$

and the matrix of overall transfer functions is therefore

$$\mathbf{T}(k) = \begin{bmatrix} \frac{(a_b^D H_{dS}^D)^2}{k^2} \frac{a_e H_{dS}}{k} & \frac{a_b^D H_{dS}^D}{k^2} \frac{a_e H_{dS}}{k} \\ -\frac{(a_b^D H_{dS}^D)^2}{k^2} \frac{a_e^2 H_{dS}^2}{k} & -\frac{a_b^D H_{dS}^D}{k^2} \frac{a_e^2 H_{dS}^2}{k} \end{bmatrix} \sin(k\Delta\eta_{all}^*), \quad (3.83)$$

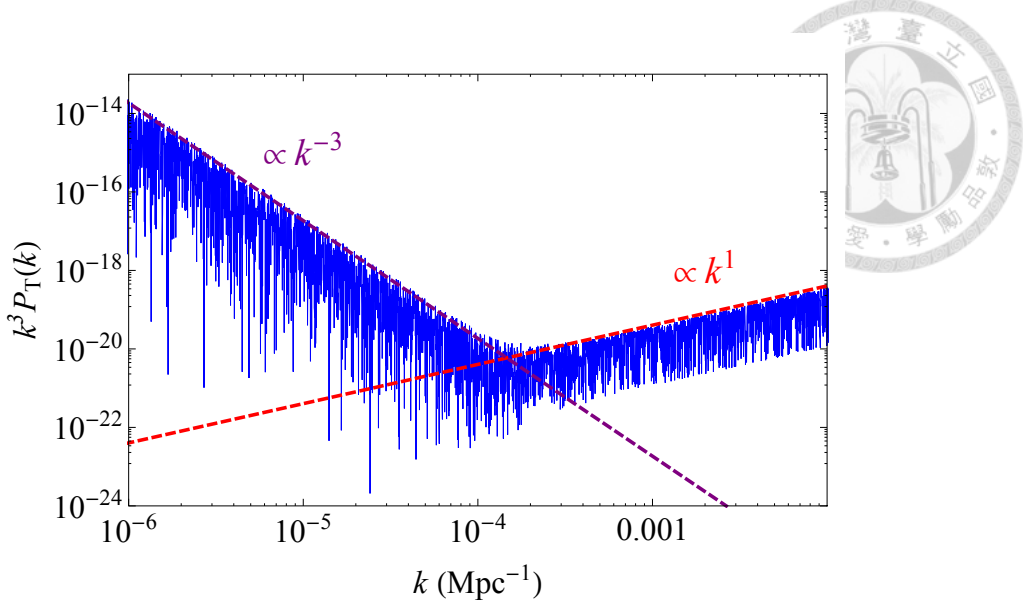


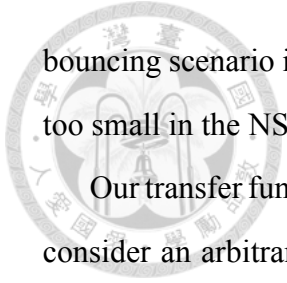
Figure 3.9: The scale-invariant power spectrum of pre-existing GWs generated by a constant  $\tilde{u}_k^{(i)}$  in the parent universe.

where  $\Delta\eta_{\text{all}}^* = \Delta\eta_{\text{D}} + \Delta\eta_{\text{B}} - \Delta\eta_{\text{I}}$ . It's obvious that the evolution of GWs in IABS is significantly different from HABS especially on the  $k$  dependence. By applying the same initial conditions  $\tilde{u}_k^{(i)}$  and its derivative  $-ik\tilde{u}_k^{(i)}$ , we can see that the power spectrum

$$P_{\text{T}}^{\text{IABS}}(k) = \left(\frac{a_{\text{b}}^{\text{D}} H_{\text{dS}}^{\text{D}}}{k}\right)^4 \sin^2(k\Delta\eta_{\text{all}}^*) \frac{16\pi H_{\text{dS}}^2}{k^2} |\tilde{u}_k^{(i)}|^2 \\ \propto k^{-6} \sin^2(k\Delta\eta_{\text{all}}^*) |\tilde{u}_k^{(i)}|^2 \quad (3.84)$$

tilts much more toward large  $k$ . In other words, deflation suppresses small scale waves and enhances large scale waves in the meantime. It means that in our context, we are more possible to observe the pre-existing GWs on large scales rather than small scales.

In order to discuss and compare these two scenarios at once, we consider a case with  $(\phi_{\text{B}}, m_{\phi}) = (0.95, 10^{-7})$  marked by the yellow cross in Figure 3.8, which appears near the boundary of HABS and IABS, and see how  $P_{\text{T}}(k)$  generated by a constant  $\tilde{u}_k^{(i)}$  behaves. The result is shown in Figure 3.9 with  $k_{\text{h}} \approx 0.0002 \text{ Mpc}^{-1}$ . The sub-horizon waves which correspond to the results of  $k_{\text{h}}\chi_1^{\text{D}} > 1$  behave like in HABS, where  $k^3 P_{\text{T}}(k) \propto k$ . In contrast, the super-horizon waves which correspond to the results of  $k_{\text{h}}\chi_1^{\text{D}} < 1$  behave like in IABS, where  $k^3 P_{\text{T}}(k) \propto k^{-3}$ . We conclude that the effects from deflation is invisible if the bouncing scenario is highly asymmetric, and expected on large scale if the



bouncing scenario is intermediately asymmetric. We note that the number of  $e$ -foldings is too small in the NSBS which we do not discuss here in this paper.

Our transfer functions is mathematically and physically transparent that if we generally consider an arbitrary source of pre-existing GWs in the parent universe, say  $\tilde{u}_k^{(i)} \propto k^n$ , the resulted power spectrums is simply computed as  $k^3 P_T(k) \propto k^{2n+1}$  for HABS and  $k^3 P_T(k) \propto k^{2n-3}$  for IABS. This helps us to study other possible kinds of pre-existing GWs such as those originated from well-known astronomical systems. Indeed we have used the transfer functions to obtain the observational features resulting from the GWs generated by stellar binaries in the parent universe in our another work which is going to be published soon.

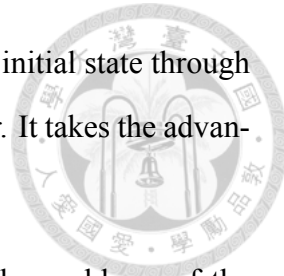
### 3.7 Summary

In this chapter, we proposed a new formalism that employs the transfer functions to evolve the GWs. For the first time in literature this enables us to study the GWs even before the quantum bounce. We offered the analytical forms of the transfer functions for the deflationary, the quantum bounce, and the inflationary epochs. We also provided a complete recipe for obtaining accurate numerical results and utilize it for the discussions and to verify our results.

In particular the transfer functions deliver accurate evolution for the primordial GW power spectrum in the standard inflationary cosmology. We used the transfer-functions formalism to resolve the IR suppression problem. We also shown that our new approach using the transfer functions is equivalent to and produces same results as the Bogoliubov transformations, but with great simplicity and thus much lower cost in calculation. This advance should be beneficial to those studying the GWs in LQC.

In addition to the transfer-function formalism, we proposed the field-free approximation for the effective mass in the quantum bounce epoch, which dramatically improves the accuracy in the predicted GW power spectrum.

We conclude this chapter by summarizing three essential advantages of the transfer function formalism in evolving the GWs and obtaining their power spectrum.



- Simplicity: The transfer functions can bring the GWs from the initial state through various epochs to the final state in a simple but accurate manner. It takes the advantage of the linear algebra.
- Intuitiveness: The transfer functions enable us to deal with the problems of the quantum mechanics in a classical way. We have verified that they are a complete alternative to the Bogoliubov transformations so that we do not need to calculate the Bogoliubov transformations anymore. In addition, the  $k$ -dependence in the GW power spectrum can be transparently revealed and we have take this advantage to resolve the IR suppression problem.
- Generality: The transfer function formalism is general in dealing with any linear problems. In cosmology, most perturbations of our interest are tiny and have evolved mostly in the linear regime. Thus we expect our formalism to be equally useful under other context with linearity.

In the next chapter we will use the transfer functions to evolve realistic initial conditions from the parent universe and see what the imprints they leave on the CMB angular power spectra.





# Chapter 4

## Signatures of Pre-existing Gravitational Waves

*“To be is to be perceived.”*

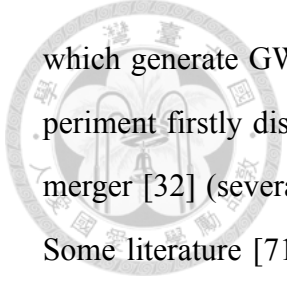
— George Berkeley

### 4.1 Overview

GWs are believed as possible signals being able to travel through the quantum bounce. According to our studies in Chapter 2, there is possibly a parent universe before the quantum bounce under the context of LQC. In Chapter 3, we have further introduced for realistic LQC background the transfer functions which evolve GWs through various cosmic epochs. In this chapter, we expect non-zero GW signals originated from the parent universe. Then we shall use the transfer functions from Chapter 3 to bring them to our present universe and discuss their observability.

The pre-existing GWs might carry characteristic information related to the parent universe for us to probe the age before the quantum bounce. They are expected to be distinguishable to the primordial GWs generated by quantum fluctuations during the early universe.

We suppose in the parent universe that there are astronomically bounded systems



which generate GWs as in our present universe. This is interesting since the LIGO experiment firstly discovered in early 2016 a GW event generated by a binary black hole merger [32] (several more events have also been confirmed in the later years [33–36]). Some literature [71–73] pointed out that there are several kinds of GW background in our universe and are possibly detected in the near future. We first consider, in particular, stellar binary systems as the GW sources in the parent universe in this study.

The primary goal of this chapter, as well of this dissertation, is to find the imprints of the pre-existing GWs on the angular power spectra of CMB, in particular, the B-mode polarization. Consequently, people can probe the parent universe once upon these signatures are observed in the future. As the first attempt, we first to use the current observational data to confine the cosmic background parameters and thus test the LQC models.

We firstly review the GW background in Section 4.2, use the GW background from stellar binary systems as the initial conditions to find the corresponding observational features in Section 4.3, and then compare the results with the current concordance model and observational data in Section 4.4. Finally, we conclude this chapter in Section 4.5.

## 4.2 Pre-existing Gravitational Waves

### 4.2.1 Gravitational-wave background as initial conditions

While studing GWs there are two physical properties, strength (amplitude) and scale (wavelength), which are supposed to be examinable by observations. Since we have not yet actually discover the pre-existing GWs now, the strength of pre-existing GWs is required to be smaller than the upper bound given by the latest observational result otherwise the model must be ruled out. On the other hand, the characteristic features of pre-existing GWs should be located at sub-horizon scale today for being detectable.

The GW function in the transverse-traceless gauge  $\tilde{h}(f, \mathbf{x})$  in frequency domain is related to the GW energy density by [72]

$$\Omega_{\text{gw}}(f) = \frac{2\pi^2}{3H_0^2} f^3 S_h(f) = \frac{8\pi^2}{3H_0^2} f^4 |\tilde{h}(f)|^2. \quad (4.1)$$

The power spectral density is defined by [71, 72]

$$S_h(f) = 4f \langle \tilde{h}^*(f, \mathbf{x}) \tilde{h}(f', \mathbf{x}') \rangle_{(\mathbf{x}, \mathbf{x}')} = 4f |\tilde{h}(f)|^2. \quad (4.2)$$



As considered in Chapter 3, we need the mode functions  $\tilde{u}_k(\eta)$  and their conformal time derivative as the initial conditions. Starting by  $\tilde{h}(f, \mathbf{x})$ , there are several steps to get  $\tilde{u}_k(\eta)$ . The first step is to perform the inverse Fourier transform from frequency to proper time space

$$F_f^{-1}[\tilde{h}(f, \mathbf{x})] \rightarrow h(t, \mathbf{x}).$$

The second step is to change the time variable from proper time to conformal time

$$h(t, \mathbf{x}) \rightarrow h(\eta, \mathbf{x}).$$

The final step is to apply Equations (3.4) and (3.6) to get  $\tilde{u}_k(\eta)$  (or equivalently, to do the Fourier transform)

$$F_{\mathbf{x}}[h(\eta, \mathbf{x})] \rightarrow \tilde{h}_k(\eta)$$

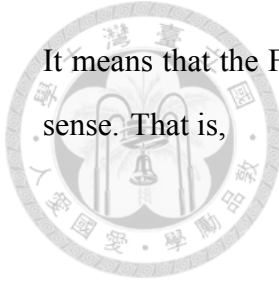
and then to get  $\tilde{u}_k(\eta)$  with an alternative definition

$$\tilde{u}_k(\eta) = \frac{a(\eta) \tilde{h}_k(\eta)}{\sqrt{16\pi}}.$$

However, there seems no way to find  $\tilde{h}(f, \mathbf{x})$  to complete the above procedure since  $\Omega_{gw}$  does not contain any spacial information. Namely, we are impossible to get the initial conditions from  $\Omega_{gw}$  through the above steps.

Fortunately, the GWs propagate with speed of light (null geodesic). The dispersion relation in the classical regime of an evolving universe is

$$\omega^2 = \frac{k^2}{a^2} = \frac{(\mathbf{k} \cdot \mathbf{x})^2}{t^2}. \quad (4.3)$$



It means that the Fourier transform with respect to time and space are equivalent in this sense. That is,

$$F_f F_{\mathbf{x}}^{-1} = F_{\mathbf{x}} F_f^{-1} = I \quad (4.4)$$

in the first and final steps.

Thanking to the fantastic property Equation (4.4), we can obtain  $\tilde{u}_k(\eta)$  by simply changing the variable from  $f$  to  $\mathbf{k}$  through the dispersion relation shown by Equation (4.3). The parent universe is also assumed to be homogeneous and isotropic on large scale to satisfy the cosmological principle in the following discussions. The wavenumber  $\mathbf{k}$  is aligned to the radial direction and hence can be simplified to be its module  $k$ .

Combining Equations (4.1), (4.2), and (4.3) with  $a = a_{\text{init}} \equiv a(\eta_{\text{init}})$ , and using the alternative definition of  $\tilde{u}_k$  mentioned in the final step, the initial condition (which is supposed to be identical to today's  $\tilde{u}_k$ ) can be written as

$$\tilde{u}_k = \frac{a_0 H_0}{2} \frac{a_{\text{init}}^2}{k^2} \sqrt{\frac{3\pi}{2} \Omega_{\text{gw}}} \quad (4.5)$$

The derivatives are also known as below

$$\frac{d\tilde{u}_k}{d\eta}(\eta_{\text{init}}) = -ik\tilde{u}_k(\eta_{\text{init}}) \quad (4.6)$$

by assuming that the GWs in the parent universe behave like plane waves, where  $\eta_{\text{init}}$  is the conformal time when we put the initial conditions.

We suppose that the parent universe appears similarly to our present universe. There should be gravitationally bound systems such as stars, galaxies, and clusters, which might generate GWs like those in our present universe. The key is that we are able to consider them as the initial conditions of  $\tilde{U}_k$  and put them at any time in the parent universe. The reason is that  $\tilde{U}_k$  is a quantity in the comoving coordinates. It will never change even the universe is contracting or expanding in the non-inflating eras including pre-deflationary and post-inflationary epochs.

### 4.2.2 Astronomical sources of gravitational waves



We start with the knowledges about our present universe. The known sources of GWs according to GR are inspiralling or coalescing stellar binaries [74–79], rotating neutron stars [80, 81], core-collapse supernovae [82], and so on [83–85]. If the parent universe contains these systems, they are also possible sources of pre-existing GWs.

We will only take the GWs generated by stellar binary systems into consideration in this work. The reason is that stellar binary is the most well-known system which is expected to emit GWs in our universe. There are numbers of literature discussing the GW background from stellar binary systems. The studied stellar binary systems are white dwarfs binary (WD-WD), neutron star-white dwarf binary (NS-WD), neutron stars binary (NS-NS), black hole-neutron star binary (BH-NS), black holes binary (BH-BH), and super-massive black holes binary (MBHB) [86]. We note that the massed of black holes are less than  $20M_{\odot}$  in BH-NS and BH-BH, and larger than  $100M_{\odot}$  in MBHB.

The energy density spectra of the GW background  $\Omega_{\text{gw}}$  generated by stellar binary systems are theoretically predicted by Reference [86] and updated by Reference [5] with the latest models and cosmological parameters. There are uncertainties on  $\Omega_{\text{gw}}$ . They are originated from uncertainties on the merger rate of stellar binary systems [87–90] and masses of white dwarfs [91], neutron stars [92], and black holes [93–95]. The upper panel of Figure 4.1 presents  $\Omega_{\text{gw}}$  from all kinds of stellar binary systems with respect to the physical frequency [5]. The solid curves present the results from the most likely values of the stellar masses and coalescence rates, and the shaded bands show the uncertainties of  $\Omega_{\text{gw}}$ . The GWs from stellar binary systems are assumed to be tested by the future observations such as advanced LIGO and Virgo [96–98], eLISA [99], and so on.

The lower panel of Figure 4.1 presents the initial conditions of  $\tilde{u}_k$  corresponding to each component with the scale factor today  $a_0$  chosen to be unity.

Another fact of relevance is that the contractive and expansive history of the universe must rescales the wavelength  $\lambda$  of the pre-existing GWs. We thus define the “rescaling

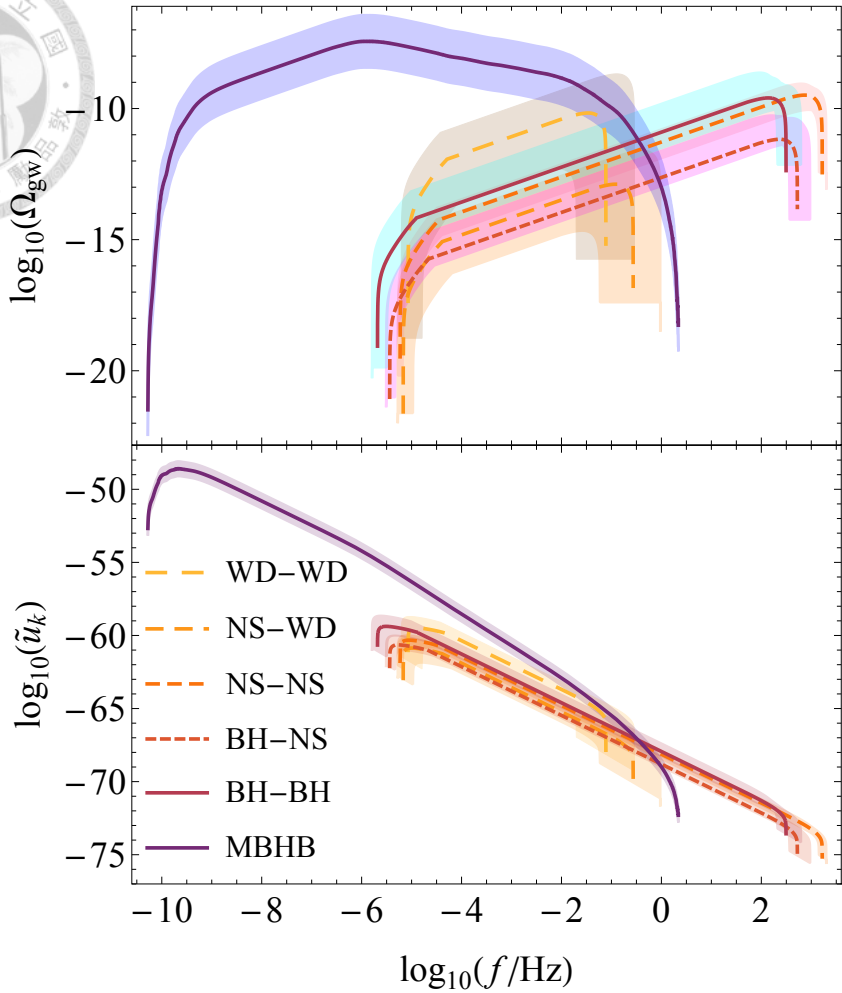


Figure 4.1: The energy density spectra of GWs (upper panel) [5] and the initial  $\tilde{u}_k$  (lower panel) generated by stellar binary systems with respect to the physical frequency. The solid curves and the shaded bands present the most likely values and the uncertainties, respectively. The scale factor today  $a_0$  has been chosen to be unity.

factor” as

$$W = \frac{\lambda_0}{\lambda_{\text{init}}} = \frac{a_0}{a_{\text{init}}}, \quad (4.7)$$

where the second equality comes naturally from the cosmic redshift. It is a free parameter in our investigation, consequently, we can choose  $W > 1$  to stretch the wavelength of pre-existing GWs.

Theoretically, according to Figure 4.1,  $f_{\text{max}} \approx 1000 \text{ Hz}$  is the maximum GW frequency that any stellar binary systems can generate. Therefore for such GWs in the parent

universe to still lie within our horizon scale today we need to require

$$W \leq W_h = \frac{f_{\max}}{f_h} \approx 3.2 \times 10^{20}, \quad (4.8)$$



where the subscript “h” denotes the horizon scale today. The subscript “sb” denotes “stellar binary” in the above equation.

## 4.3 Observational Features

### 4.3.1 Power spectrum of gravitational waves

As studied in Chapter 3, the cosmic background dynamics determines the transfer functions. Simply speaking, the transfer functions depend on the cosmic background parameters:  $\phi_B$  and the inflaton mass  $m_\phi$  (for chaotic potential) or  $m_H$  (for  $R^2$  potential). Thus, the pre-existing GWs that we can observe also depend on the cosmic background parameters when the rescaling factor  $W$  is fixed.

For conveniently demonstrating our results, we here define a new quantity

$$\alpha_\phi \equiv \frac{\phi_B}{\phi_{\text{crit}}}. \quad (4.9)$$

We note that this  $\alpha_\phi$  is not a good physical parameter because  $\phi_{\text{crit}}$  depends on inflationary models and thus is not uniquely defined.

The solid curve in Figure 4.2 demonstrates the total power spectrum of pre-existing GWs generated by stellar binary systems in the cosmic background with the chaotic potential. The cosmic background parameters are chosen to be  $\alpha_\phi = 1.0$  and  $m_\phi = 10^{-5}$ , and the rescaling factor is fixed at  $10^{13}$ . It has been normalized to the primordial power spectrum with the tensor-to-scalar ratio  $r = 1$  and the tensor spectral index  $n_T = 0$ . For comparison, the primordial power spectrum with  $r = 0.07$ , which is the observational upper bound given by BICEP2/Keck experiment [42], is presented by the dashed horizontal line in the figure as well. We have known that there are several components of stellar binary systems. What we observed here is, therefore, the summation of all components.

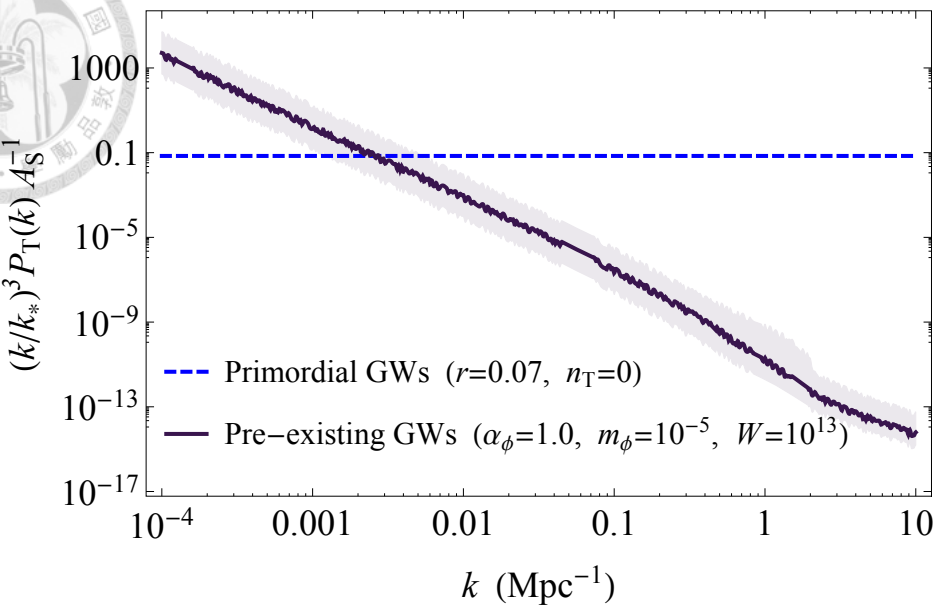
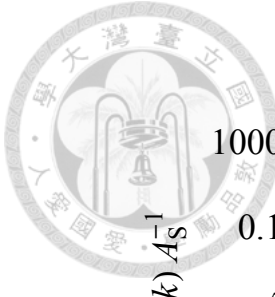


Figure 4.2: The power spectrum as evolved from the pre-existing GWs (solid) with the uncertainties from modelling the pre-existing GWs (shaded).

The solid curve corresponds to the final state evolving from the initial conditions with the most-likely values of stellar mass and coalescence rate. The shaded area around the solid curve illustrates the overall uncertainties mentioned in the previous section.

As shown in the figure, it is evident to see that the pre-existing GWs suppress more quickly compared to the primordial GWs while  $k$  increasing. It means that they are significant on large scale. In fact, this phenomenon can be roughly explained by an analytical approach. According to the literature [5, 86], we know that  $\tilde{u}_k$  generated by the stellar binary systems is approximately proportional to  $k^{-5/3}$ . The corresponding  $P_T(k)$  calculated by the transfer functions studied in Chapter 3 is, therefore, roughly proportional to  $k^{-19/3}$ , which is much steeper than the primordial power spectrum ( $\propto k^{-3}$ ).

We can see there appear fluctuations on the solid curve. They are caused by the oscillations of the transfer functions. It is because that the Hubble horizon today, in this cosmic background, corresponds to an extremely small scale in the comoving space (i.e. the HABS, see Section 3.6 in detail) where the transfer functions oscillate so fast. This effect is hard to be detected since the resolutions of instruments are limited. Also, these fluctuations will be smeared out after  $P_T(k)$  is integrated to an angular power spectrum as what we will do in the next subsection.

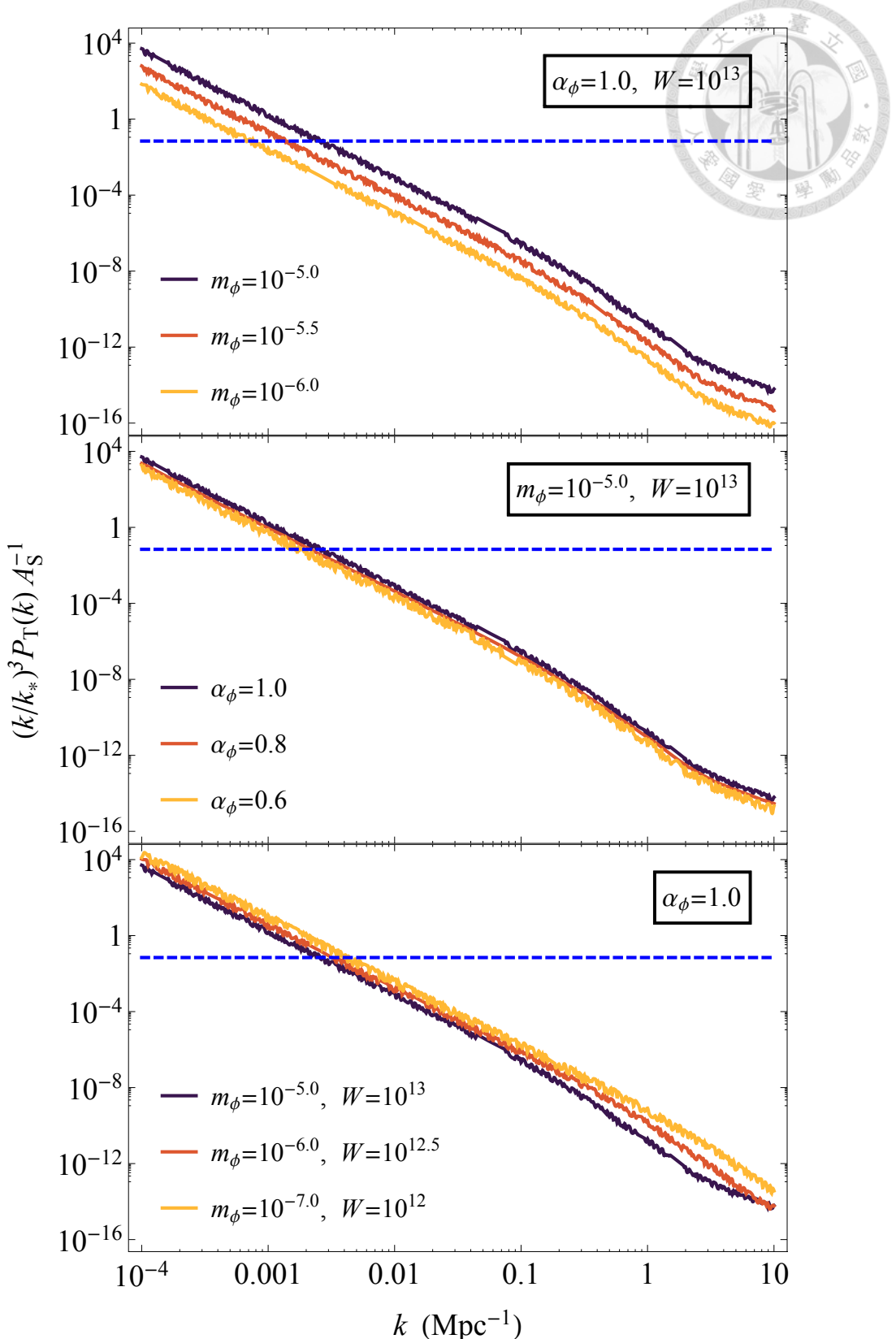


Figure 4.3: Comparisons of the power spectra resulted from the pre-existing GWs with different background parameters.

Figure 4.3 illustrates the parameter dependences of the pre-existing power spectrum in the chaotic background, too. In the upper two panels, we fix one of two cosmic background parameters and variate another one to see how  $P_T(k)$  changes. The rescaling factor  $W$  in this two cases is again fixed at  $10^{13}$ . Here we choose proper parameter configurations such that the pre-existing GWs are comparable to the primordial power spectrum with  $r = 0.07$  shown by the blue dashed lines as in Figure 4.2.

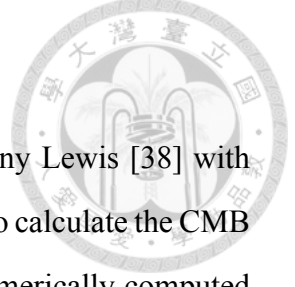
The top panel presents the power spectra by varying  $m_\phi$  from  $10^{-6}$  to  $10^{-5}$  with  $\alpha_\phi$  fixed at 1.0. We can obviously see that  $P_T(k)$  becomes smaller when  $m_\phi$  increases. That is because the size of the universe grows more through deflation to inflation in a more time-asymmetric cosmic background. Thus, the GWs are diluted more. The middle panel presents the power spectra by varying  $\alpha_\phi$  from 0.6 to 1.0 with  $m_\phi$  fixed at  $10^{-5}$ . As shown in the plots, there is no significant difference between the power spectra. It seems quite surprising to get this result since we have known that  $\phi_B$  determines the time symmetry of cosmic background according to Section 2.3. However, when  $\phi_B$  becomes positive, the magnification of GWs will be enlarged during the quantum bounce epoch.

To explain this, we note that in the HABS  $P_T(k)$  is proportional to  $H_{\text{dS}}^2$ , which takes the following form for a chaotic potential under the PSRA:

$$H_{\text{dS}}^2 = \frac{4\pi}{3} m_\phi^2 \phi^2. \quad (4.10)$$

Therefore, a positive  $\alpha_\phi$ , equivalently a positive  $\phi_B$  by Equation (4.9) when  $m_\phi$  is fixed, raises the value of  $\phi$  during inflation and thus enlarges  $H_{\text{dS}}^2$  and  $P_T(k)$ . This enlargement is considerable to the increment of dilution caused by inflation. That is why we see as the result of this panel.

In the upper two panels, the power spectrum  $P_T(k)$  can only change by amplitude (i.e. vertically). As considered in Subsection 4.2.2, the only way to change the scale of  $P_T(k)$  is to choose different values of  $W$ . That is what the bottom panel presents. In this plot,  $\alpha_\phi$  is fixed at 1.0 and  $m_\phi$  is chosen to be several values for remaining  $P_T(k)$  in the same order when varying  $W$ . We can see that for the cases with smaller  $W$ ,  $P_T(k)$  moves horizontally to larger  $k$  as expected.



### 4.3.2 CMB B-mode angular power spectrum

In this subsection, we run the CAMB code developed by Anthony Lewis [38] with applying the latest cosmological parameters provided by Planck [40] to calculate the CMB B-mode angular power spectra of pre-existing GWs. We use our numerically computed  $P_T(k)$  presented in the last subsection as the input of CAMB so that we can get the B-mode angular power spectra  $C_l^{BB}$  predicted by the models. The corresponding  $C_l^{BB}$  induced by  $P_T(k)$  shown in Figure 4.2 is presented in Figure 4.4. The solid curve illustrates the most-likely spectrum and the purple shaded band refers to its uncertainty.

As what we have presented in Figure 4.2, again, the pre-existing GWs are significantly strong on the large scale (i.e.  $l < 30$ ). Otherwise, the CMB B-mode should be dominated by the signals from other known sources (e.g. lensing induced B-mode). The primordial B-mode with  $r = 0.07$  and lensing induced B-mode are also provided in the figure as references.

The signals of pre-existing GWs on such large scale are expected to be detectable only by space-based instruments such as Planck satellite. It is hard for ground-based instruments to measure because of insufficient sky coverage unless they spend a long time to

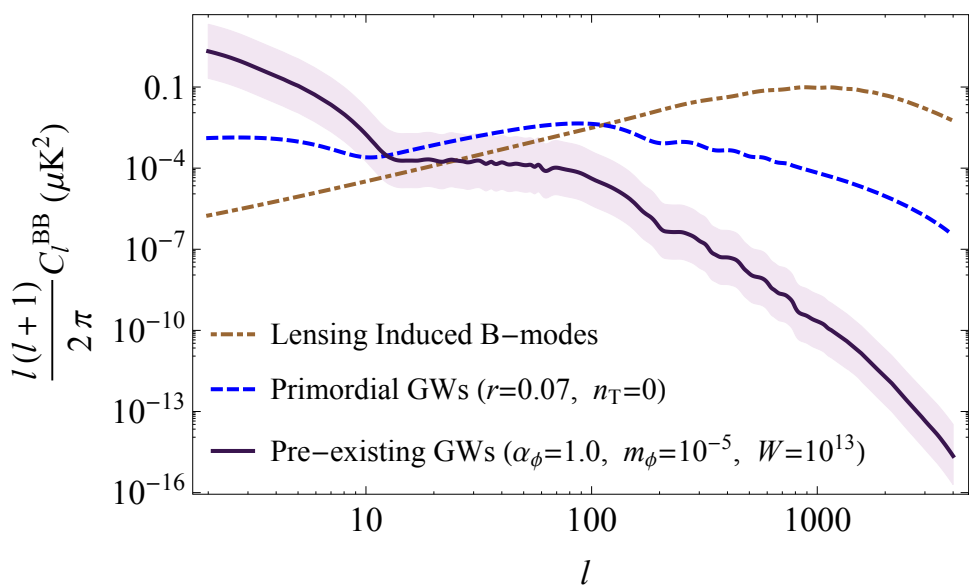


Figure 4.4: The B-mode angular power spectrum resulted from the pre-existing GWs (solid), as compared with the primordial (dashed) and the lensing power (dash-dotted).

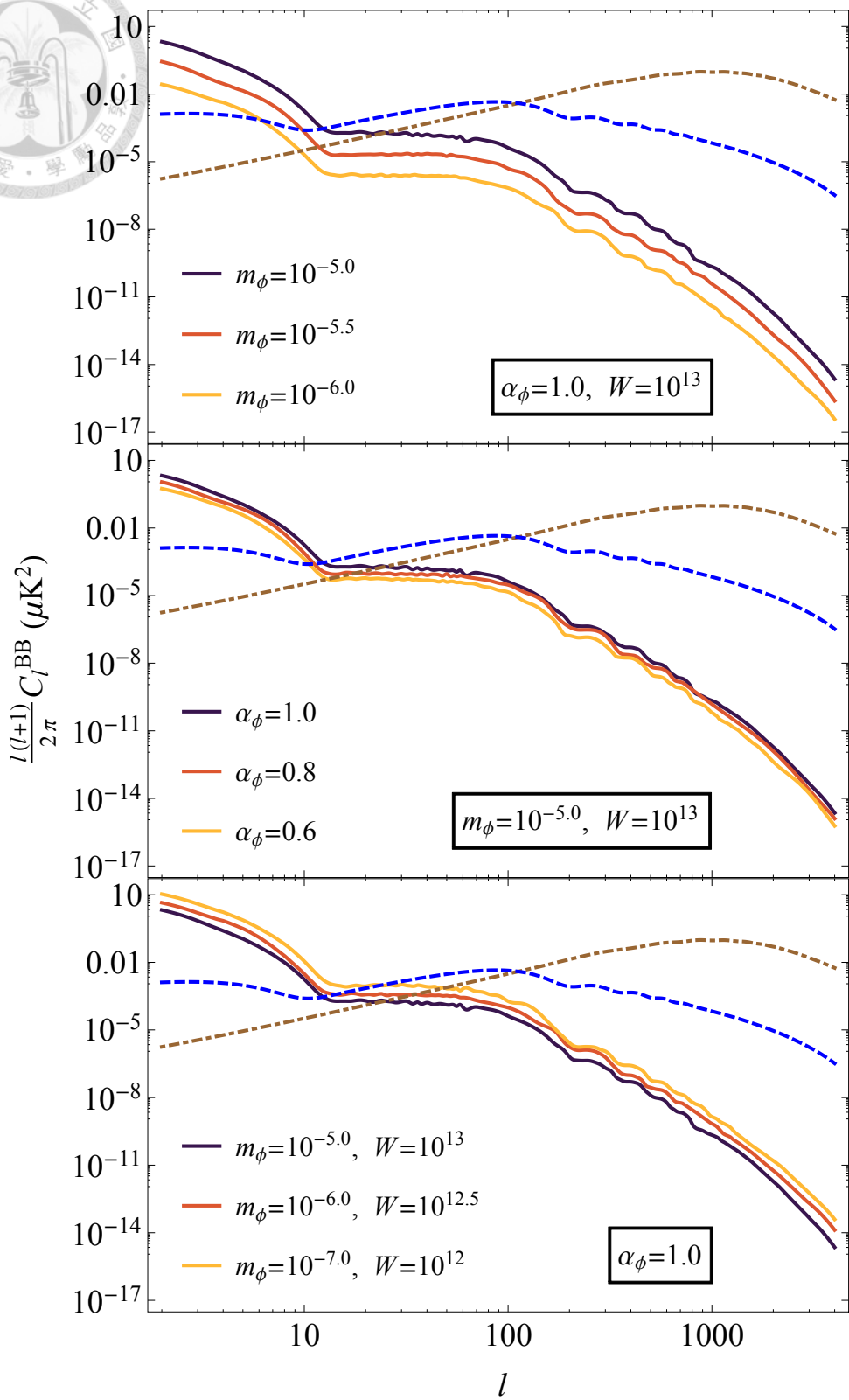


Figure 4.5: Comparisons of the B-mode angular power spectra resulted from the pre-existing GWs with different background parameters.

accumulate data from enough area of patches of sky. There is still a statistical problem for both space-based and ground-based experiments, that is, considerable sample variance.

Here we especially note that the pre-existing GWs are much larger than the primordial GWs. If the pre-existing GWs are observed and confirmed, the tensor-to-scalar ratio of the primordial GWs must be effectively zero under this theoretical framework. Meaning, there is no way for the purple solid and blue dashed curves being valid simultaneously. As a result, the medium scale ( $30 < l < 200$ ) might become a significant window to justify whether there are GWs from the parent universe if there are actual detections in this range. This detection window, indeed, is more favored by the ground-based experiments.

Figure 4.5 illustrates the parameter dependences of pre-existing  $C_l^{\text{BB}}$  induced by  $P_T(k)$  shown in Figure 4.3. All panels of Figure 4.5 directly correspond to Figure 4.3. As the conclusion of Figure 4.3, the B-mode becomes smaller when  $m_\phi$  increases. There is no significant different when varying  $\alpha_s$ . The reasons are just as stated before when we are discussing  $P_T(k)$ .

We have seen that there appear different features of  $P_T(k)$  on small scale in the bottom panel of Figure 4.3, however, it is difficult to see any distinction between the B-mode angular power spectra with various the rescaling factor. The meaning is that there is a strong degeneracy between  $m_\phi$  and the rescaling factor. In other words, we might have to constrain  $m_\phi$  through alternative ways so that we can restrict the rescaling factor by our method. Nonetheless, since the amplitude of pre-existing  $C_l^{\text{BB}}$  is very sensitive to the rescaling factor, we are still able to fix the value of the rescaling factor as usual and construct restrictions of the cosmic background parameters.

### 4.3.3 Restriction of chaotic background parameters

We here compare our theoretical works to the observational realities in the parameter space. The CMB B-mode angular power spectra predicted by our computations are required to be lower than the upper bound set by BICEP2/Keck experiment within the multipole range  $20 < l < 330$  [42]. That might put some restrictions on the cosmic background parameters when the rescaling factor is fixed.

First of all, we investigate the pre-existing GWs in the chaotic background. Figure 4.6 and Figure 4.7 present the maximum of  $C_l^{\text{BB}}/C_l^{\text{BB, std}}$  with respect to  $\alpha_\phi$  and the inflaton mass  $m_\phi$ , respectively. In Figure 4.6, the solid curves with different colors correspond to different values of  $m_\phi$  from  $10^{-10}$  to  $10^{-3}$ . Moreover, in Figure 4.7, the solid curves with different colors correspond to different values of  $\alpha_\phi$  from 0 to 1. The rescaling factors in these two plots are both fixed at  $10^{13}$ . The observational upper bound provided by BICEP2/Keck experiment is presented by the red dashed horizontal line.

We have mentioned that there are uncertainties from the initial conditions on  $C_l^{\text{BB}}$ . As a result, there are uncertainties on the maximum of  $C_l^{\text{BB}}/C_l^{\text{BB, std}}$  as well. In Figures 4.6 and 4.7, the solid curves illustrate the most-likely values and the corresponding shaded bands present their uncertainties.

The cosmic background with parameter configurations that correspond to those points greater than zero have already been ruled out observationally as what we have just mentioned above. For example, a universe with  $m_\phi = 10^{-8}$  (the gray curve in Figure 4.6) should be excluded if  $\alpha_\phi \lesssim 0.2$ . Furthermore, there's no way for a cosmic background with  $\alpha_\phi < 0.1$  to pass the observational examination for all  $m_\phi$  shown in this figure.

On the other hand, we may put some restrictions to  $m_\phi$  according to the figures. The pre-existing GWs become much larger when  $\alpha_\phi$  is smaller as shown in Figure 4.6. In other words, the cosmic background with larger  $m_\phi$  are more disfavored by observations. We can reach the same conclusion by looking at Figure 4.7 as well. We can further see in Figure 4.7 that all time-symmetric cosmic background have been ruled out observationally with strong confidence.

We also present the regions of observational acceptance in the two-dimensional parameter space  $\{(\alpha_\phi, m_\phi) \in \mathbb{R}^2\}$  in Figure 4.8. The rescaling factor  $W$  is fixed at  $10^{13}$ . The solid curves present the most-likely upper bound which refers to the zero level on the color bar. This figure provides the permitted and prohibited regions separated by the solid curves. It presents a visualized constraint on the cosmic background parameters. According to the figure, we conclude that the cosmic background with smaller  $\alpha_\phi$  and larger  $m_\phi$  are more disfavored in which the GWs might be dramatically enlarged during deflation

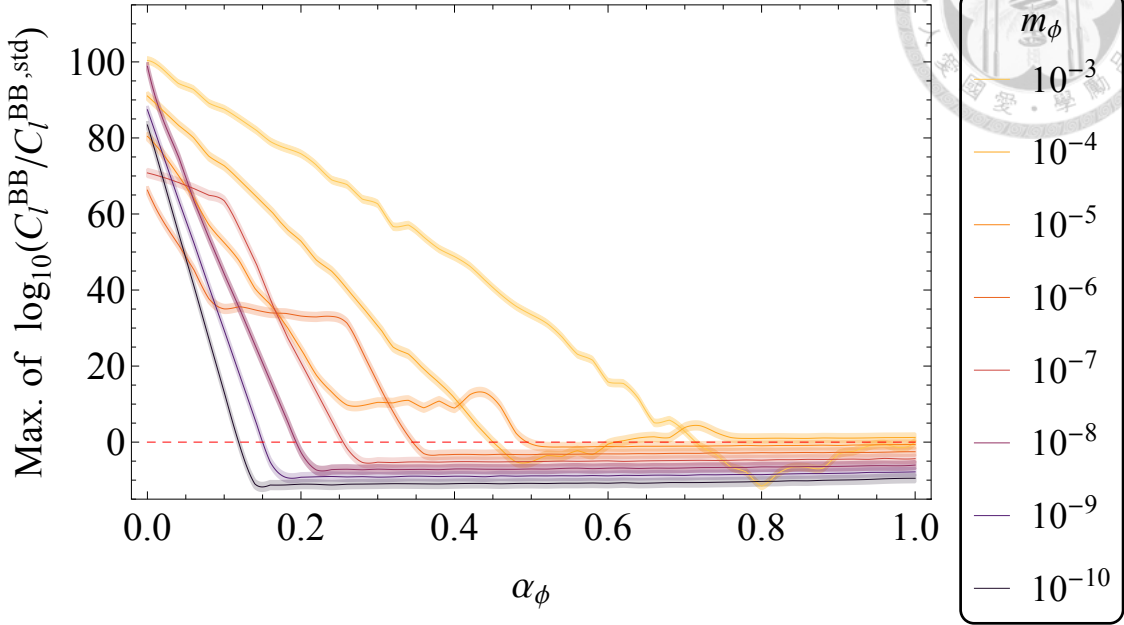
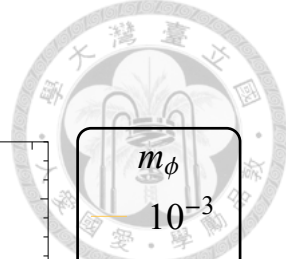


Figure 4.6: The maximum of  $C_l^{\text{BB}}/C_l^{\text{BB, std}}$  within  $20 < l < 330$  with respect to  $\alpha_\phi$  in the chaotic background with  $W = 10^{13}$ .

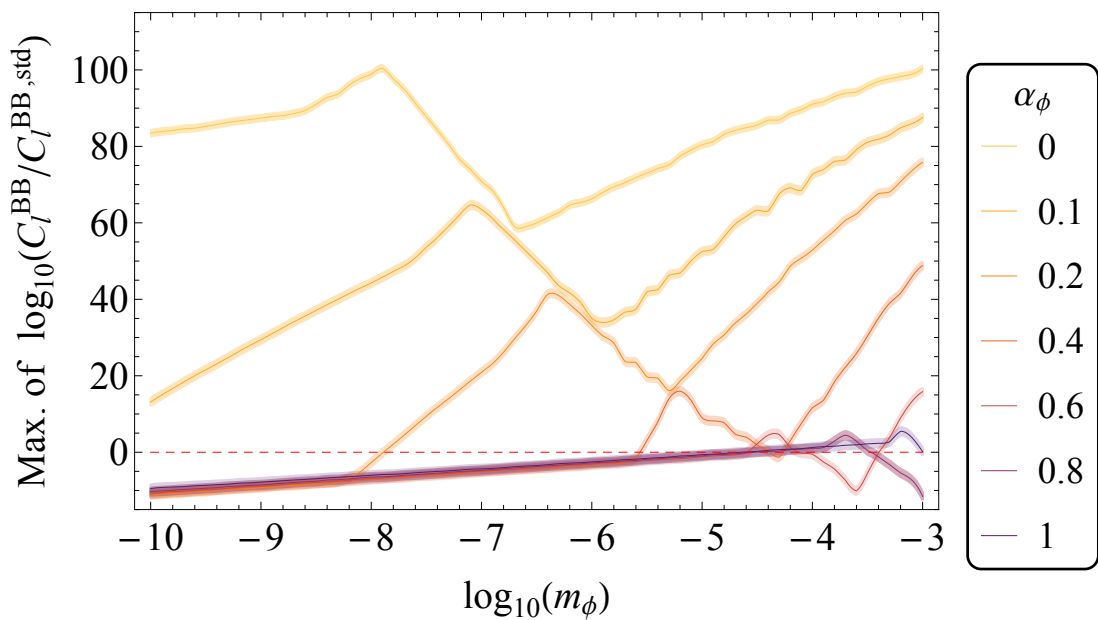


Figure 4.7: The maximum of  $C_l^{\text{BB}}/C_l^{\text{BB, std}}$  within  $20 < l < 330$  with respect to  $m_\phi$  in the chaotic background with  $W = 10^{13}$ .

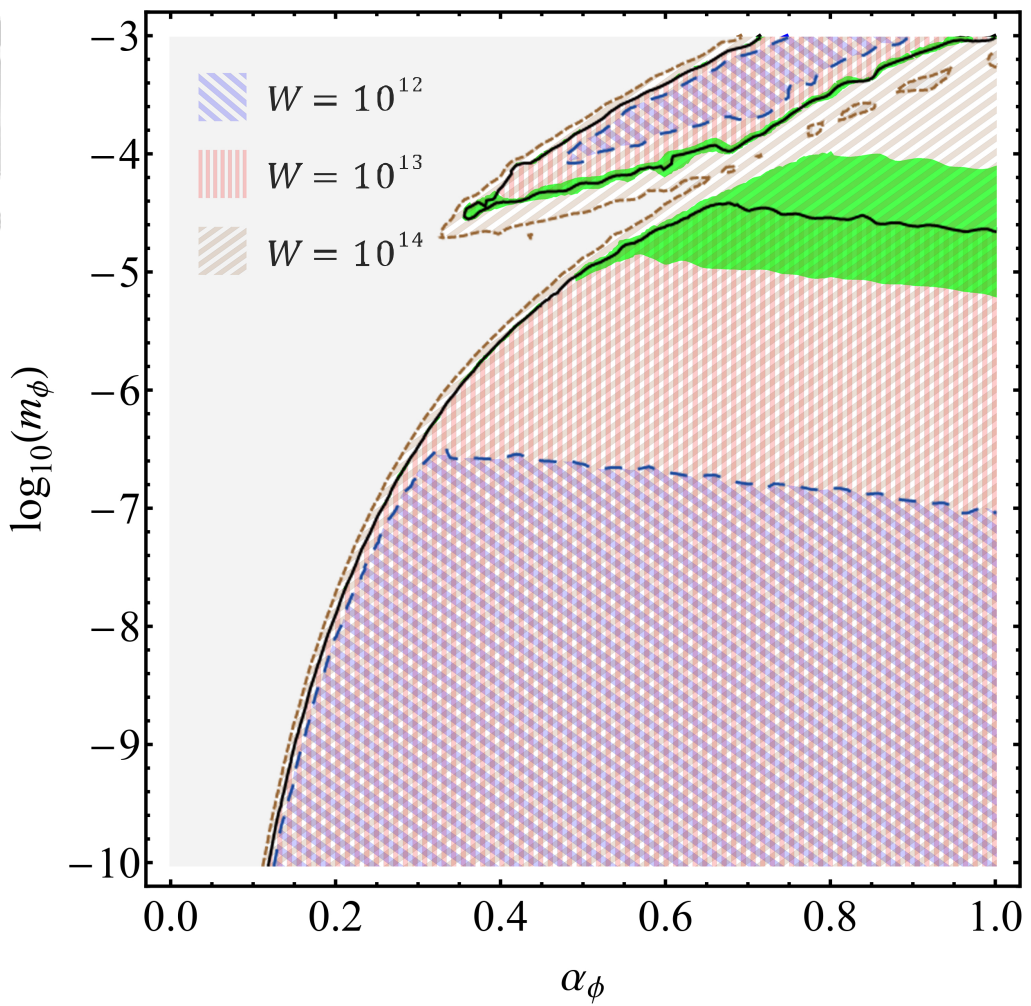


Figure 4.8: The regions of observational acceptance (shaded) in the  $(\alpha_\phi, m_\phi)$ -space with selected  $W$ 's.

and the quantum bounce. We especially note that the symmetric bouncing scenarios have already been excluded.

The green dashed curves present the variations of the upper bound corresponding to uncertainties from the initial conditions. Also, the cyan dotted curves give the upper bound when considering the rescaling factors being fixed at  $10^{12}$  (the lower curve) and  $10^{14}$  (the upper curve). Figure 4.8 displays the parameter dependence on the strength of pre-existing GWs. We find that the larger the rescaling factor is, the weaker the pre-existing GWs are. That is the reason why we choose the rescaling factor  $W = 10^{13}$  to let the predicted power spectra comparable to the observational results.

As shown in the figures presented in this subsection, we again note that it is impossible to find a universe with a symmetric bouncing scenario that satisfies the observational

realities.



#### 4.3.4 Restriction of $R^2$ background parameters

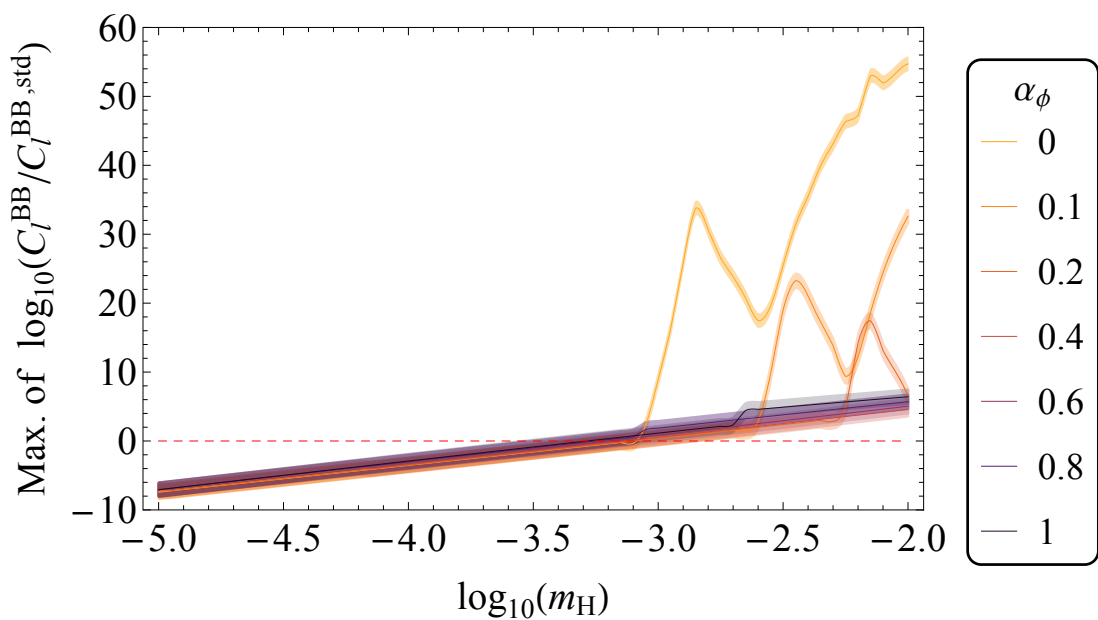
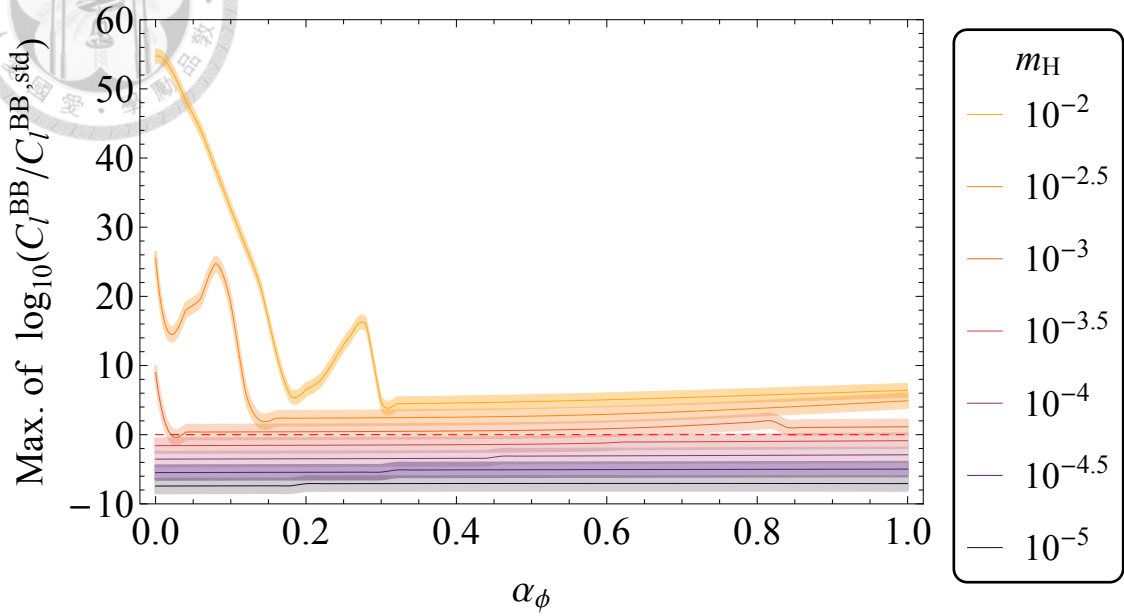
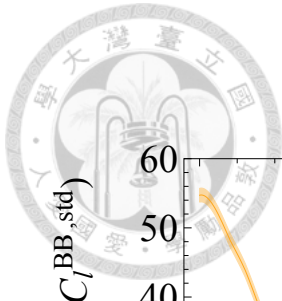
We then investigate the pre-existing GWs in the  $R^2$  background. As what we have displayed in the previous subsection, Figures 4.9 and 4.10 present the maximum of  $C_l^{\text{BB}}/C_l^{\text{BB, std}}$  with respect to the normalized  $\alpha_\phi$  and the inflaton mass  $m_H$ , respectively. In Figure 4.9, the curves with different colors correspond to different values of  $m_H$  from  $10^{-5}$  to  $10^{-2}$ . Moreover, in Figure 4.7, the curves with different colors correspond to different values of  $\alpha_\phi$  from 0 to 1. The rescaling factors in these two plots are both fixed at  $10^{12}$ .

The behaviors of pre-existing B-mode in the cosmic background with  $R^2$  potential are similar to those with the chaotic potential. However, we notice that the cosmic background with small  $\alpha_\phi$  survive this time when  $m_H$  is larger. It is because that the cosmic background are promised to be time-asymmetric to the quantum bounce when the  $R^2$  potential is considered although  $\alpha_\phi$  is exactly zero. The pre-existing GWs are diluted in the cosmic background with larger inflation and smaller deflation.

Another thing which has to be pointed out is that the cosmic background are also excluded if the inflaton is too heavy. In Figure 4.9, we can see that  $C_l^{\text{BB}}/C_l^{\text{BB, std}}$  are always greater than the observational upper bound in the cases with the  $m_H$  being  $10^{-2.5}$  and  $10^{-2}$ . It is more clear to see Figure 4.10 for this conclusion. On the contrary, they are all smaller than the upper bound if the inflaton is light enough. It seems that the strength of pre-existing GWs is controlled only by  $m_H$  rather than  $\alpha_\phi$ .

In the same way, we provide the maximum of  $C_l^{\text{BB}}/C_l^{\text{BB, std}}$  in the two-dimensional parameter space  $\{(\alpha_\phi, m_H) \in \mathbb{R}^2\}$  as a density plot in Figure 4.11. The rescaling factor, again, is fixed at  $10^{12}$ . The green solid curve presents the upper bound given by observation as before. In this plot, we can clearly see that the strength of the primordial GWs depends mainly on the  $m_H$  and almost free from  $\alpha_\phi$ . It is an alert that the future experiments may not able to constrain  $\alpha_\phi$  very well in the  $R^2$  background.

The green dashed curves present the variations of the upper bound corresponding to the uncertainties from the initial conditions. The cyan dotted curves give the upper bound



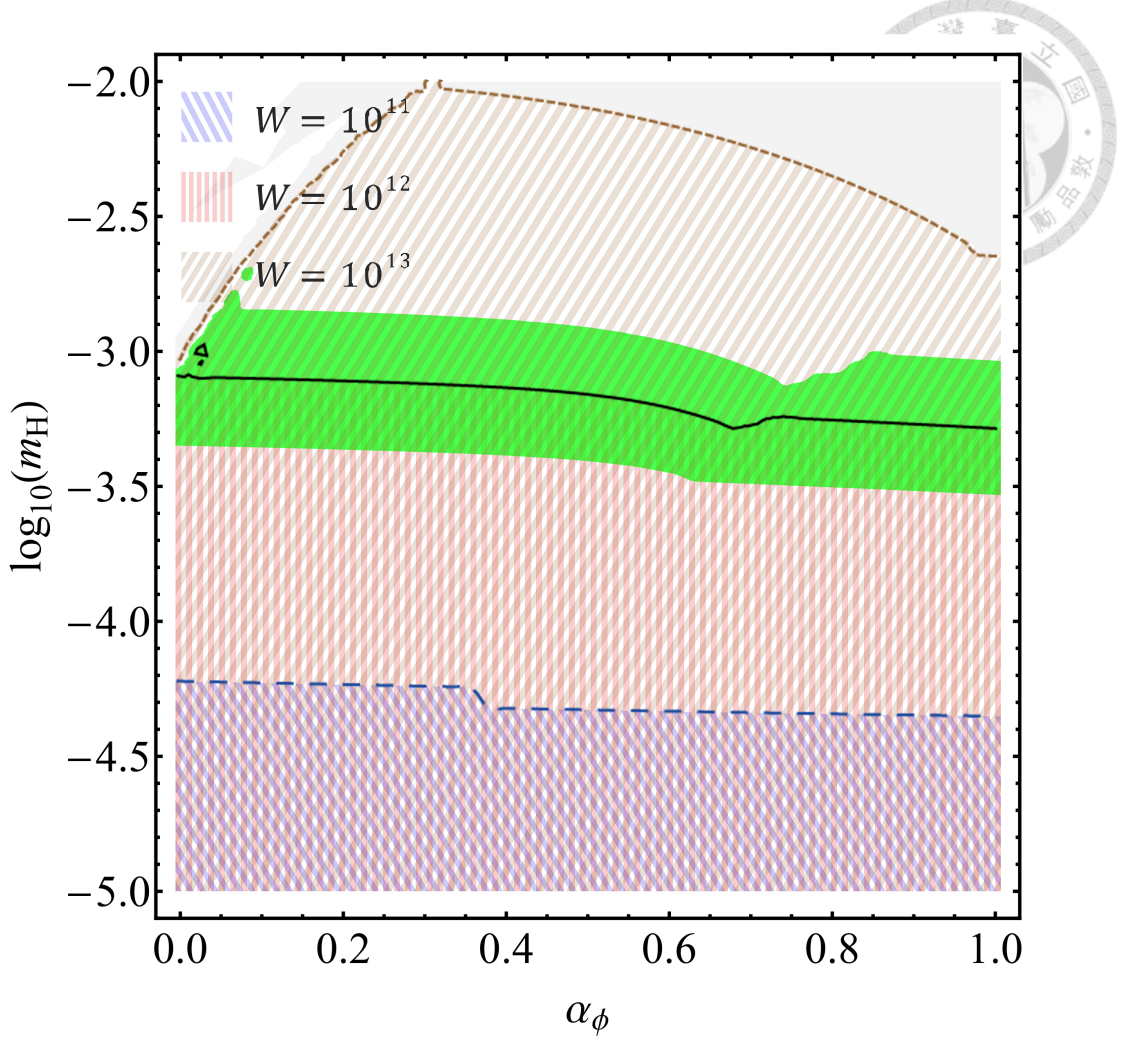


Figure 4.11: The regions of observational acceptance (shaded) in the  $(\alpha_\phi, m_H)$ -space with selected  $W$ 's.

when considering the rescaling factors being fixed at  $10^{11}$  (the lower curve) and  $10^{13}$  (the upper curve).

## 4.4 Observational Constraints

### 4.4.1 CMB TT, EE, and TE angular power spectra

In the previous section, we have discussed the observational features of the pre-existing GWs. We have compared the theoretical results of the CMB B-mode to the current concordance model. Now we compare our theoretical predictions to the observational data as well. To survive the observational test, our models must correctly predict the observed

phenomena. As expected, the pre-existing GWs must also generate the CMB TT, EE, and TE power in addition to the B-mode. Therefore, we present the total CMB TT, EE, and TE angular power spectra in this subsection.

Recalling the last section, the pre-existing GWs are expected to be significant on large scale. We show that, in this subsection, the TT, EE, and TE angular power spectra generated by the pre-existing GWs are consistent with the concordance model except for the large scale.

Figures 4.12 and 4.13 display such a conclusion for the chaotic background. The blue dashed curves are the total B-mode angular power spectra generated by the primordial GWs and the gravitational lensing. The rescaling factor is fixed at  $10^{13}$ . On the right plots of these two figures, we present only the low- $l$  region together with the Planck data points released in 2015 [58]. We can see, in the upper part of Figure 4.12, the pre-existing TT, EE, and TE (from top to bottom, the same for Figures 4.13 to 4.15 as well) in the cosmic background with different  $m_\phi$ . In this figure,  $\alpha_\phi$  is fixed at 1.0. It is clear that the larger  $m_\phi$  is, the stronger pre-existing TT, EE, and TE are. Similarly, we can see the pre-existing TT, EE, and TE in the cosmic background with different  $\alpha_\phi$  in the upper part of Figure 4.13. In this figure,  $m_\phi$  is fixed at  $10^{-7}$ . There is almost no effect when  $\alpha_\phi$  is changed between 0.6 and 1.0. According to Figures 4.12 and 4.13, we find that  $m_\phi$  is the only sensitive parameter to constrain this kind of cosmic background by using the CMB TT, EE, and EE power spectra.

Roughly speaking, the model with the chaotic potential survives when  $m_\phi$  is less than the order of  $10^{-7}$ . It is more restricted than the restriction given by the upper bound of the CMB B-mode angular power spectrum which we have presented in Subsection 4.3.3. Reviewing Figure 4.8, we can see that the CMB B-mode restricts  $m_\phi$  to be less than the order of  $10^{-5}$ .

On the other hand, the upper parts of Figures 4.14 and 4.15 present the CMB TT, EE, and TE angular power spectra in the  $R^2$  background. The rescaling factor is fixed at  $10^{12}$ . The right plots, in the similar way, display the low- $l$  region of the corresponding left plots. The fixed cosmic background parameters are  $\alpha_\phi = 1.0$  in Figure 4.14 and  $m_H = 10^{-4}$  in

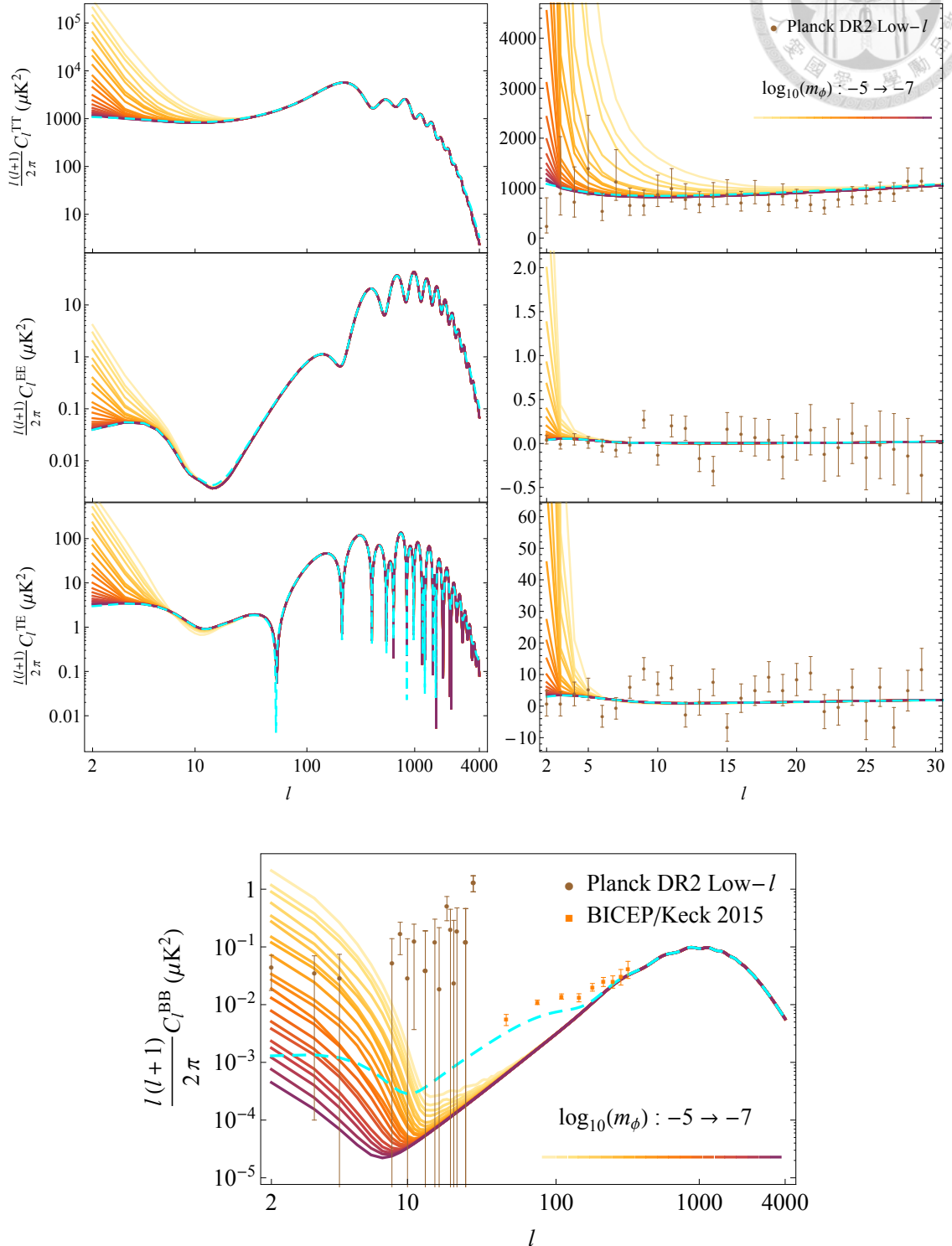
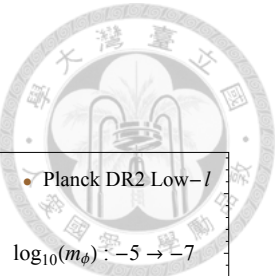


Figure 4.12: The CMB TT, EE, TE, and BB angular power spectra in the chaotic background with  $\alpha_\phi = 1.0$  and  $W = 10^{13}$  as compared to the current concordance model (dashed).

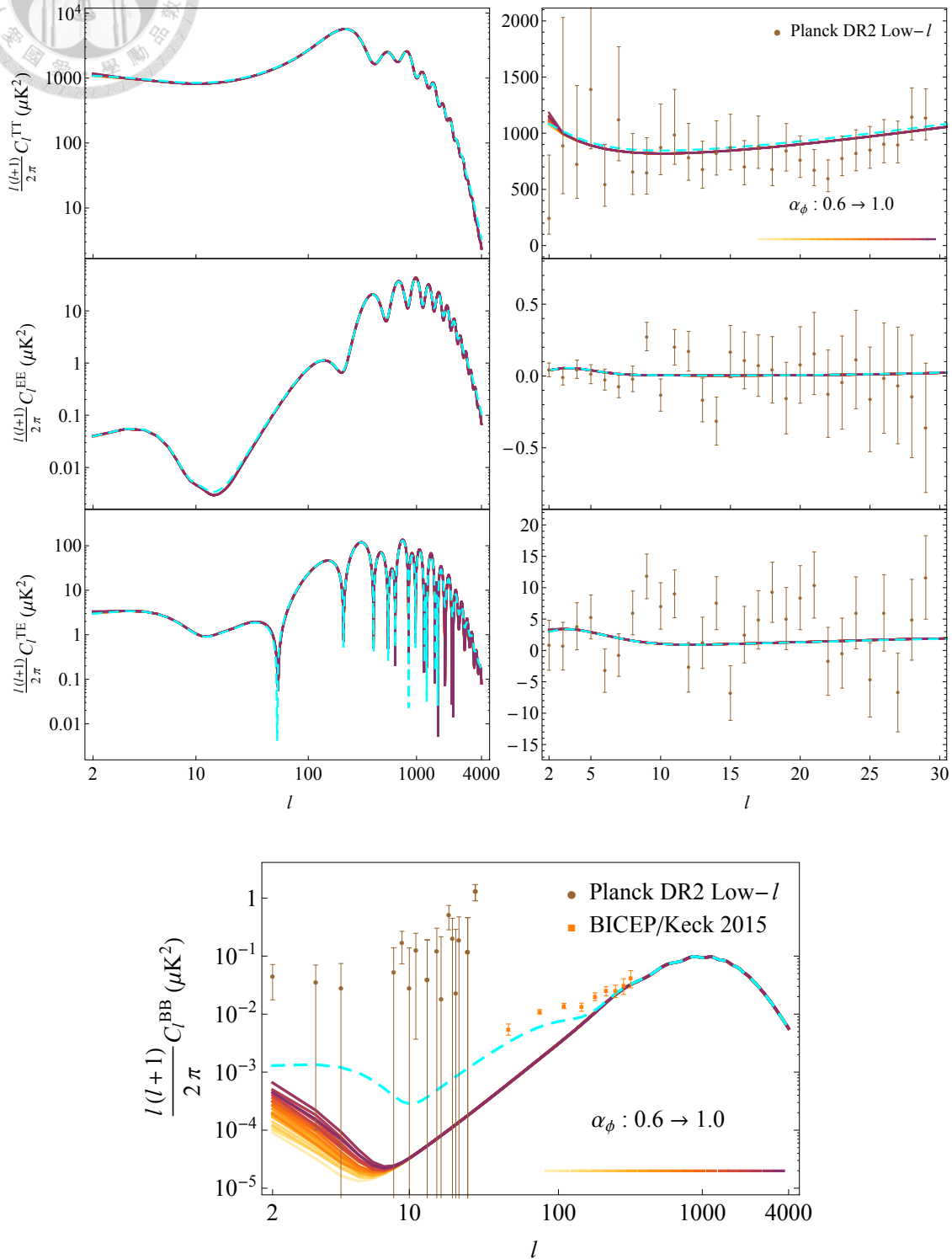
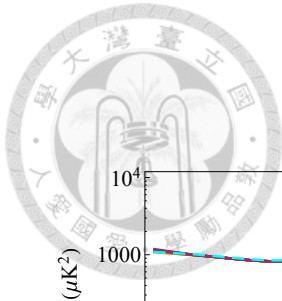


Figure 4.13: The CMB TT, EE, TE, and BB angular power spectra in the chaotic background with  $m_\phi = 10^{-7}$  and  $W = 10^{13}$ .

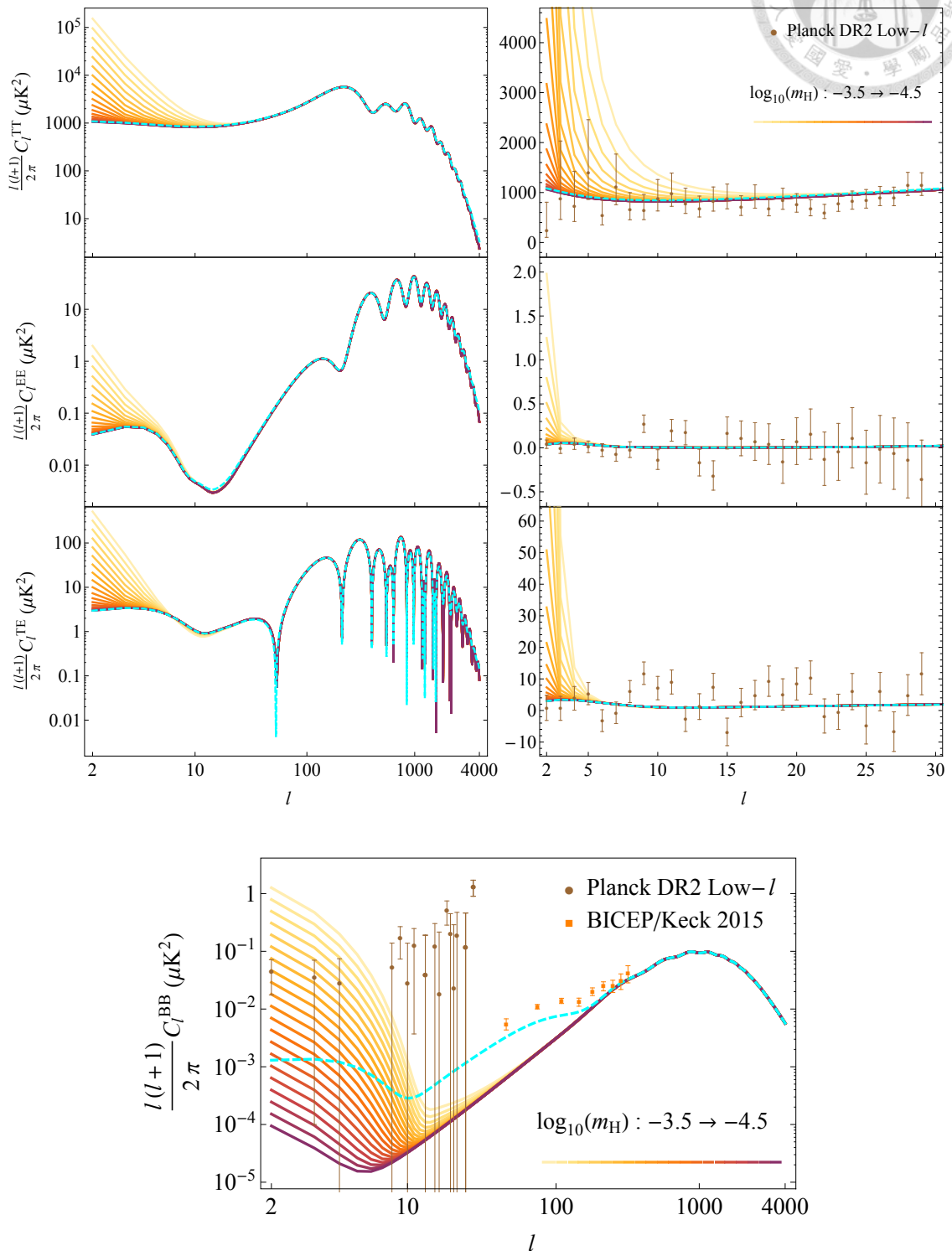


Figure 4.14: The CMB TT, EE, TE, and BB angular power spectra in the  $R^2$  background with  $\alpha_\phi = 1.0$  and  $W = 10^{12}$ .

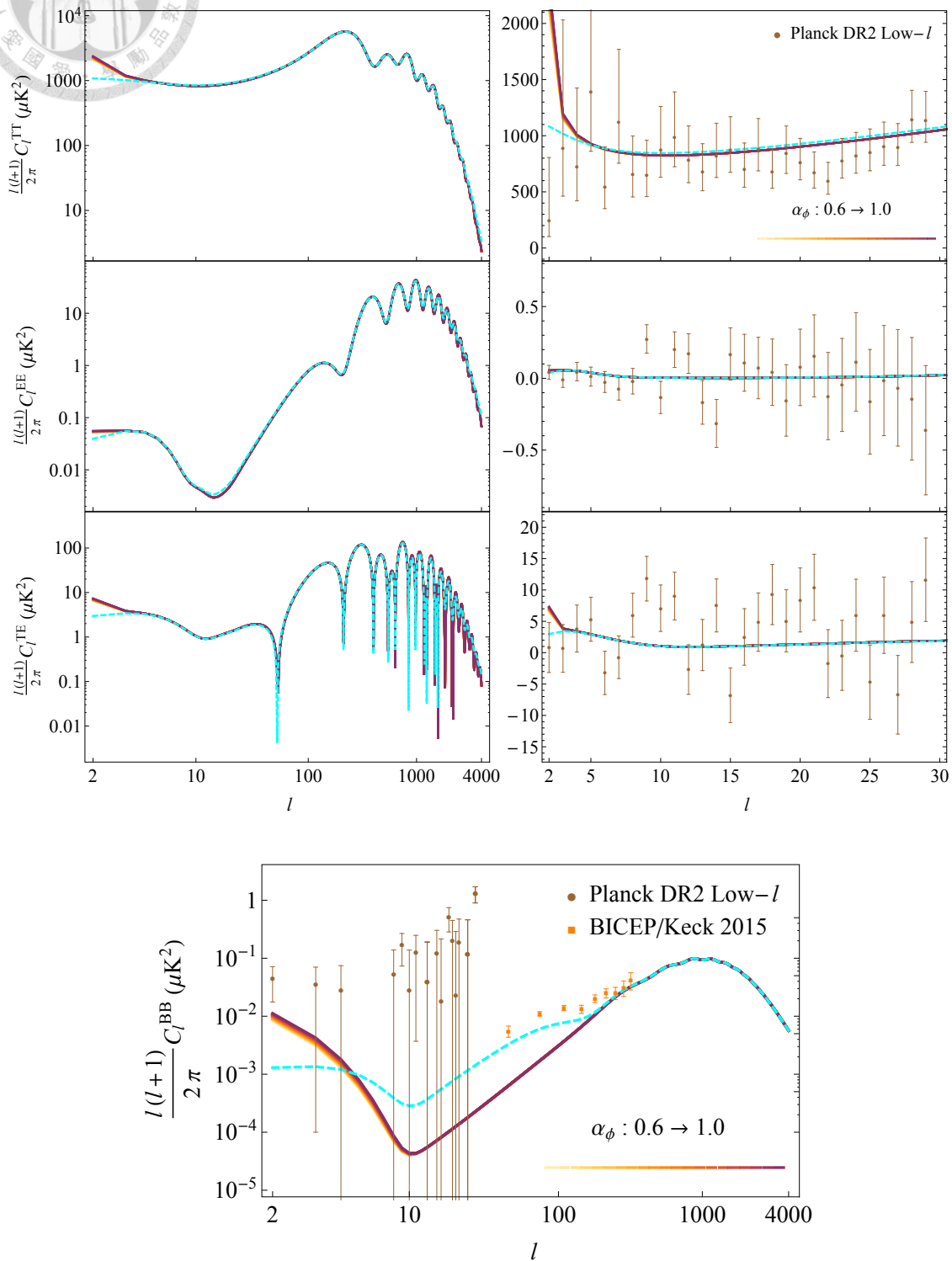
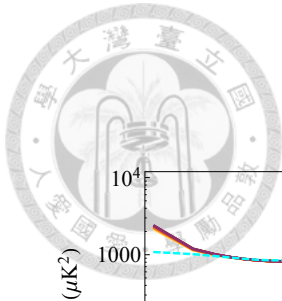


Figure 4.15: The CMB TT, EE, TE, and BB angular power spectra in the  $R^2$  background with  $m_H = 10^{-4}$  and  $W = 10^{12}$ .

Figure 4.15, respectively. It is clear that, again, the larger  $m_H$  is, the stronger pre-existing TT, EE, and TE are. In this case,  $\alpha_\phi$  dose not play a significant role of changing the CMB TT, EE, and EE power as in the chaotic background.

The model with the  $R^2$  potential survives when  $m_H$  is less than the order of  $10^{-4}$ . It is also more restricted than the restriction given by the upper bound of the CMB B-mode angular power spectrum which we have presented in Subsection 4.3.4. Reviewing Figure 4.11, we can see that the CMB B-mode angular power spectrum restricts  $m_H$  to be less than the order of  $10^{-3}$  in this model.

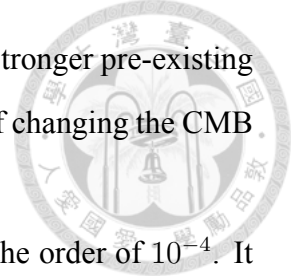
#### 4.4.2 CMB B-mode angular power spectrum

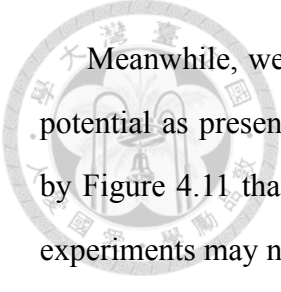
However, the pre-existing B-mode is distinguishable to the concordance model with  $r = 0.07$  not only on the large scale but also on the medium scale as we have mentioned in Section 4.3. We additionally present the B-mode angular power spectra in the cosmological models considered in the last subsection.

The lower parts of Figures 4.12 and 4.13 display the pre-existing B-mode angular power spectra in the chaotic background. In this subsection, we add the observational data released by the BICEP2/Keck experiment in 2015 [41]. The blue dashed curves are the total B-mode angular power spectra generated by the primordial GWs and the gravitational lensing. We have known from Section 4.3 that the primordial GWs are far weaker than the pre-existing GWs. The bump on the B-mode angular power spectrum on the medium scale predicted by the non-zero primordial GWs disappears in our models. Consequently, we can observe that the pre-existing B-mode dominates the gravitational lensing on the large scale.

Similarly, the lower parts of Figures 4.14 and 4.15 display the pre-existing B-mode angular power spectra in the  $R^2$  background. The conclusions are basically the same with the cases of chaotic potential except for the effect of changing  $\alpha_\phi$ .

Reviewing Figure 4.13, we find that varying  $\alpha_\phi$  changes the B-mode angular power spectrum only. That is to say, we can constrain  $\alpha_\phi$  by using the B-mode angular power spectrum in this model. It is consistent with the result given by Figure 4.8.





Meanwhile, we find that it is hard to reach the same thing in the model with the  $R^2$  potential as presented in Figure 4.15. The conclusion is identical with the result given by Figure 4.11 that  $m_H$  is the only sensitive parameter to the CMB power. The future experiments may not able to constrain  $\alpha_\phi$  very well in the  $R^2$  background.

## 4.5 Summary

We used the transfer functions to evolve the pre-existing GWs, in particular those generated by stellar binary systems in the parent universe, and obtained the corresponding GW power spectra and the angular power spectra of the CMB B-mode polarization. As the result, the behaviors of the pre-existing GWs are different from the primordial ones resulting distinguishable features on large ( $l < 30$ ) and medium ( $30 < l < 200$ ) scale. This allows us to probe and test the parent universe by using not only space-based but also ground-based experiments.

Our results successfully constrain the LQC parameters with the current observational upper bound given by BICEP2/Keck. We realized that a cosmic background with a heavier inflaton mass and smaller  $\phi_B$  is observationally disfavored. This is again saying that a time-asymmetric bouncing scenario is required to solve the cosmological conundrums. We found that the time-symmetric bounce scenarios are ruled out and the inflationary models that have been ruled out are possible to revive within our framework.

Finally we compared the TT, EE, and TE angular power spectra in our scenario with the concordance model as well as the observational data from Planck and BICEP2/Keck experiments. We found that our model is consistent with the present understanding of cosmology. We conclude that the scenario of having a parent universe in the LQC is being observationally confined and can soon be decisively tested by observations.

In the follow-up chapter we will provide a possible solution to the UV divergence problem in the scalar counterpart. The scalar perturbations do not have to diverge around the quantum bounce. Therefore the LQC models are worthy further studies in more details. After all the pre-existing GWs must survive the quantum bounce because they are essentially decoupled from the cosmic contents, including the inflaton.



# Chapter 5

## The UV Divergence on Scalar Perturbations

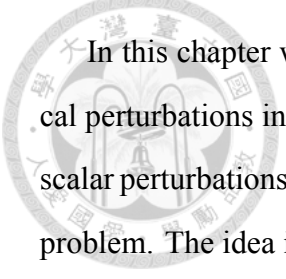
*“A free man thinks of death least of all things, and his wisdom is a meditation not of death but of life.”*

— Baruch Spinoza

### 5.1 Overview

In the previous chapters, we have already proposed a complete framework to probe the parent universe by using the angular power spectrum of CMB, in particular the B-mode polarization, induced by the GW background in the parent universe. We employed the transfer functions to evolve such pre-existing GWs from their initial states to the CMB B-mode imprints today. On top of that, our context is expected to be observationally tested soon by both space-based and ground-based instruments.

In addition to the pre-existing GWs, however, we find that our context must predict pre-existing scalar perturbations which can lead to a so-called “UV divergence” problem [100, 101]. This problem practically makes our model inconsistent with the observational results, even violates the fundamental physics as well as the fact of the existence of our present universe.



In this chapter we start by Section 5.2 with the theory of gauge-invariant cosmological perturbations in LQC [102–104] and introduce the UV divergence of the pre-existing scalar perturbations. Then in Sections 5.3 we shall propose a possible scenario to solve this problem. The idea is mainly coming from Firouzjshi’s study [105] which considered that our universe was born inside a Schwarzschild-de Sitter black hole. We show in Subsection 5.3.3 that the boundary conditions at the event horizon of a black hole can eliminate the UV divergence. Finally we conclude this chapter in Section 5.4.

## 5.2 Scalar Perturbations in LQC

### 5.2.1 Evolutionary equation

The scalar perturbations are sourced by the scalar field and curvature. In the case of single scalar field, the gauge-invariant curvature perturbation on comoving hypersurface  $\mathcal{R}_c \equiv \mathcal{R}_c(\mathbf{x}, t)$  can be related to the perturbed field  $\delta\phi \equiv \delta\phi(\mathbf{x}, t)$  and intrinsic curvature perturbation  $\mathcal{R} \equiv \mathcal{R}(\mathbf{x}, t)$  by [106]

$$\mathcal{R}_c = \mathcal{R} - \frac{H}{\dot{\phi}}\delta\phi, \quad (5.1)$$

where  $\phi \equiv \phi(\mathbf{x}, t) = \bar{\phi}(t) + \delta\phi(\mathbf{x}, t)$  is the given scalar field with  $\bar{\phi}(t)$  the unperturbed average and  $H = \dot{a}/a$  is the Hubble parameter with  $a$  the scale factor. The equation describing  $\mathcal{R}_c$  in the quantum regime in Fourier space is given by [101, 107, 108]

$$\ddot{\tilde{\mathcal{R}}}_{ck} - \left( 3H + 2\frac{V^2}{\dot{V}} + 2\frac{\dot{H}}{H} \right) \dot{\tilde{\mathcal{R}}}_{ck} + \Omega \frac{k^2}{a^2} \tilde{\mathcal{R}}_{ck} = 0, \quad (5.2)$$

where  $\tilde{\mathcal{R}}_{ck}$  is the mode function of  $\mathcal{R}_c$  with  $\mathbf{k}$  the wave vector and  $k \equiv |\mathbf{k}|$  its module,  $V \equiv V(\phi)$ , and  $\Omega = 1 - 2\rho/\rho_c$  is the deformation factor [104]. It is clear that  $\Omega$  equals to one in the classical regime (i.e. Lorentzian spacetime), becomes smaller in the quantum regime, and finally reaches minus one at the quantum bounce (i.e. Euclidean spacetime) [101, 109]. The upper panel of Figure 5.1 demonstrates the time evolution of  $\Omega$  in the quantum bounce epoch. The curvature perturbations, therefore, evolve from an Euclidean-

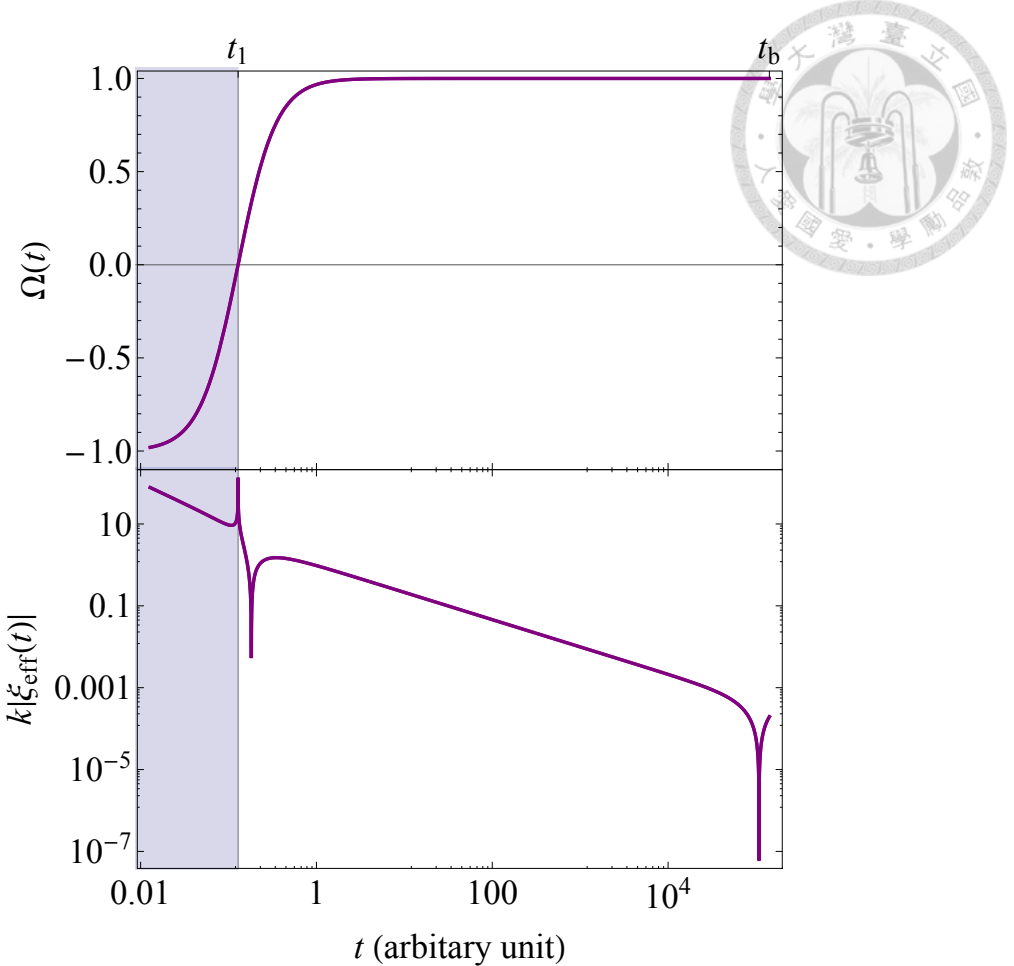


Figure 5.1: Time evolution of the deformation factor and effective damping ratio between the quantum bounce and the beginning of inflation.

like spacetime (shaded) to a Lorentzian-like spacetime (blank) after the quantum bounce. We now define  $t_1$  by  $\Omega(t_1) = 0$  as shown in the figure.

It is obvious that a singularity appears in  $\dot{\mathcal{R}}_{\text{ck}}$  term of Equation (5.2) at the quantum bounce (i.e.  $H = 0$ ), which has been discovered and studied by Schander *et al.* [101]. The singularity, however, is not physical. Schander *et al.* provided an approximated solutions of  $\dot{\mathcal{R}}_{\text{ck}}$  around the quantum bounce with the chaotic potential [101]. The behavior of  $\dot{\mathcal{R}}_{\text{ck}}$  is no doubt kept regular all the way and hence survive the quantum bounce as expected.

Here we define the effective damping ratio of Equation (5.2) by

$$\zeta_{\text{eff}} = \frac{-a}{2k\sqrt{|\Omega|}} \left( 3H + 2\frac{V^2}{\dot{V}} + 2\frac{\dot{H}}{H} \right) \quad (5.3)$$

and plot it in the lower panel of Figure 5.1.

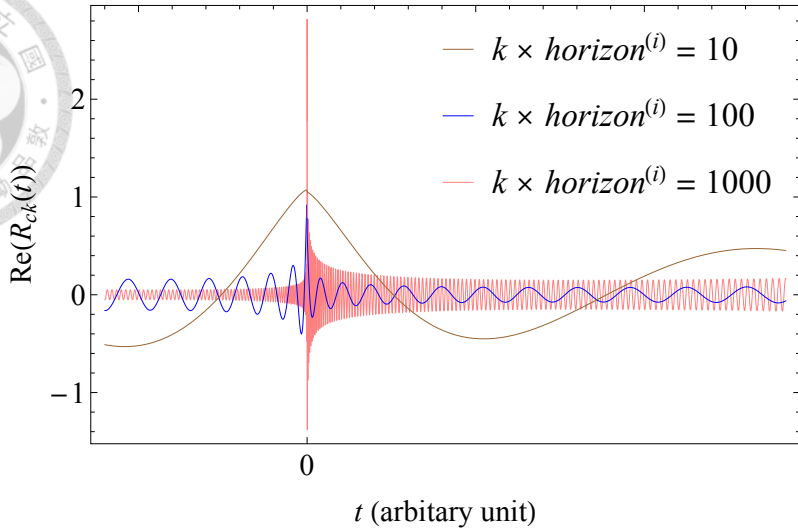


Figure 5.2: Time evolution of  $\tilde{\mathcal{R}}_{ck}$  with different  $k$  across the quantum bounce.

The numerical solutions of  $\tilde{\mathcal{R}}_{ck}$  for several  $k$  in the chaotic background is provided in Figure 5.2. Here the wavenumber  $\mathbf{k}$  has been replace by its module  $k$  because of the cosmological principle.

We further define the function  $v$  by [104]

$$v = v(\mathbf{x}, \eta) = z\mathcal{R}_c \quad (5.4)$$

with  $z \equiv a\dot{\phi}/H$ . By performing a Fourier transform to  $k$ -space, the evolutionary equation of the mode function  $\tilde{v}_k$  can be written as [104]

$$\tilde{v}_k''(\eta) + k_{\text{eff}}^2 \tilde{v}_k(\eta) = 0, \quad (5.5)$$

where  $k_{\text{eff}}$  is the effective wavenumber given by [104]

$$k_{\text{eff}} = \sqrt{\Omega k^2 - \frac{z''}{z}}. \quad (5.6)$$

The most crucial thing in Equation (5.5) is the sign of  $k_{\text{eff}}^2$ . When  $k_{\text{eff}}^2 < 0$  near the quantum bounce,  $\tilde{\mathcal{R}}_{ck}$  behaves hyperbolically rather than harmonically. On the other hand, it oscillates as a wave when  $k_{\text{eff}}^2 > 0$  far from the quantum bounce. The transition, however, is very closed to the quantum bounce. Consequently  $\tilde{\mathcal{R}}_{ck}$  must be observed as oscillating

most of the time as shown in Figure 5.2. We note that Equation (5.6) contains a non-regular singularity in term of  $z''/z$  at  $t = 0$  hence it is physically invalid at the quantum bounce.

The power spectrum of scalar perturbations at the end of inflation is

$$P_S(k) = \frac{4}{9} |\tilde{\mathcal{R}}_{ck}(\eta_e)|^2 = \frac{4}{9z^2} |\tilde{v}_k(\eta_e)|^2. \quad (5.7)$$

### 5.2.2 The UV divergence problem

In this subsection, we study the sub-horizon perturbations which we are interested in. As shown in the lower panel of Figure 5.1,  $\zeta_{\text{eff}}$  becomes smaller when  $t$  goes larger. There shall be  $|t_2| < |t_1|$  that  $\zeta_{\text{eff}}(t_2) = \text{sign}(\Omega)$  if  $k$  is large enough, say  $k \times \text{horizon}^{(i)} \geq 100$ . An approximation on the damping term of Equation (5.2) has been suggested by the previous works [101, 110]

$$2k\zeta_{\text{eff}} \frac{\sqrt{|\Omega|}}{a} \approx -2 \frac{\dot{H}}{H} \rightarrow -\frac{2}{t} \quad (5.8)$$

near the quantum bounce. It means that we are able to define  $t_2 \equiv 1/k$  since  $\Omega \rightarrow -1$  and  $a \rightarrow 1$  when  $t \rightarrow 0$ . This definition is, obviously, only valid for  $k > 1/t_1$ . More so, we notice that  $\Omega/a^2$  is proportional to  $t^{-2/3}$  when  $t \gg t_1$ . In general, we divide the quantum bounce epoch into five stages as shown in Figure 5.3. For a time-asymmetric cosmic background, we further define  $t_1^{(-)}$  and  $t_2^{(-)}$  corresponding to  $t_1$  and  $t_2$  mentioned above (labelled as  $t_1^{(+)}$  and  $t_2^{(+)}$  here) in the age before the quantum bounce. The reason is that  $t_1^{(-)}$  and  $t_2^{(-)}$  are generally unequal to  $t_1^{(+)}$  and  $t_2^{(+)}$ , respectively.

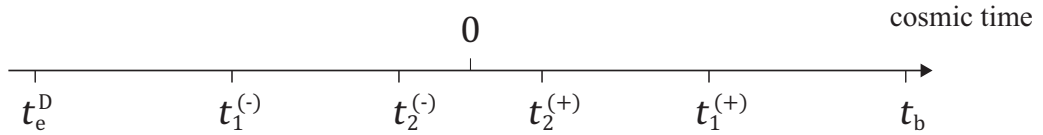
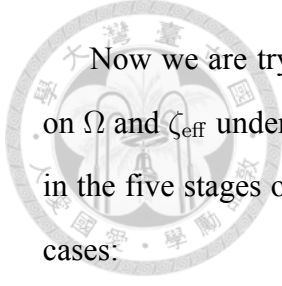


Figure 5.3: A conceptual time division of the quantum bounce epoch for approximating the scalar perturbations.



Now we are trying to derive the analytical solutions with taking the approximations on  $\Omega$  and  $\zeta_{\text{eff}}$  under the large- $k$  limit. According to the above discussions, Equation (5.2) in the five stages of quantum bounce epoch can be approximated by the following three cases:

$$\ddot{\tilde{\mathcal{R}}}_{ck} - \frac{2}{t} \dot{\tilde{\mathcal{R}}}_{ck} - k^2 \tilde{\mathcal{R}}_{ck} = 0 \quad \text{for } t_2^{(-)} < t < t_2^{(+)}, \quad (5.9a)$$

$$\ddot{\tilde{\mathcal{R}}}_{ck} - k^2 \tilde{\mathcal{R}}_{ck} = 0 \quad \text{for } t_1^{(-)} < t \leq t_2^{(-)} \text{ and } t_2^{(+)} \leq t < t_1^{(+)}, \quad (5.9b)$$

$$\ddot{\tilde{\mathcal{R}}}_{ck} + \beta t^{2/3} k^2 \tilde{\mathcal{R}}_{ck} = 0 \quad \text{for } t \leq t_1^{(-)} \text{ and } t \geq t_1^{(+)}. \quad (5.9c)$$

The parameter  $\beta$  is a proportional constant which is determined numerically. First of all, the independent solutions of Equation (5.9a) is provided by [101]

$$\tilde{\mathcal{R}}_{ck}^{(a,1)} = \sin(kt) - kt \cos(kt) \quad \text{and} \quad \tilde{\mathcal{R}}_{ck}^{(a,2)} = \cos(kt) - kt \sin(kt). \quad (5.10)$$

Here we can apparently see that  $\tilde{\mathcal{R}}_{ck}$  is regular at  $t = 0$ . Also, by the definition of  $t_2^{(\pm)}$ , the argument  $|kt|$  for these solutions must always be less than one. Secondly, the solutions of Equation (5.9b) are simply the exponential functions

$$\tilde{\mathcal{R}}_{ck}^{(b,1)} = e^{kt} \quad \text{and} \quad \tilde{\mathcal{R}}_{ck}^{(b,2)} = e^{-kt}, \quad (5.11)$$

which lead to a divergence when  $|kt|$  goes large. This is in fact the mathematical origin of the UV divergence problem. Finally, the solutions of Equation (5.9c) are given by [111, 112]

$$\tilde{\mathcal{R}}_{ck}^{(c,1)} = \sqrt{t} J_{3/4} \left( \frac{3}{2} \sqrt{\beta} k t^{2/3} \right) \quad \text{and} \quad \tilde{\mathcal{R}}_{ck}^{(c,2)} = \sqrt{t} Y_{3/4} \left( \frac{3}{2} \sqrt{\beta} k t^{2/3} \right). \quad (5.12)$$

Because  $|kt_1^{(\pm)}|$  must be much greater than one under our definition, Equation (5.12) can be reduced by applying large-argument approximations of the Bessel functions as

$$\lim_{kt \rightarrow \infty} \tilde{\mathcal{R}}_{ck}^{(c,1)} = \sqrt{\frac{t^{1/3}}{k}} \cos\left(kt' - \frac{\pi}{8}\right) \quad \text{and} \quad \lim_{kt \rightarrow \infty} \tilde{\mathcal{R}}_{ck}^{(c,2)} = \sqrt{\frac{t^{1/3}}{k}} \sin\left(kt' - \frac{\pi}{8}\right), \quad (5.13)$$

where  $t' \equiv 3\sqrt{\beta}t^{2/3}/2$ .

We study, in particular, the epoch before the quantum bounce. The second solution within  $t_1^{(-)} < t \leq t_2^{(-)}$  shown in Eqs. (5.11),  $\tilde{\mathcal{R}}_{ck}^{(b,2)}$ , which contains exponentially growing term, leads to the UV divergence and thus an unbounded  $P_S(k)$ . However, we have never observed any divergent scalar perturbation in the real world. Furthermore, the quantum fluctuations from vacuum must be virtual according to the uncertainty principle of quantum mechanics. The expected value of energy of quantum fluctuations is therefore linearly limited with respect to  $k$ . It means that the exponentially growing term is definitely not a physical solution.

Mathematically, the way to prevent the UV divergence is to reduce the degree of freedom of  $\tilde{\mathcal{R}}_{ck}^{(b,2)}$ . The general solution of  $\tilde{\mathcal{R}}_{ck}^{(b)}$  turns out to contain only  $\tilde{\mathcal{R}}_{ck}^{(b,1)}$  rather than the linear combination of  $\tilde{\mathcal{R}}_{ck}^{(b,1)}$  and  $\tilde{\mathcal{R}}_{ck}^{(b,2)}$ . Under this consideration, instead of blowing up dramatically,  $\tilde{\mathcal{R}}_{ck}^{(b)}$  is smeared out during  $t_1^{(-)} < t \leq t_2^{(-)}$  by a factor of  $e^{-k(t_2^{(-)} - t_1^{(-)})}$ . The resulting  $P_S(k)$  thus returns to  $P_S^{\text{std}}(k)$  and hence agrees with the current observational results.

In the following sections, we find that the UV divergence is possible to be physically solved if we consider our universe as a ‘‘baby universe’’ born inside a black hole. The reason is that the boundary conditions on the event horizon of the black hole indeed prohibit the exponentially growing term.

## 5.3 The Parent Black Hole

### 5.3.1 Spacetime geometry

There have been lots of literatures considering the black hole interior as a new separate universe [113–117]. This idea is now probable to be achieved by LQG after a decade hard work. Recently, Bojowald suggested in his paper [118] that there are two scenarios for Hawking-evaporating black holes [119–121]. The first one is without an event horizon. In this scenario, the event horizon is replaced by an apparent horizon which encloses the black-hole region such that the interior and exterior regions will eventually reconnect to

each other [122–125]. Another scenario is that the black-hole interior can split off into a baby universe which is causally disconnected with the exterior universe.

To deal with the UV divergence problem specified in the last section, we propose a “parent black hole” which undergoes the second scenario. This proposal is quite intuitive if we assume that the parent universe looked like our present universe and contained commonly known gravitationally bounded systems including black holes. Under this assumption, we claim that people can only observe the perturbations originally inside the event horizon because our universe is causally disconnected with the external universe. Any perturbation from the black hole exterior is not allowed to travel accross the event horizon in a finite time. In other words, the pre-existing perturbations are now the GW background from the parent universe and the quantum fluctuations inside the black hole.

There have been literatures discussing Schwarzschild black holes in the context of LQG [126–132]. Some of them even used semi-classical approaches. However, instead of studying loop quantum black hole directly, we study the quantum bounce which naturally occurs at the center of a Schwarzschild black hole. We have known that the quantum bounce occurs when the energy density reaches the critical value  $\rho_c^{(n)}$  [47], where  $n$  denotes that we account the holonomies up to the  $n$ -th order. Not only a contractive parent universe but also a black hole can trigger the quantum bounce [133] if the total rest mass of the black hole is heavy enough.

First of all, we introduce a toy calculation to establish the condition of black hole formation in LQG. A Schwarzschild black hole in the GR forms when a rest mass  $M_\bullet$  distributes within the radius  $r_{\text{sch}} = 2M_\bullet$  (known as event horizon). The average density of the Schwarzschild black hole is

$$\rho_{\text{sch}} = \frac{3}{32\pi} M_\bullet^{-2} \approx 3.2656 \times 10^{-40} \left( \frac{M_\bullet}{M_\odot} \right)^{-2}, \quad (5.14)$$

where  $M_\bullet$  denotes the mass of black hole. This result implies that, in LQG, for an astronomical black hole whose rest mass is much larger than the square root of  $3/32\pi\rho_c^{(n)}$  the quantum bounce occurs inside its event horizon because  $\rho_{\text{sch}} < \rho_c^{(n)}$ , and in the contrary an uniform object with  $M_\bullet^2 < 3/32\pi\rho_c^{(n)}$  does not form a black hole because the quantum



bounce occurs at  $\rho_c^{(n)} < \rho_{\text{sch}}$ .

We now consider a Schwarzschild black hole embedded in a FRW spacetime. The metric of this so-called “Schwarzschild-FRW black hole” is given by [134]

$$ds^2 = - \left( \frac{1 - \frac{2M_\bullet}{ay} \sqrt{1 + \frac{Ky^2}{4}}}{1 + \frac{2M_\bullet}{ay} \sqrt{1 + \frac{Ky^2}{4}}} \right)^2 dt^2 + \frac{a^2}{\left(1 + \frac{Ky^2}{4}\right)^2} \left( 1 + \frac{2M_\bullet}{ay} \sqrt{1 + \frac{Ky^2}{4}} \right)^4 (dy^2 + y^2 d\Omega^2), \quad (5.15)$$

where  $y$  is a variable defined by the Schwarzschild radius  $r$  (not the tensor-to-scalar ratio hereafter in this chapter) as [134]

$$r = \frac{y}{2} \left( 1 + \frac{M_\bullet}{y} \right)^2. \quad (5.16)$$

The Schwarzschild-FRW black hole reduces to the static Schwarzschild black hole when  $K = 0$  and  $a = \text{const}$ . Furthermore, the result of a “Schwarzschild-de Sitter black hole” is also obtained by taken  $K = 0$  and  $a = e^{Ht}$  with  $H$  a constant  $H_\Lambda = \sqrt{\Lambda/3}$ .

We can further reduce the Schwarzschild-de Sitter metric to a de Sitter metric by requiring  $M_\bullet = 0$ . With the following tramsformations of variables from  $(t, r)$  to  $(\bar{t}, \bar{r})$ :

$$r = \frac{\bar{r}}{a} \quad \text{and} \quad t = \bar{t} + \frac{1}{H_\Lambda} \log \left( \sqrt{1 - H_\Lambda^2 \bar{r}^2} \right). \quad (5.17)$$

Equation (5.15) simply returns to the familiar form of a de Sitter metric

$$ds^2 = -(1 - H_\Lambda^2 \bar{r}^2) d\bar{t}^2 + \frac{d\bar{r}^2}{1 - H_\Lambda^2 \bar{r}^2} + \bar{r}^2 d\Omega^2. \quad (5.18)$$

It means that a de Sitter contraction (i.e. deflation), as well as the follow-up quantum bounce, can occur inside a collapsing Schwarzschild-de Sitter black hole.

Figure 5.4 shows the conceptual Penrose-Carter diagram of the scenario that our present universe was born inside a Schwarzschild black hole in the parent universe.

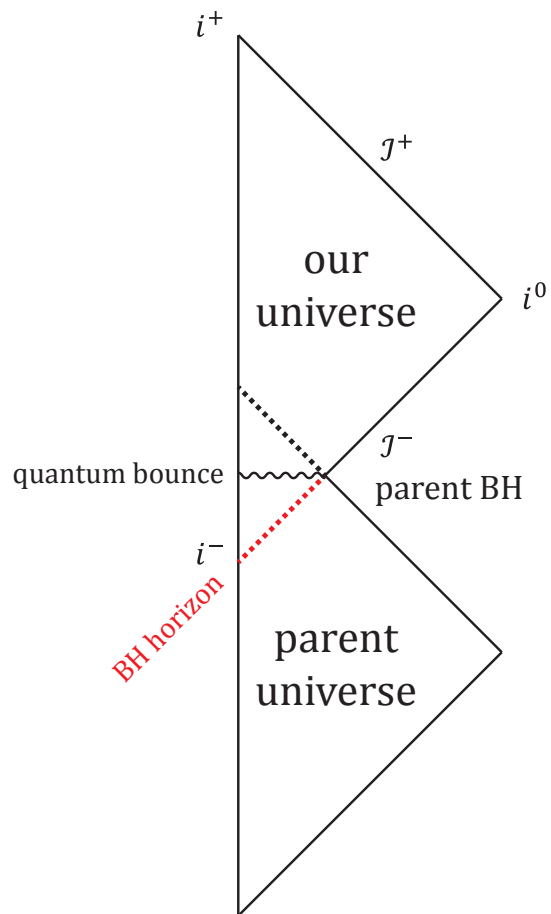
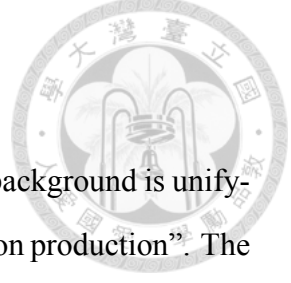


Figure 5.4: A conceptual Penrose-Carter diagram of the scenario that our present universe was born inside a Schwarzschild black hole.



### 5.3.2 Inflaton production

The key to connect a Schwarzschild black hole interior to a LQC background is unifying ordinary matters to inflaton. This procedure is what we call “inflaton production”. The unification comes before deflation, makes  $M_\bullet$  zero, and thus returns a Schwarzschild-de Sitter metric to a de Sitter metric. Consequently, we can easily use the LQC Hamiltonian to describe the quantum bounce inside the black hole.

The concept of inflaton production can be simply thought as a bunch of inversed processes of inflaton decay, known as reheating, occurring at the end of standard inflation. According to the literatures [135–137], for example with a chaotic potential, there are parametric (narrow) and broad resonances during the reheating. It converts the classical inflaton  $\phi$  to a quantum scalar field  $\chi$  which can be a proxy for the ordinary matters, namely, the standard model particles.

For simplicity, we here consider a toy model with a quadratic interaction

$$\mathcal{L}_{\text{int}} = -\frac{1}{2}g^2\chi^2\phi^2 \quad (5.19)$$

scaled by a dimensionless coupling constant  $g$ . The transition amplitude of converting a pair of  $\chi$ -particles with momenta  $\mathbf{p}_1$  and  $\mathbf{p}_2$  to a pair of  $\phi$ -particles with momenta  $\mathbf{q}_1$  and  $\mathbf{q}_2$  in vacuum is

$$\begin{aligned} \mathcal{A} &\equiv \langle \mathbf{q}_1, \mathbf{q}_2 | \mathcal{T} e^{i \int d^4x \mathcal{L}_{\text{int}}} | \mathbf{p}_1, \mathbf{p}_2 \rangle \\ &\simeq -\frac{ig^2}{2} \int d^4x \langle \mathbf{q}_1, \mathbf{q}_2 | \hat{\phi}^2 \hat{\chi}^2 | \mathbf{p}_1, \mathbf{p}_2 \rangle, \end{aligned} \quad (5.20)$$

where  $\mathcal{T}$  is the time ordering symbol. We now consider both  $\phi$  and  $\chi$  as quantum fields. The interacting representation for  $\phi$  and  $\chi$  are

$$\hat{\phi} = \int \frac{d^3\mathbf{q}}{(2\pi)^{3/2}\sqrt{2\omega_q}} (\hat{a}_\mathbf{q} e^{iq \cdot x} + \text{h.c.}), \quad (5.21)$$

$$\hat{\chi} = \int \frac{d^3\mathbf{p}}{(2\pi)^{3/2}\sqrt{2\omega_p}} (\hat{a}_\mathbf{p} e^{ip \cdot x} + \text{h.c.}), \quad (5.22)$$

where  $\hat{a}_q$  and  $\hat{a}_p$  are the annihilation operators of  $\phi$  and  $\chi$ , respectively, whose hermitian conjugate  $\hat{a}_q^\dagger$  and  $\hat{a}_p^\dagger$  are the corresponding creation operators. Moreover,  $\omega_q^2 = |\mathbf{q}|^2 + m_\phi^2$  and  $\omega_p^2 = |\mathbf{p}|^2 + m_\chi^2$  with  $m_\chi$  the mass of  $\chi$  which is much lighter than  $\phi$ . With Eqs. (5.21) and (5.22), Equation (5.20) becomes

$$\mathcal{A} = \frac{-ig^2}{2}(2\pi)^4 \delta^{(4)}(p_1 + p_2 - q_1 - q_2) \times \frac{1}{\sqrt{2\omega_{p_1}}} \frac{1}{\sqrt{2\omega_{p_2}}} \frac{1}{\sqrt{2\omega_{q_1}}} \frac{1}{\sqrt{2\omega_{q_2}}}. \quad (5.23)$$

The transition rate, in the center-of-mass (CM) frame (i.e.  $\mathbf{p}_2 = -\mathbf{p}_1$  and  $\mathbf{q}_2 = -\mathbf{q}_1$ ), is therefore

$$\begin{aligned} \omega_{\chi\chi \rightarrow \phi\phi} &= \frac{1}{2!} \int \frac{d^3\mathbf{q}_1}{(2\pi)^3} \int \frac{d^3\mathbf{q}_2}{(2\pi)^3} (2\omega_{p_1})(2\omega_{p_2}) \frac{|\mathcal{A}|^2}{VT} \\ &= \frac{g^4}{128\pi^2} \int \frac{d^3\mathbf{q}_1}{\omega_{q_1}^2} \delta(\omega_{p_1} - \omega_{q_1}) \\ &= \frac{g^4}{32\pi} \int d\omega_{q_1} \sqrt{1 - \frac{m_\phi^2}{\omega_{q_1}^2}} \delta(\omega_{p_1} - \omega_{q_1}) \\ &= \frac{g^4}{32\pi} \sqrt{1 - \frac{m_\phi^2}{\omega_{p_1}^2}}. \end{aligned} \quad (5.24)$$

In the quantum field theory, as usual,  $VT$  is interpreted as  $(2\pi)^4 \delta^{(4)}(p_1 + p_2 - q_1 - q_2)$ . Here we used the relations  $d^3\mathbf{q}_1 = 4\pi|\mathbf{q}_1|^2|d|\mathbf{q}_1|$  and  $|\mathbf{q}_1|d|\mathbf{q}_1| = \omega_{q_1} d\omega_{q_1}$  to derive Equation (5.24). It is clear that the  $\chi\chi \rightarrow \phi\phi$  scattering occurs only when  $\omega_{p_1} > m_\phi$ .

The transition rate here describes the number of scattering events happening in a unit time at a certain CM energy of the incoming  $\chi$ -particles. We can simply obtain the increasing number of outgoing  $\phi$ -particles as

$$dN_{\phi,\omega_{p_1}} = 2\omega_{\chi\chi \rightarrow \phi\phi} N_{\phi,\omega_{p_1}} dt. \quad (5.25)$$

At the energy scale much larger than  $m_\phi$ , the transition rate returns to  $g^4/32\pi$ . We assume that the  $\phi$  will never decay into  $\chi$  during the production so that the number of  $\phi$  increases exponentially until  $M_\bullet$  reaches zero.



### 5.3.3 Black hole perturbations

We can observe the cosmic background of perturbations existing before the parent black hole forms rather than the perturbations from individual events travelling through the event horizon. The reason is that it takes an infinitely long time for the perturbations to depart from the event horizon to the black hole interior.

On the other hand, Firouzjshi's has investigated the observability of the perturbations in a Schwarzschild-de Sitter model from the baby universe [105]. He proposed that the primordial perturbations of the baby universe are associated with the quantum fluctuations of a massless scalar field near the event horizon in the black hole side. However, we have claimed in Chapter 4 that the pre-existing perturbations must dominate the so-called “black hole perturbation” generated by quantum fluctuations.

The perturbations in a Schwarzschild black hole have already been studied for a long time [138–140]. Regge and Wheeler firstly proposed the evolution equation, known as the Regge-Wheeler equation, of perturbations with odd parity (also known as the “axial” perturbations) [138]:

$$\frac{d^2 Z_{\omega,s,\ell}}{dr_*^2} + (\omega^2 - V_{RW}) Z_{\omega,s,\ell} = 0, \quad (5.26)$$

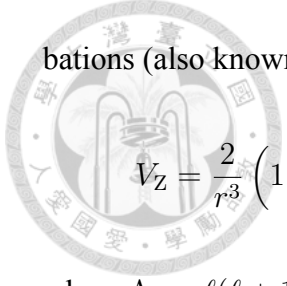
where  $Z_{\omega,s,\ell}$  collectively denotes the mode function of all kinds of perturbations and  $r_*$  is the tortoise coordinate which is defined by

$$r_* = r + \log \left( 1 - \frac{r}{2M_\bullet} \right) \quad (5.27)$$

for the black hole interior ( $r < 2M_\bullet$ ). The effective potential  $V_{RW}$  is given by

$$V_{RW} = \left( 1 - \frac{2M_\bullet}{r} \right) \left[ \frac{\ell(\ell+1)}{r^2} + \frac{2M_\bullet}{r^3} (1 - s^2) \right], \quad (5.28)$$

where  $s$  denotes the spin of  $Z_{\omega,s,\ell}$  with 0 for scalar perturbations, 1 for vector perturbations, and 2 for GWs. Zerilli later found that Equation (5.26) describes the even-parity pertur-



bations (also known as the “polar” perturbations) as well by replacing  $V_{\text{RW}}$  with [139]

$$V_Z = \frac{2}{r^3} \left(1 - \frac{2M_\bullet}{r}\right) \frac{\Lambda_\ell^2(\Lambda_\ell + 1)r^3 + 3\Lambda_\ell^2 M_\bullet r^2 + 9\Lambda_\ell M_\bullet^2 r + 2M_\bullet^3}{(\Lambda_\ell r + 2M_\bullet)^2}, \quad (5.29)$$

where  $\Lambda_\ell = \ell(\ell + 1)/2 - 1$ . We note that for any kind of perturbations one needs  $\ell \geq s$ .

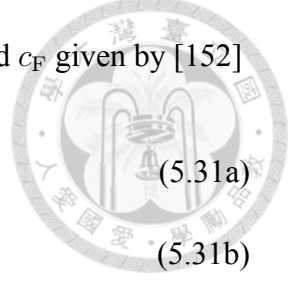
The axial and polar modes are closely related to each other. It is possible to transform one to another via suitable differential operations [141] (see Ref. [142] as well for details). We thus only need to consider one of them, in particular  $V_{\text{RW}}$ , with only a simple parameter  $s$  distinguishing different types of perturbations.

There is no normal mode due to the fact that there are no outgoing perturbation on the event horizon and ingoing perturbation at the center of the black hole. Therefore the perturbations survive in a black hole as damping oscillations called “quasi normal modes” (QNMs) [143, 144] (see also Refs. [145, 146]). The QNMs are the solutions of Equation (5.26) with  $V_{\text{RW}}$  and  $V_Z$ .

Despite of the difficulty on solving Equation (5.26), it is still possible to figure out the behaviors of QNMs by analysing their boundary conditions [147]. Some studies found that the QNMs can be the hints of quantum gravity [148, 149], in particular, the Hawking radiation. Hod further discovers that the quasi normal frequencies of Schwarzschild black holes tend to the Hawking temperature by a factor of  $\log 3$  [149]. This result is almost consistent with the interpretation of statistical mechanics of black hole entropy. Moreover, the damping time of QNMs depends linearly on the mass of the black hole [141], meaning that the perturbations damp faster when the mass of the black hole decreases owing to the inflaton production.

Fiziev have finally solved the exact solutions of Equation (5.26) with  $V_{\text{RW}}$  as the confluent Heun functions [150, 151] for both interior and exterior of a black hole. Firouzjahi further found an asymptotic form for  $r_* \rightarrow 0$  (the center of the black hole) as [152]

$$Z_{\omega,s,\ell} \rightarrow r_*^{(1+s)/2} {}_2F_1 \left( a_F, b_F, c_F, 1 + \frac{r_*}{2M_\bullet} \right), \quad (5.30)$$



where  ${}_2F_1$  is the hypergeometric function. The parameters  $a_F$ ,  $b_F$ , and  $c_F$  given by [152]

$$a_F = \frac{1+s^2}{2} + 2i \left( \pm\omega + \sqrt{\omega^2 + \beta_F^2} \right), \quad (5.31a)$$

$$b_F = \frac{1+s^2}{2} + 2i \left( \pm\omega - \sqrt{\omega^2 + \beta_F^2} \right), \quad (5.31b)$$

$$c_F = 1 \pm 4i\omega, \quad (5.31c)$$

with

$$\beta_F^2 = \frac{1}{4e} \left[ (1-s^2) \left( \frac{e}{4} - 1 \right) - \ell(\ell+1) \right]. \quad (5.32)$$

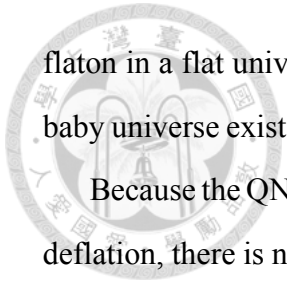
A regular  $Z_{\omega,s,\ell}$  at  $r_* \rightarrow 0$  requires that either  $a_F$  or  $b_F$  to be a non-positive integer. Firouzjahi therefore obtained, for either case, the spectrum of the perturbations for the bound state which has the form  $Z_{\omega,s,\ell} \propto e^{i\omega r_*}$  with a purely imaginary  $\omega$  [152]. This indicates, again, the damping nature of perturbations inside a black hole.

In summary, the cosmic background of the pre-existing GWs are the only perturbations standing inside the parent black hole and thus can survive the quantum bounce. The QNMs including the scalar perturbations must decay out in consequence there is no longer UV divergence.

## 5.4 Summary

In this chapter we mathematically studied the UV divergence problem of the scalar perturbation in the quantum bounce epoch. We found that under the approximations suggested by the literature the intrinsic curvature perturbations diverge exponentially before the bounce. To resolve the UV divergence, we suppose that our universe was born inside a Schwarzschild black hole so that the boundary conditions may attenuate perturbations.

First of all, we discuss the possibility for evolving a Schwarzschild black hole interior to a deflationary (de Sitter) geometry. We employed the Schwarzschild-FRW metric and found that it reduces to the de Sitter spacetime by converting the SM particles to the in-



flaton in a flat universe. This result indicates that a quantum bounce, and thus a separate baby universe exist naturally inside a Schwarzschild black hole under the context of LQC.

Because the QNMs including the scalar perturbations must eventually decay out before deflation, there is no longer UV divergence. It means that the only perturbation surviving inside the parent black hole is the pre-existing GW background. This is consistent with the current concordance model of cosmology as well as our previous studies.

We conclude that this possible scenario not only solves the UV divergence problem but also provides a new thought of solving the black hole information paradox [120, 153, 154] and even the dark energy problem [51] today according to the holographic principle [155, 156].



# Chapter 6

## Conclusion

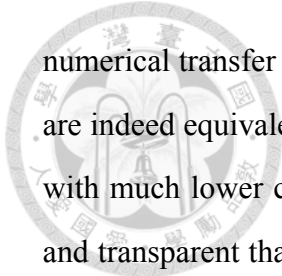
*“The starry heavens above me and the moral law within me.”*

— Immanuel Kant

### 6.1 Innovation and Achievement

This dissertation aims to probe the parent universe by figuring out the pre-existing GWs generated by stellar binaries and their imprints on the CMB B-mode polarization. In order to reach this target, we first studied the cosmic background dynamics, in particular the inflationary and deflationary epochs and the time asymmetry of the quantum bounce. We defined a new parameter  $\phi_B$  to quantitatively investigated the time asymmetry because the PKR used in the literature is not good enough to do so. With this  $\phi_B$ , we discussed deflation in a systematic manner and found the transition of the contractive behavior with respect to the time asymmetry. We minimized deflation by gaining  $\phi_B$  to the critical value  $\phi_{\text{crit}}$  and surprisingly revealed linear relationships between  $\phi_{\text{crit}}$  and the order of magnitude of the inflaton mass for both of the chaotic and  $R^2$  models.

The second thing we did is to evolve the pre-existing GWs from the parent universe through the quantum bounce to the end of inflation. For this purpose we proposed a new framework which employs the simple transfer functions instead of the complex Bogoliubov transformations that had used in the literature. We obtained both the analytical and



numerical transfer functions for the realistic epochs in our context, and verified that they are indeed equivalent to and produce the same results as the Bogoliubov transformations with much lower cost in calculation. This new framework is mathematically so simple and transparent that enable us to intuitively solved the IR suppression problem. The advantages of transfer functions should be beneficial to those studying the GWs in LQC.

Besides, we introduced the field-free approximation for the quantum effective mass of GWs and thus calculated the GW power spectrum more accurately.

The primary achievement of this study is that we successfully confined the LQC parameters using the current observational results. We found that, interestingly, the distinguishable features of the pre-existing GWs appear on large ( $l < 30$ ) and medium ( $30 < l < 200$ ) scale in the CMB angular power spectra. This allows not only space-based but also ground-based experiments to probe and test the parent universe in our model. We note that the cosmic background with time symmetry to the quantum bounce is ruled out. On the other hand, inflationary models that have been observationally ruled out are possible to revive within our framework.

We finally studied the pre-existing scalar perturbations which could lead to the UV divergence problem and even violate the fact of the existence of our present universe. To solve this problem we supposed a scenario which suggests that our present universe was born inside a parent black hole. This Schwarzschild-FRW black hole reduces to the deflationary epoch by unifying all the SM particles to the inflatons. The QNMs standing inside the black hole dominate the pre-existing scalar perturbations, nonetheless, we concluded that the boundary conditions on the event horizon indeed eliminate the UV divergence on the QNMs and thus recover the current understanding of our universe.

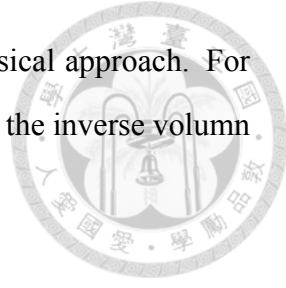
## 6.2 Outlook in the Future

In this section we list six significant topics for the future works on LQG and LQC.

- **Quantum corrections**

In this dissertation we counted only the zeroth-order holonomy correction, which is

the major contribution of the quantum effects in the semi-classical approach. For completeness, people should take higher-order holonomies and the inverse volume corrections into account in the future.



- **Inflationary models**

In particular, the inflationary models that we discussed in this dissertation are the chaotic potential (the simplest) and  $R^2$  potentials (observationally the most favored). It should be a good try to investigate other inflationary models under the context of LQC.

- **Sources of pre-existing GWs**

We studied only the GW background generated by the stellar binaries in the parent universe. It could be interesting if other astronomical systems such as rotating neutron stars and core-collapse supernovae are considered as sources of pre-existing GWs.

- **Parent black hole and baby universe**

The detailed mechanism of inflaton production in the parent black hole is still ambiguous. More so, the evolution of the QNMs in the deflationary epoch has not yet been seriously calculated in this dissertation. It remains a big issue to clearly figure out the UV divergence as well as the birth of our universe.

- **Information loss paradox**

It has been a long-time debate whether the informations falling into a black hole will come out again. One of the guesses is that the falling informations will be stored in the baby universe. The pre-existing GWs in our model could be a solution of this paradox.

- **Holographic principle and dark energy**

According to the holographic principle it is still possible for us to observe the exterior of the parent black hole (i.e. the parent universe) through the informations embedded on the event horizon. These informations could act on our universe as an unobservable interaction and thus become a candidate of the dark energy.





# Appendix A

## The Fourier Transform

We define the one dimensional Fourier transform of a function  $f(x)$  as

$$\tilde{f}(k) = F_x[f(x)] \equiv \int \frac{dx}{\sqrt{2\pi}} e^{-ikx} f(x),$$

so that the corresponding inverse transform is

$$f(x) = F_k^{-1}[\tilde{f}(k)] \equiv \int \frac{dk}{\sqrt{2\pi}} e^{ikx} \tilde{f}(k),$$

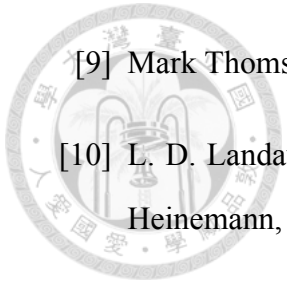
where  $x$  is the coordinate in real space and  $k$  is the wavenumber (frequency) in Fourier domain. The one dimensional Fourier transform can be easily generalized to a higher dimensional transform.



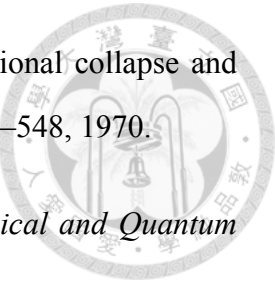


# Bibliography

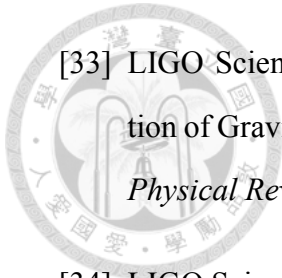
- [1] Wen-Hsuan Lucky Chang and Jiun-Huei Protty Wu. Time asymmetry of cosmic background evolution in loop quantum cosmology. *Physical Review D*, 99(12):123528, 2019.
- [2] Wen-Hsuan Lucky Chang and Jiun-Huei Protty Wu. New Approach to Evolving Gravitational Waves in Loop Quantum Cosmology. (summmited to *Physical Review D*). arXiv:1806.10508.
- [3] Wen-Hsuan Lucky Chang and Jiun-Huei Protty Wu. Signatures of the gravitational waves from parent universe in the CMB B-mode angular power spectrum. (summmited to *Physical Review Letters*).
- [4] Wen-Hsuan Lucky Chang and Jiun-Huei Protty Wu. A solution to the UV divergence of scalar perturbation in loop quantum cosmology. (in preparation).
- [5] Yu-Chiung Lin. *Gravitational Waves Predicted from Stellar Binaries and Rotating Neutron Stars*. Master thesis, National Taiwan University, 2016.
- [6] Norriss S. Hetherington. *Encyclopedia of Cosmology (Routledge Revivals) : Historical, Philosophical, and Scientific Foundations of Modern Cosmology*. Routledge, 2014.
- [7] Francis Halzen and Alan D. Martin. *Quarks and Leptons: An Introductory Course in Modern Particle Physics*. Wiley, 1984.
- [8] Matthew D. Schwartz. *Quantum Field Theory and the Standard Model*. Cambridge University Press, 2014.



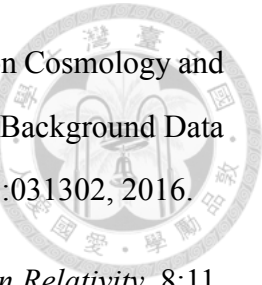
- [9] Mark Thomson. *Modern Particle Physics*. Cambridge University Press, 2013.
- [10] L. D. Landau and E. M. Lifshitz. *The Classical Theory of Fields*. Butterworth-Heinemann, 4th edition, 1980.
- [11] Sean Carroll. *Spacetime and Geometry: An Introduction to General Relativity*. Pearson, 2003.
- [12] Bernard Schutz. *A First Course in General Relativity*. Cambridge University Press, 2nd edition, 2009.
- [13] A. A. Penzias and R. W. Wilson. A Measurement of Excess Antenna Temperature at 4080 Mc/s. *The Astrophysical Journal*, 142:419, 1965.
- [14] C. Copi, D. Schramm, and M. Turner. Big-bang nucleosynthesis and the baryon density of the universe. *Science*, 267(5195):192–199, 1995.
- [15] P. J. E. Peebles. *Principles of Physical Cosmology*. Princeton University Press, 1993.
- [16] Edward Kolb and Michael Turner. *The Early Universe*. Westview Press, 1994.
- [17] Scott Dodelson. *Modern Cosmology*. Academic Press, 2003.
- [18] Ya.B. Zeldovich and M.Yu. Khlopov. On the concentration of relic magnetic monopoles in the universe. *Physics Letters B*, 79(3):239–241, 1978.
- [19] John P. Preskill. Cosmological Production of Superheavy Magnetic Monopoles. *Physical Review Letters*, 43(19):1365–1368, 1979.
- [20] Alan H. Guth. Inflationary universe: A possible solution to the horizon and flatness problems. *Physical Review D*, 23(2):347–356, 1981.
- [21] Andrew R. Liddle and David H. Lyth. *Cosmological Inflation and Large-Scale Structure*. Cambridge University Press, 2000.
- [22] Steven Weinberg. *Cosmology*. Oxford University Press, 2008.



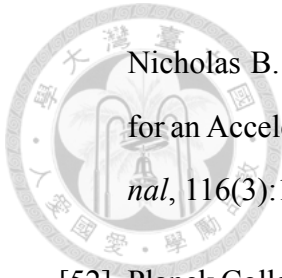
- [23] S. W. Hawking and R. Penrose. The singularities of gravitational collapse and cosmology. *Proceedings of the Royal Society A*, 314(1519):529–548, 1970.
- [24] Martin Bojowald. Isotropic loop quantum cosmology. *Classical and Quantum Gravity*, 19(10):2717, 2002.
- [25] Martin Bojowald. Absence of a Singularity in Loop Quantum Cosmology. *Physical Review Letters*, 86(23):5227–5230, 2001.
- [26] Abhay Ashtekar, Tomasz Pawłowski, and Parampreet Singh. Quantum nature of the big bang: Improved dynamics. *Physical Review D*, 74(8):084003, 2006.
- [27] Abhay Ashtekar, Tomasz Pawłowski, and Parampreet Singh. Quantum nature of the big bang: An analytical and numerical investigation. *Physical Review D*, 73(12):124038, 2006.
- [28] Abhay Ashtekar, Tomasz Pawłowski, and Parampreet Singh. Quantum Nature of the Big Bang. *Physical Review Letters*, 96(14):141301, 2006.
- [29] Martin Bojowald. Inflation from Quantum Geometry. *Physical Review Letters*, 89(26):261301, 2002.
- [30] Jakub Mielczarek, Thomas Cailleteau, Julien Grain, and Aurelien Barrau. Inflation in loop quantum cosmology: Dynamics and spectrum of gravitational waves. *Physical Review D*, 81(10):104049, 2010.
- [31] Julien Grain, Aurélien Barrau, Thomas Cailleteau, and Jakub Mielczarek. Observing the big bounce with tensor modes in the cosmic microwave background: Phenomenology and fundamental loop quantum cosmology parameters. *Physical Review D*, 82(12):123520, 2010.
- [32] LIGO Scientific Collaboration and Virgo Collaboration. Observation of Gravitational Waves from a Binary Black Hole Merger. *Physical Review Letters*, 116(6):061102, 2016.



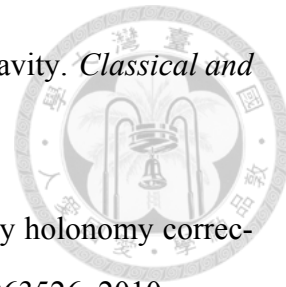
- [33] LIGO Scientific Collaboration and Virgo Collaboration. GW151226: Observation of Gravitational Waves from a 22-Solar-Mass Binary Black Hole Coalescence. *Physical Review Letters*, 116(24):241103, 2016.
- [34] LIGO Scientific Collaboration and Virgo Collaboration. GW170104: Observation of a 50-Solar-Mass Binary Black Hole Coalescence at Redshift 0.2. *Physical Review Letters*, 118(22):221101, 2017.
- [35] LIGO Scientific Collaboration and Virgo Collaboration. GW170814: A Three-Detector Observation of Gravitational Waves from a Binary Black Hole Coalescence. *Physical Review Letters*, 119(14):1–16, 2017.
- [36] LIGO Scientific Collaboration and Virgo Collaboration. GW170817: Observation of Gravitational Waves from a Binary Neutron Star Inspiral. *Physical Review Letters*, 119(16):30–33, 2017.
- [37] LIGO Scientific Collaboration and Virgo Collaboration, Fermi Gamma-ray Burst Monitor, and INTEGRAL. Gravitational Waves and Gamma-Rays from a Binary Neutron Star Merger: GW170817 and GRB 170817A. *The Astrophysical Journal*, 848(2):L13, 2017.
- [38] Antony M. Lewis. *Geometric algebra and covariant methods in physics and cosmology*. Doctoral thesis, University of Cambridge, 2001.
- [39] Planck Collaboration. Planck 2015 results. XI. CMB power spectra, likelihoods, and robustness of parameters. *Astronomy & Astrophysics*, 594:A11, 2016.
- [40] Planck Collaboration. Planck 2015 results. XIII. Cosmological parameters. *Astronomy & Astrophysics*, 594:A13, 2016.
- [41] Keck Array and BICEP2 Collaborations. BICEP2/KECK ARRAY V: MEASUREMENTS OF B-MODE POLARIZATION AT DEGREE ANGULAR SCALES AND 150 GHz BY THE KECK ARRAY. *The Astrophysical Journal*, 811(2):126, 2015.



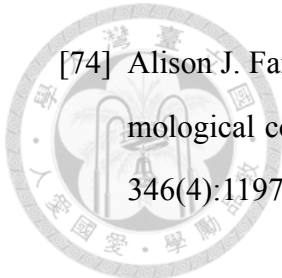
- [42] Keck Array and BICEP2 Collaborations. Improved Constraints on Cosmology and Foregrounds from BICEP2 and Keck Array Cosmic Microwave Background Data with Inclusion of 95 GHz Band. *Physical Review Letters*, 116(3):031302, 2016.
- [43] Martin Bojowald. Loop Quantum Cosmology. *Living Reviews in Relativity*, 8:11, 2005.
- [44] Kevin Vandersloot. Hamiltonian constraint of loop quantum cosmology. *Physical Review D*, 71(10):103506, 2005.
- [45] Martin Bojowald. The semiclassical limit of loop quantum cosmology. *Classical and Quantum Gravity*, 18(18):L109–L116, 2001.
- [46] Parampreet Singh and Kevin Vandersloot. Semiclassical states, effective dynamics, and classical emergence in loop quantum cosmology. *Physical Review D*, 72(8):084004, 2005.
- [47] Dah-Wei Chiou and Li-Fang Li. How loopy is the quantum bounce? A heuristic analysis of higher order holonomy corrections in loop quantum cosmology. *Physical Review D*, 79(6):063510, 2009.
- [48] Dah-Wei Chiou and Li-Fang Li. Loop quantum cosmology with higher order holonomy corrections. *Physical Review D*, 80(4):043512, 2009.
- [49] Martin Bojowald. Inverse scale factor in isotropic quantum geometry. *Physical Review D*, 64(8):084018, 2001.
- [50] Jérôme Martin, Christophe Ringeval, Roberto Trotta, and Vincent Vennin. The best inflationary models after Planck. *Journal of Cosmology and Astroparticle Physics*, 2014(3):039, 2014.
- [51] Adam G. Riess, Alexei V. Filippenko, Peter Challis, Alejandro Clocchiatti, Alan Diercks, Peter M. Garnavich, Ron L. Gilliland, Craig J. Hogan, Saurabh Jha, Robert P. Kirshner, B. Leibundgut, M. M. Phillips, David Reiss, Brian P. Schmidt, Robert A. Schommer, R. Chris Smith, J. Spyromilio, Christopher Stubbs,



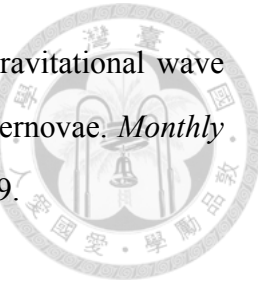
- Nicholas B. Suntzeff, and John Tonry. Observational Evidence from Supernovae for an Accelerating Universe and a Cosmological Constant. *The Astronomical Journal*, 116(3):1009–1038, 1998.
- [52] Planck Collaboration. Planck 2018 results. VI. Cosmological parameters. arXiv: 1807.06209.
- [53] Paul J. Steinhardt and Michael S. Turner. Prescription for successful new inflation. *Physical Review D*, 29(10):2162–2171, 1984.
- [54] D. S. Salopek and J. R. Bond. Nonlinear evolution of long-wavelength metric fluctuations in inflationary models. *Physical Review D*, 42(12):3936–3962, 1990.
- [55] Andrew R. Liddle and David H. Lyth. COBE, gravitational waves, inflation and extended inflation. *Physics Letters B*, 291(4):391–398, 1992.
- [56] Andrew R. Liddle, Paul Parsons, and John D. Barrow. Formalizing the slow-roll approximation in inflation. *Physical Review D*, 50(12):7222–7232, 1994.
- [57] Planck Collaboration. Planck 2013 results. XXII. Constraints on inflation. *Astronomy & Astrophysics*, 571:A22, 2014.
- [58] Planck Collaboration. Planck 2015 results. XX. Constraints on inflation. *Astronomy & Astrophysics*, 594:A20, 2016.
- [59] Planck Collaboration. Planck 2018 results. X. Constraints on inflation. arXiv: 1807.06211.
- [60] Abhay Ashtekar. New Variables for Classical and Quantum Gravity. *Physical Review Letters*, 57(18):2244–2247, 1986.
- [61] J. Fernando Barbero. Real Ashtekar variables for Lorentzian signature space-times. *Physical Review D*, 51(10):5507–5510, 1995.
- [62] Giorgio Immirzi. Real and complex connections for canonical gravity. *Classical and Quantum Gravity*, 14(10):L177–L181, 1997.



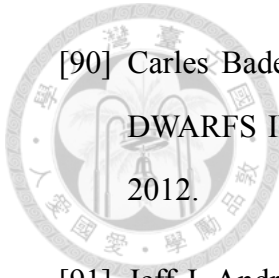
- [63] Krzysztof A Meissner. Black-hole entropy in loop quantum gravity. *Classical and Quantum Gravity*, 21(22):5245–5251, 2004.
- [64] Dah Wei Chiou and Kai Liu. Cosmological inflation driven by holonomy corrections of loop quantum cosmology. *Physical Review D*, 81(6):063526, 2010.
- [65] T Thiemann. Quantum spin dynamics (QSD). *Classical and Quantum Gravity*, 15(4):839–873, 1998.
- [66] Jiun-Huei Proty Wu. *Analytical and Numerical Approaches to Inflationary Cosmology*. Master thesis, The University of Sussex, 1996.
- [67] Jakub Mielczarek. Tensor power spectrum with holonomy corrections in loop quantum cosmology. *Physical Review D*, 79(12):123520, 2009.
- [68] Martin Bojowald and Golam Mortuza Hossain. Loop quantum gravity corrections to gravitational wave dispersion. *Physical Review D*, 77(2):27, 2007.
- [69] Frank Bowman. *Introduction to Bessel Functions*. Dover Publications, 1958.
- [70] Milton Abramowitz and Irene A. Stegun. *Handbook of Mathematical Functions: with Formulas, Graphs, and Mathematical Tables*. National Bureau of Standards, 10th edition, 1972.
- [71] Peter F. Michelson. On detecting stochastic background gravitational radiation with terrestrial detectors. *Monthly Notices of the Royal Astronomical Society*, 227(4):933–941, 1987.
- [72] Nelson Christensen. Measuring the stochastic gravitational-radiation background with laser-interferometric antennas. *Physical Review D*, 46(12):5250–5266, 1992.
- [73] Eanna E. Flanagan. Sensitivity of the Laser Interferometer Gravitational Wave Observatory to a stochastic background, and its dependence on the detector orientations. *Physical Review D*, 48(6):2389–2407, 1993.



- [74] Alison J. Farmer and E. S. Phinney. The gravitational wave background from cosmological compact binaries. *Monthly Notices of the Royal Astronomical Society*, 346(4):1197–1214, 2003.
- [75] T. Regimbau and J. A. de Freitas Pacheco. Stochastic Background from Coalescences of Neutron Star–Neutron Star Binaries. *The Astrophysical Journal*, 642(1):455–461, 2006.
- [76] T Regimbau and V Mandic. Astrophysical sources of a stochastic gravitational-wave background. *Classical and Quantum Gravity*, 25(18):184018, 2008.
- [77] T. Regimbau and Scott A. Hughes. Gravitational-wave confusion background from cosmological compact binaries: Implications for future terrestrial detectors. *Physical Review D*, 79(6):062002, 2009.
- [78] Alberto Sesana, Francesco Haardt, Piero Madau, and Marta Volonteri. The Gravitational Wave Signal from Massive Black Hole Binaries and Its Contribution to the LISA Data Stream. *The Astrophysical Journal*, 623(1):23–30, 2005.
- [79] A. Sesana, A. Vecchio, and C. N. Colacino. The stochastic gravitational-wave background from massive black hole binary systems: implications for observations with Pulsar Timing Arrays. *Monthly Notices of the Royal Astronomical Society*, 390(1):192–209, 2008.
- [80] Valeria Ferrari, Sabino Matarrese, and Raffaella Schneider. Stochastic background of gravitational waves generated by a cosmological population of young, rapidly rotating neutron stars. *Monthly Notices of the Royal Astronomical Society*, 303(2):258–264, 1999.
- [81] T. Regimbau and J. A. de Freitas Pacheco. Cosmic background of gravitational waves from rotating neutron stars. *Astronomy & Astrophysics*, 376(2):381–385, 2001.

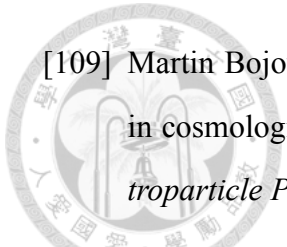


- [82] Valeria Ferrari, Sabino Matarrese, and Raffaella Schneider. Gravitational wave background from a cosmological population of core-collapse supernovae. *Monthly Notices of the Royal Astronomical Society*, 303(2):247–257, 1999.
- [83] David M. Coward, Ronald R. Burman, and David G. Blair. The stochastic background of gravitational waves from neutron star formation at cosmological distances. *Monthly Notices of the Royal Astronomical Society*, 324(4):1015–1022, 2001.
- [84] David M. Coward, Ronald R. Burman, and David G. Blair. Simulating a stochastic background of gravitational waves from neutron star formation at cosmological distances. *Monthly Notices of the Royal Astronomical Society*, 329(2):411–416, 2002.
- [85] T. Regimbau and J. A. de Freitas Pacheco. Gravitational wave background from magnetars. *Astronomy & Astrophysics*, 447(1):1–7, 2006.
- [86] Pablo A. Rosado. Gravitational wave background from binary systems. *Physical Review D*, 84(8):084004, 2011.
- [87] Michal Dominik, Emanuele Berti, Richard O’ Shaughnessy, Ilya Mandel, Krzysztof Belczynski, Christopher Fryer, Daniel E. Holz, Tomasz Bulik, and Francesco Pannarale. DOUBLE COMPACT OBJECTS. III. GRAVITATIONAL-WAVE DETECTION RATES. *The Astrophysical Journal*, 806(2):263, 2015.
- [88] Chunglee Kim, Benetge Bhakthi, Pranama Perera, and Maura A McLaughlin. Implications of PSR J0737–3039B for the Galactic NS–NS binary merger rate. *Monthly Notices of the Royal Astronomical Society*, 448(1):928–938, 2015.
- [89] Chunglee Kim, Vassiliki Kalogera, Duncan R. Lorimer, and Tiffany White. The Probability Distribution Of Binary Pulsar Coalescence Rates. II. Neutron Star-White Dwarf Binaries. *The Astrophysical Journal*, 616(2):1109–1117, 2004.

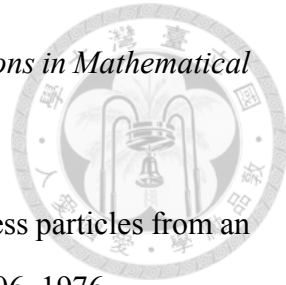


- [90] Carles Badenes and Dan Maoz. THE MERGER RATE OF BINARY WHITE DWARFS IN THE GALACTIC DISK. *The Astrophysical Journal*, 749(1):L11, 2012.
- [91] Jeff J. Andrews, Adrian M. Price-Whelan, and Marcel A. Agüeros. THE MASS DISTRIBUTION OF COMPANIONS TO LOW-MASS WHITE DWARFS. *The Astrophysical Journal*, 797(2):L32, 2014.
- [92] Bülent Kiziltan, Athanasios Kottas, Maria De Yoreo, and Stephen E. Thorsett. THE NEUTRON STAR MASS DISTRIBUTION. *The Astrophysical Journal*, 778(1):66, 2013.
- [93] J. Casares and P. G. Jonker. Mass Measurements of Stellar and Intermediate-Mass Black Holes. *Space Science Reviews*, 183(1-4):223–252, 2013.
- [94] Janusz Ziokowski. Masses of Black Holes in the Universe. *Chinese Journal of Astronomy & Astrophysics Supplement*, 8:273–280, 2008.
- [95] Jerome A. Orosz, James F. Steiner, Jeffrey E. McClintock, Michelle M. Buxton, Charles D. Bailyn, Danny Steeghs, Alec Guberman, and Manuel A. P. Torres. THE MASS OF THE BLACK HOLE IN LMC X-3. *The Astrophysical Journal*, 794(2):154, 2014.
- [96] LIGO Scientific Collaboration. LIGO: the Laser Interferometer Gravitational-Wave Observatory. *Reports on Progress in Physics*, 72(7):076901, 2009.
- [97] LIGO Scientific Collaboration and Virgo Collaboration. Prospects for Observing and Localizing Gravitational-Wave Transients with Advanced LIGO and Advanced Virgo. *Living Reviews in Relativity*, 19, 2016.
- [98] LIGO Scientific Collaboration and Virgo Collaboration. Advanced LIGO. *Classical and Quantum Gravity*, 32(7):074001, 2015.
- [99] ESA/LISA Pathfinder Collaboration. eLISA: Astrophysics and cosmology in the millihertz regime. [arXiv:1201.3621](https://arxiv.org/abs/1201.3621).

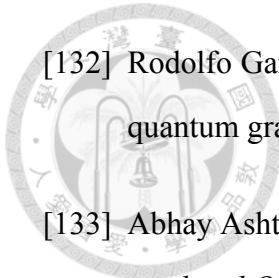
- [100] Xiao-Jun Yue and Jian-Yang Zhu. Power spectrum and anisotropy of super inflation in loop quantum cosmology. *Physical Review D*, 87(6):063518, 2013.
- [101] Susanne Schander, Aurélien Barrau, Boris Bolliet, Linda Linsefors, Jakub Mielczarek, and Julien Grain. Primordial scalar power spectrum from the Euclidean big bounce. *Physical Review D*, 93(2):023531, 2016.
- [102] Jian-Pin Wu and Yi Ling. The cosmological perturbation theory in loop cosmology with holonomy corrections. *Journal of Cosmology and Astroparticle Physics*, 2010(05):026–026, 2010.
- [103] Edward Wilson-Ewing. Holonomy corrections in the effective equations for scalar mode perturbations in loop quantum cosmology. *Classical and Quantum Gravity*, 29(8):085005, 2012.
- [104] Thomas Cailleteau, Jakub Mielczarek, Aurelien Barrau, and Julien Grain. Anomaly-free scalar perturbations with holonomy corrections in loop quantum cosmology. *Classical and Quantum Gravity*, 29(9):095010, 2012.
- [105] Hassan Firouzjahi. Primordial Universe Inside the Black Hole and Inflation. arXiv:1610.03767.
- [106] Hideo Kodama and Misao Sasaki. Cosmological Perturbation Theory. *Progress of Theoretical Physics Supplement*, 78:1–166, 1984.
- [107] Thomas Cailleteau and Aurelien Barrau. Gauge invariance in loop quantum cosmology: Hamilton-Jacobi and Mukhanov-Sasaki equations for scalar perturbations. *Physical Review D*, 85(12):123534, 2012.
- [108] Thomas Cailleteau, Aurélien Barrau, Francesca Vidotto, and Julien Grain. Consistency of holonomy-corrected scalar, vector, and tensor perturbations in loop quantum cosmology. *Physical Review D*, 86(8), 2012.



- [109] Martin Bojowald and Jakub Mielczarek. Some implications of signature-change in cosmological models of loop quantum gravity. *Journal of Cosmology and Astroparticle Physics*, 2015(08):052–052, 2015.
- [110] Boris Bolliet, Julien Grain, Clément Stahl, Linda Linsefors, and Aurélien Barrau. Comparison of primordial tensor power spectra from the deformed algebra and dressed metric approaches in loop quantum cosmology. *Physical Review D*, 91(8):084035, 2015.
- [111] Erich Kamke. *Differentialgleichungen Lösungsmethoden und Lösungen*. B. G. Teubner, Leipzig, 10th edition, 1977.
- [112] Valentin F. Zaitsev and Andrei D. Polyanin. *Handbook of Exact Solutions for Ordinary Differential Equations*. Chapman and Hall/CRC, Boca Raton, 2nd edition, 2002.
- [113] Robert W. Brehme. Inside the black hole. *American Journal of Physics*, 45(5):423, 1977.
- [114] V. P. Frolov, M. A. Markov, and V. F. Mukhanov. Through a black hole into a new universe? *Physics Letters B*, 216(3):272–276, 1989.
- [115] Curtis G. Callan, Steven B. Giddings, Jeffrey A. Harvey, Andrew Strominger, Steven B Giddings, Jeffrey A Harvey, and Andrew Strominger. Evanescent black holes. *Physical Review D*, 45(4):R1005–R1009, 1992.
- [116] V. Mukhanov and R. Brandenberger. A nonsingular universe. *Physical Review Letters*, 68(13):1969–1972, 1992.
- [117] Damien A Easson and Robert H Brandenberger. Universe generation from black hole interiors. *Journal of High Energy Physics*, 2001(06):024–024, 2001.
- [118] Martin Bojowald. Information loss, made worse by quantum gravity? *Frontiers in Physics*, 3:33, 2015.
- [119] S. W. Hawking. Black hole explosions? *Nature*, 248(5443):30–31, 1974.



- [120] S. W. Hawking. Particle creation by black holes. *Communications in Mathematical Physics*, 43(3):199–220, 1975.
- [121] Don N. Page. Particle emission rates from a black hole: Massless particles from an uncharged, nonrotating hole. *Physical Review D*, 13(2):198–206, 1976.
- [122] V.P. Frolov and G.A. Vilkovisky. Spherically symmetric collapse in quantum gravity. *Physics Letters B*, 106(4):307–313, 1981.
- [123] Thomas A. Roman and Peter G. Bergmann. Stellar collapse without singularities? *Physical Review D*, 28(6):1265–1277, 1983.
- [124] Sean A. Hayward. Formation and Evaporation of Nonsingular Black Holes. *Physical Review Letters*, 96(3):031103, 2006.
- [125] Valeri P. Frolov. Information loss problem and a ‘black hole’ model with a closed apparent horizon. *Journal of High Energy Physics*, 2014(5):49, 2014.
- [126] Leonardo Modesto. Disappearance of the black hole singularity in loop quantum gravity. *Physical Review D*, 70(12):124009, 2004.
- [127] Christian G. Böhmer and Kevin Vandersloot. Loop quantum dynamics of the Schwarzschild interior. *Physical Review D*, 76(10):104030, 2007.
- [128] Dah-Wei Chiou. Phenomenological loop quantum geometry of the Schwarzschild black hole. *Physical Review D*, 78(6):064040, 2008.
- [129] Leonardo Modesto. Black Hole Interior from Loop Quantum Gravity. *Advances in High Energy Physics*, 2008:1–12, 2008.
- [130] Rodolfo Gambini and Jorge Pullin. Black Holes in Loop Quantum Gravity: The Complete Space-Time. *Physical Review Letters*, 101(16):161301, 2008.
- [131] Rodolfo Gambini and Jorge Pullin. Loop Quantization of the Schwarzschild Black Hole. *Physical Review Letters*, 110(21):211301, 2013.



- [132] Rodolfo Gambini, Javier Olmedo, and Jorge Pullin. Quantum black holes in loop quantum gravity. *Classical and Quantum Gravity*, 31(9):095009, 2014.
- [133] Abhay Ashtekar and Martin Bojowald. Black hole evaporation: a paradigm. *Classical and Quantum Gravity*, 22(16):3349–3362, 2005.
- [134] G. C. McVittie. The Mass-Particle in an Expanding Universe. *Monthly Notices of the Royal Astronomical Society*, 93(5):325–339, 1933.
- [135] Jennie H. Traschen and Robert H. Brandenberger. Particle production during out-of-equilibrium phase transitions. *Physical Review D*, 42(8):2491–2504, 1990.
- [136] Lev Kofman, Andrei Linde, and Alexei A. Starobinsky. Reheating after Inflation. *Physical Review Letters*, 73(24):3195–3198, 1994.
- [137] Lev Kofman, Andrei Linde, and Alexei A. Starobinsky. Towards the theory of reheating after inflation. *Physical Review D*, 56(6):3258–3295, 1997.
- [138] Tullio Regge and John A. Wheeler. Stability of a Schwarzschild Singularity. *Physical Review*, 108:1063–1069, 1957.
- [139] Frank J. Zerilli. Effective Potential for Even-Parity Regge-Wheeler Gravitational Perturbation Equations. *Physical Review Letters*, 24(13):737–738, 1970.
- [140] C. V. Vishveshwara. Scattering of Gravitational Radiation by a Schwarzschild Black-Hole. *Nature*, 227(5261):936–938, 1970.
- [141] Luciano Rezzolla. Gravitational Waves from Perturbed Black Holes and Relativistic Stars. arXiv:gr-qc/0302025.
- [142] S. Chandrasekhar. *The Mathematical Theory of Black Holes*. Oxford University Press, Oxford, 1998.
- [143] C. V. Vishveshwara. Stability of the Schwarzschild Metric. *Physical Review D*, 1:2870, 1970.

[144] William H. Press. Long Wave Trains of Gravitational Waves from a Vibrating Black Hole. *The Astrophysical Journal*, 170:L105–L108, 1971.

[145] Kostas D. Kokkotas and Bernd G Schmidt. Quasi-Normal Modes of Stars and Black Holes. *Living Reviews in Relativity*, 2, 1999.

[146] Hans-Peter Nollert. Quasinormal modes: the characteristic ‘sound’ of black holes and neutron stars. *Classical and Quantum Gravity*, 16(12):R159–R216, 1999.

[147] Chris A Clarkson and Richard K Barrett. Covariant perturbations of Schwarzschild black holes. *Classical and Quantum Gravity*, 20(18):3855–3884, 2003.

[148] James W. York. Dynamical origin of black-hole radiance. *Physical Review D*, 28(12):2929–2945, 1983.

[149] Shahar Hod. Bohr’s Correspondence Principle and the Area Spectrum of Quantum Black Holes. *Physical Review Letters*, 81(20):4293–4296, 1998.

[150] Plamen P Fiziev. Exact solutions of Regge–Wheeler equation and quasi-normal modes of compact objects. *Classical and Quantum Gravity*, 23(7):2447–2468, 2006.

[151] Plamen P Fiziev. Exact solutions of Regge-Wheeler equation. *Journal of Physics: Conference Series*, 66(1):012016, 2007.

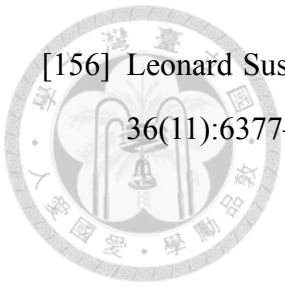
[152] Hassan Firouzjahi. The spectrum of perturbations inside the Schwarzschild black hole. [arXiv:1805.11289](https://arxiv.org/abs/1805.11289).

[153] John Preskill. Do Black Holes Destroy Information? [arXiv:hep-th/9209058](https://arxiv.org/abs/hep-th/9209058).

[154] S. Hossenfelder and L. Smolin. Conservative solutions to the black hole information problem. *Physical Review D*, 81(6):064009, 2010.

[155] C R Stephens, G ’t Hooft, and B F Whiting. Black hole evaporation without information loss. *Classical and Quantum Gravity*, 11(3):621–647, 1994.





- [156] Leonard Susskind. The world as a hologram. *Journal of Mathematical Physics*, 36(11):6377–6396, 1995.